HARVARD UNIVERSITY
Graduate School of Arts and Sciences

DISSERTATION ACCEPTANCE CERTIFICATE

The undersigned, appointed by the

Department of Physics

have examined a dissertation entitled

Dynamics in Biological Soft Materials

presented by Jennifer Hsin-I Hou

candidate for the degree of Doctor of Philosophy and hereby certify that it is worthy of acceptance.

Signature Adam E Cohen

Typed name: Professor Adam Cohen, Chair

Signature _____

Typed name: Professor Florian Engert

Signature _____

Typed name: Professor Aravinthan Samuel

Date: October 9, 2013

Dynamics in Biological Soft Materials

A dissertation presented

by

Jennifer Hsin-I Hou

to

The Department of Physics

in partial fulfillment of the requirements

for the degree of

Doctor of Philosophy

in the subject of

Physics

Harvard University

Cambridge, Massachusetts

October 2013

Dissertation Advisor: Adam E. Cohen Jennifer Hsin-I Hou

Dynamics in Biological Soft Materials

Abstract

I present applications of imaging and spectroscopy to understand mechanical, chemical, and electrical dynamics in biological materials. The first part describes the development and characterization of a protein-based fluorescent calcium and voltage indicator (CaViar). The far-red fluorescence of CaViar faithfully tracks the cardiac action potential in cardiomyocytes. CaViar's green fluorescence reports the resulting calcium transients. I demonstrated the applicability of CaViar *in vivo* with transgenic zebrafish designed to express CaViar in their hearts. Spinning disk confocal imaging allowed detailed three-dimensional mapping of simultaneous voltage and calcium dynamics throughout the heart of zebrafish embryos, *in vivo*, as a function of developmental stage. I tested the effect of channel blockers on voltage and calcium dynamics and discovered a chamber-specific transition from a calcium-dependent to a sodium-dependent action potential. I also describe a new measurement technique using a fluorescent voltage indicator to report absolute voltage via the indicator's temporal response.

Confocal spinning disk microscopy is a standard technique for imaging fluorescence in three-dimensional samples. Thus far, spinning disk microscopy has not been broadly used for imaging dim samples, due to low signal-to-noise ratios. I developed optical modifications to a commercial Yokogawa spinning disk microscopy system that drastically reduce autofluorescence emanating from the unit itself.

The last section of this thesis presents a new mode of motion in biological hydrogels via enzymatic degradation. I showed that a spatial gradient in the degradation of two gel/enzyme systems—gelatin/trypsin and hyaluronan/hyaluronidase—leads to directional motion of particles embedded in the gel in the direction of higher enzyme concentration. I studied the rate at which the degradation front propagates through the gel and the ensuing velocity of the embedded particles, as functions of enzyme and gel concentrations. I propose that asymmetric degradation leads to asymmetric swelling, which transports particles up the enzyme concentration gradient.

Contents

List of Figures

Acknowledgements

Graduate school has been a time of incredible academic and personal growth, and I have many people to thank for this experience. My advisor, Adam Cohen, is the most inspirational scientist I have ever met, and it was a true privilege to work with and learn from him. I was a great beneficiary of Adam's boundless energy and devotion towards furthering science and leading his research group in this pursuit. Joining a new lab was a unique and enlightening experience, and I am grateful to have been a part of the process. I am constantly humbled by Adam's unwavering mentorship at all odd hours of the day and night, his natural intuition for new project directions, and his fearlessness to take those ideas from just a figment of a dream to reality.

The work on cardiac imaging could not have been done without guidance from two postdocs, Joel Kralj and Adam Douglass. I am extraordinarily appreciative of their previous work on CaViar that enabled the *in vivo* work in zebrafish. Joel taught me all that is known about Arch, and was an exceedingly helpful mentor during my forays into CaViar and cardiology. Even in his last weeks at Harvard, Adam Douglass found the time to impart his wisdom on zebrafish cloning, husbandry, and imaging. I also thank the Engert Lab, for their help during my struggles in the fish facility and injection room. In particular, Abhi Grama, David Grant Hildebrand Colburn, and Clemens Riegler were exceptionally generous with their time and advice. I also acknowledge David Feldman, a rotation student in the Cohen Lab, who wrote the LabView program used for the 3-D spinning disk acquisition, and Emma Dowd, a talented undergraduate, who assisted tremendously with the zebrafish work over the last year.

I worked closely with another graduate student, Veena Venkatachalam, on the absolute voltage project of Chapter 3. I thank Veena for teaching me the art of patch-clamping, for maintaining a crazy tag-team schedule to continuously acquire data, and for keeping our spirits

high during the intense months to complete this project. The gel work of 0 greatly benefited from the scientific guidance of Katharina Ribbeck of MIT and Binny Cherayil of Indian Institute of Science.

It has been a pleasure to work with and learn from the amazingly talented team of scientists in the Cohen Lab. I am appreciative of their scientific input, technical assistance, and friendship, and am glad to have overlapped with: Alex Fields, Yiqiao Tang, Prashant Jain, Nan Yang, Halil Bayraktar, Min Ju Shon, Sabrina Leslie, Daniel Hochbaum, Hohjai Lee, Dougal Maclaurin, Lucy Rosenbaum, Jeehae Park, Tony Shen, Daan Brinks, Kit Werley, Dian Yang, Sami Farhi, Peng Zou, Vedha Nathan, and Niklas Smedemark-Margulies.

I thank my thesis committee, Professors Aravi Samuel and Florian Engert, for their guidance and comments as I prepared for my defense. I also thank my qualifying exam committee, Professors Vinny Manoharan and Zhigang Suo, for their insights and support during my first project on gels.

My graduate studies were funded by the National Defense Science & Engineering Graduate Fellowship and the National Science Foundation's Graduate Research Fellowship. The projects described in this thesis were supported from the Harvard Materials Research Science and Engineering Center under NSF grant DMR-0820484, the Presidential Early Career Award for Scientists and Engineers N00014-11-1-0549, and NIH grants R01EB012498-02 and DP2OD007428.

My years at Harvard were made extraordinary by the community here. For four years, Mather House was my home, where I lived as a resident tutor. I will miss the camaraderie of the incredible group of fellow tutors, students, and staff members. It was a blessing to have such a large and welcoming family in the Concrete Fortress.

I was so lucky to have my best friend from childhood, Celene Chang, be in Cambridge with me, as we experienced the highs and lows of graduate school together. Thank you for being an inspiration to look up to, a shoulder to lean on, and the best friend one could hope for. Amy Xu was a constant support, a fantastic workout buddy, and a source of puppy therapy when it was most needed. I also thank Heather Brink-Roby, Lily Huang, Marena Lin, Anna Wang, and Allison Zajac for their continuous care, laughter, and generosity over the past years.

Finally, I thank my parents and brother, for sacrificing so much for me from the very beginning, so that I could have the opportunities to pursue my dreams and fancies. I am indebted to their unconditional love and encouragement.

Introduction

The focus of my graduate work has been on the development and application of imaging and spectroscopic techniques to make novel measurements in biological samples. The couplings between mechanical, chemical, and electrical responses are complex, nuanced, and dynamic. With a combination of new genetic probes, spectroscopic measurements, optical engineering, and image analysis algorithms, I parsed apart some of these couplings to further our understanding in the fields of cardiac development, voltage imaging, and biological hydrogels.

Chapter 1 introduces a genetically-encoded simultaneous calcium and voltage indicator, CaViar. CaViar's ability to track membrane voltage and the resulting calcium dynamics is validated human-induced pluripotent stem cell-derived cardiomyocytes. Chapter 2 demonstrates an *in vivo* application of CaViar to zebrafish hearts. I constructed a complete spatiotemporal map of the cardiac action potential across an embryonic zebrafish heart *in vivo*. Via pharmacology, I discovered developmental stage- and chamber-specific functional changes in the ionic currents that drive the cardiac action potential in zebrafish.

In Chapter 3, I describe a measurement technique in which the time-domain response of a voltage sensitive Archaerhodopsin3 mutant reports absolute membrane voltage. I exploited the mutant's complex spectroscopic landscape to discover a time-dependent illumination scheme that led to a fluorescence transient whose relaxation depended on voltage. Parameterization of the relaxation yielded a one-to-one mapping with the numerical value of membrane voltage from human embryonic kidney cells. The techniques developed in the first part of this thesis enable future investigation in the electrical dynamics *in vivo*.

Chapter 4 describes modifications made to a commercial Yokogawa spinning disk confocal microscope system. I discovered a high autofluorescence from the internal optics of the unit. Modifications to the Yokogawa unit decreased background by 37-fold and enabled imaging of dim samples, such as Arch *in vivo* and single molecules.

The last part of this thesis, Chapter 5, discusses induced motion in biological hydrogels. I showed that spatially non-uniform enzymatic degradation of a gel leads to directional motion of particles embedded in the gel. I developed a quantitative model that describes the transport of the enzyme, the kinetics of the enzyme-gel reaction, and the resulting swelling of the gel. This work established a fundamentally new mechanism of motion of microscale objects in complex materials, with relevance to bacterial invasion through mucus, drug delivery, and growth of biofilms.

Below is a list of publications related to the work presented in this thesis:

[1] Hou JH and Cohen AE. (2012). Motion induced by asymmetric enzymatic degradation of hydrogels. *Soft Matter* **8**: 4616-4624.

[2] Kralj JM*, Hou, JH*, Douglass, AD, Wortzman, JR, Engert, F, Cohen AE. (2013). Simultaneous measurement of cardiac membrane voltage and calcium with a genetically encoded reporter. *In preparation*.

[3] Hou JH, Venkatachalam V, and Cohen AE. (2014). Temporal dynamics of microbial rhodopsin fluorescence reports absolute membrane voltage. *Biophysical Journal*. *In press*.

Chapter 1 Simultaneous measurement of cardiac membrane voltage and calcium with a genetically encoded reporter

1.1 Introduction

The cardiac action potential (AP) arises through the interaction of a large number of membrane proteins, and thus is an essential indicator of cardiac cell function. Excitation contraction coupling is mediated through voltage-dependent calcium flow into the cytoplasm, followed by calcium-triggered calcium release from the sarcoplasmic reticulum. Cytoplasmic Ca^{2+} induces a conformational change to the protein troponin upon binding. This change exposes myosin binding sites on the actin filaments. Thus, calcium allows binding of myosin to actin, and results in contraction of the cardiac muscle.

Advances in drug screening for safety [1–3] and efficacy [4, 5], new stem cell-based therapies [6], and improved understanding of cardiac development [7] all require new approaches to measure the relation of electrical and calcium dynamics, with increased throughput, wide dynamic range in space and time, and capability for long-term measurements *in vitro* and *in vivo* [8, 9].

Voltage-sensitive dyes (VSDs) have been used to record AP waveforms from intact hearts since the 1970's [7, 10, 11], in cultured cardiomyocytes since the early 1990's [12–14], and more recently from human iPSC-derived cardiomyocytes [15]. Simultaneous measurements with a VSD and a Ca^{2+} sensitive dye have been applied in intact guinea pig hearts [16] and in centimeter-scale cultures of human iPSC-derived cardiomyocytes [17, 18]. Due to dye-mediated phototoxicity, optical recordings with VSDs typically do not extend beyond one minute, and preparations are not

stable for repeated imaging. Dye-mediated phototoxicity is most acute for single-cell measurements, which require high magnification and consequently high illumination intensity.

In this chapter, we introduce a dual-function Ca^{2+} and voltage reporter (CaViar) for studies in cardiac electrophysiology. The cardiac AP is inherently dynamic—drugs or environmental changes affect cardiac function over timescales ranging from seconds to days. Thus the ability to perform long-term or repeated imaging with minimal phototoxicity was a key aim of our design. Cardiac electrophysiology is also multimodal—the dynamics of membrane voltage and Ca^{2+} are tightly coupled, so significant additional insight is gained by monitoring both simultaneously.

1.2 CaViar, a calcium and voltage indicator

Figure 1-1*a* shows the constructs characterized in this chapter: Arch(D95N)-eGFP and Arch(D95N)-GCaMP5G (CaViar). These dual-function indicators made use of the far-red spectrum of Arch(D95N) (ex. 594 – 640 nm, em. 710 nm) to avoid spectral crosstalk with the appended GFP-based expression marker (eGFP), Ca^{2+} indicator (GCaMP5G) [19].

In previous work performed at 25 ºC, the response of Arch(D95N) was dominated by a 41 ms time constant, with a minor component (< 20%) of the response occurring in < 1 ms [20]. Kinetic measurements at 35 ºC showed the sub-millisecond component of the response grew to 47% on a rising step and 59% on a falling step (Figure 1-1*b*). The slow component of the response is expected to somewhat distort the peak of the AP waveform and to prohibit measurement of the rate of voltage upswing during phase 1 ($dV/dt|_{max}$). However, the speed is sufficient to distinguish atrial from ventricular waveforms, to detect shifts in AP width, and to detect arrhythmias.

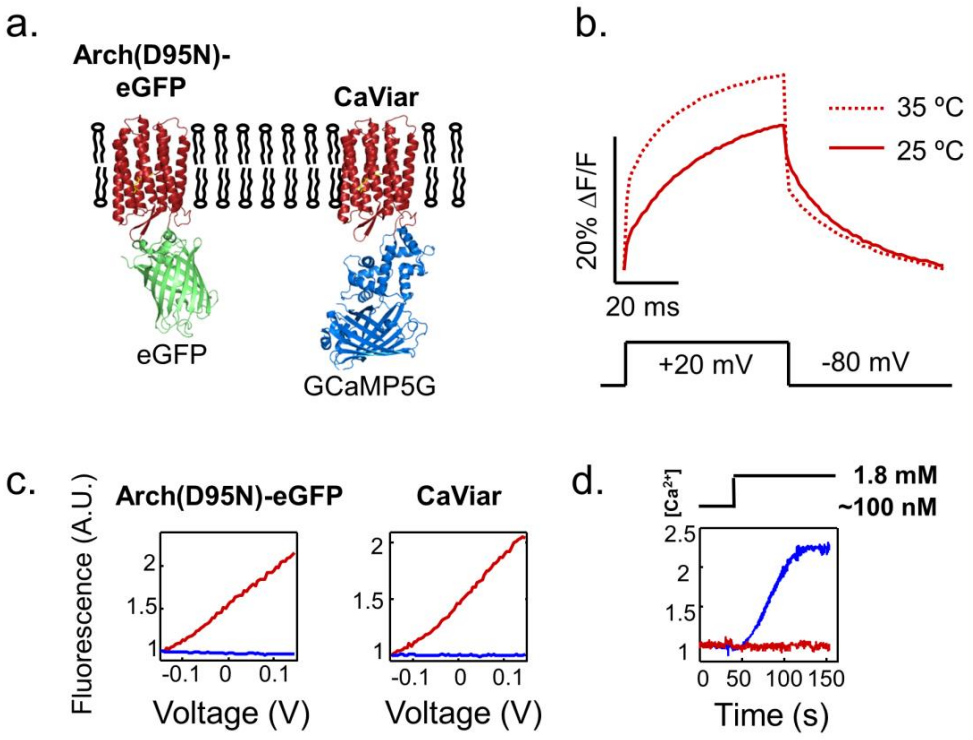

Figure 1-1: Multimodal indicators for voltage, Ca^{2+}
(*a*) Structures of fusions of the far-red voltage indicator Arch(D95N) with an expression marker (eGFP) or a calcium indicator (GCaMP5G). CaViar reports Ca^{2+} and voltage. (*b*) Step response of Arch(D95N) at 25 °C and 35 °C. At elevated temperature, the fast (< 1 ms) component of the response is enhanced to 47% of the response on the rising edge, 59% on the falling edge. (*c*) Steady-state fluorescence of Arch(D95N)-eGFP and CaViar as a function of membrane voltage. (*d*) Temporal response of CaViar to a change in $[Ca^{2+}]$. The red trace indicates fluorescence of Arch(D95N), and the blue trace indicates fluorescence of the appended GFP derivative (eGFP or GCaMP5G).

We monitored the fluorescence of Arch(D95N) and the appended GFP derivative in HEK cells as a function of steady state membrane voltage (Figure 1-1*c*). In both constructs, the fluorescence of Arch(D95N) increased roughly linearly with membrane voltage between -150 mV and +150 mV. In the eGFP fusion, eGFP fluorescence showed a very small voltage response with magnitude -3% of the response of Arch(D95N). We attribute this phenomenon to photochromic fluorescence resonance energy transfer (FRET), in which the excited eGFP underwent

nonradiative energy transfer to the retinal in Arch in a voltage-dependent manner [21]. CaViar did not show detectable crosstalk of voltage into the GCaMP5G channel.

We tested the response of the indicators to steps in $[Ca^{2+}]$ or pH (Figure 1-1*d*). Intact HEK cells expressing CaViar were permeabilized to Ca^{2+} with ionomycin, raising internal $[Ca^{2+}]$ to 1.8 mM. Fluorescence of GCaMP5G increased by 225%, while fluorescence of Arch(D95N) did not undergo a detectable change.

1.3 Expression in hiPSC cardiomyocytes

Commercially available terminally differentiated hiPSC-derived cardiomyocytes were plated at a density of 5×10^4 cells/cm^2. The cells formed a monolayer and contracted spontaneously within 2 days of plating. Beat rate was constant across the dish, indicating that the culture formed a single electrical syncytium. Expression was detectable after 2 days and was stable for at least 14 days. HiPSC-derived cardiomyocytes expressing Arch(D95N)-eGFP showed membrane labeling via Arch fluorescence as well as via eGFP fluorescence (Figure 1-2*a*). Both channels also showed peri-nuclear aggregates indicative of imperfect membrane trafficking. In spontaneously beating cells, Arch(D95N) emitted periodic flashes of fluorescence which were readily observed in the raw video. Fluorescence intensities were determined by a direct average over all pixels corresponding to a single cell. The eGFP photobleached faster than the Arch(D95N) so we did not normalize Arch(D95N) fluorescence by eGFP fluorescence.

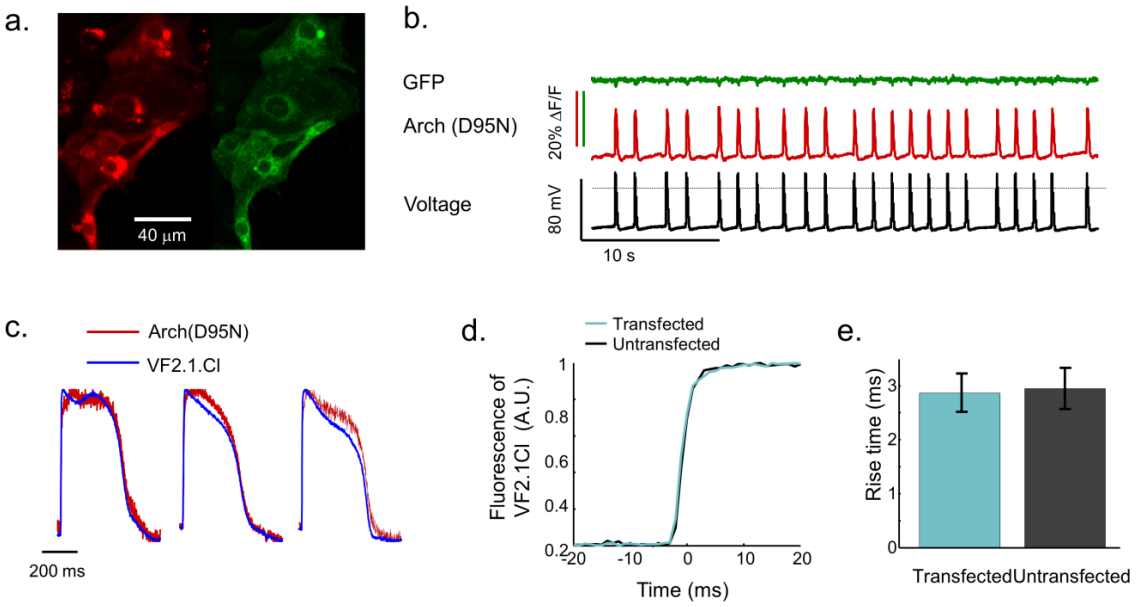

Figure 1-2: Arch(D95N) reports membrane voltage in hiPSC-derived cardiomyocytes
(*a*) Confocal image of cardiomyocytes expressing Arch(D95N) (*red*) and eGFP (*green*). (*b*) Simultaneous recording of eGFP fluorescence (*green*), Arch(D95N) fluorescence (*red*), and V_m via whole-cell patch clamp (*black*; dashed line indicates 0 V). (*c*) Comparison of AP waveforms reported by Arch(D95N) and a fast voltage-sensitive dye, VF2.1.Cl, recorded at 1 kHz. The genetically encoded reporter reproduced the AP upstroke and width, but distorted the peak of the AP. (*d*) Temporal AP upswing as measured by voltage-sensitive dye VF2.1.Cl in cells expressing Arch(D95N) (*teal*) vs. neighboring cardiomyocytes that did not express Arch(D95N) (*black*). (*e*) The rise time for transfected cells (20% to 80%) was 2.87 ± 0.94 ms, while for untransfected cells the rise time was 2.96 ± 1.01 ms, showing no statistically significant difference (n = 7 cells of each type).

We next compared the optically reported AP to manual patch-clamp measurements in cells expressing Arch(D95N)-eGFP (Figure 1-2*b*). The fluorescence of Arch(D95N) clearly indicated each AP. We determined the precision of the fluorescence-based voltage estimate using the maximum likelihood technique described previously [20]. During the diastolic interval, when V_m was slowly changing, the optical data resolved electrical dynamics with a precision of 510 $\mu V/(Hz)^{1/2}$.

To determine how accurately Arch(D95N) reported the details of the AP waveform, we simultaneously recorded fluorescence from Arch(D95N) and from a fast VSD, VF2.1.Cl. This VSD was recently shown to report AP waveforms with high accuracy and negligible capacitive loading [22]. Figure 1-2*c* shows overlays of fluorescence from Arch(D95N) and VF2.1.Cl, simultaneously acquired at a frame rate of 1 kHz. The protein and VSD reported similar rates of AP rise: the upstroke duration (20% to 80%) was 3.4 ± 0.8 ms as reported by Arch(D95N) and 3.3 ± 1.3 ms as reported by VF2.1.Cl (n = 6 cells). The slow component of the Arch(D95N) response led to a distortion of the peak of the AP but only a small increase in the reported width of the AP at 50% depolarization (AP_{50}; 348 ± 19 ms for Arch(D95N); 344 ± 21 ms for VF2.1.Cl; n = 6 cells).

A further concern was whether expression of Arch(D95N) affected the AP waveform. The gating charge of a transmembrane voltage indicator leads to capacitive loading of the cell membrane, which can be a serious perturbation to the electrophysiology [23]. The capacitive loading of Arch was recently shown to be negligible in HEK cells [24], but one might worry that expression of Arch(D95N) displaced endogenous ion channels or pumps. We used the VSD VF2.1.Cl to compare AP upstroke in cells expressing Arch(D95N)-eGFP, with neighboring cells in the same dish that had not taken up the gene. The upstroke velocity measured by the VSD was indistinguishable between cells with and without Arch(D95N) (Figure 1-2*d*-*e*) confirming that Arch(D95N) neither presented significant capacitive load nor displaced endogenous Na^+ channels.

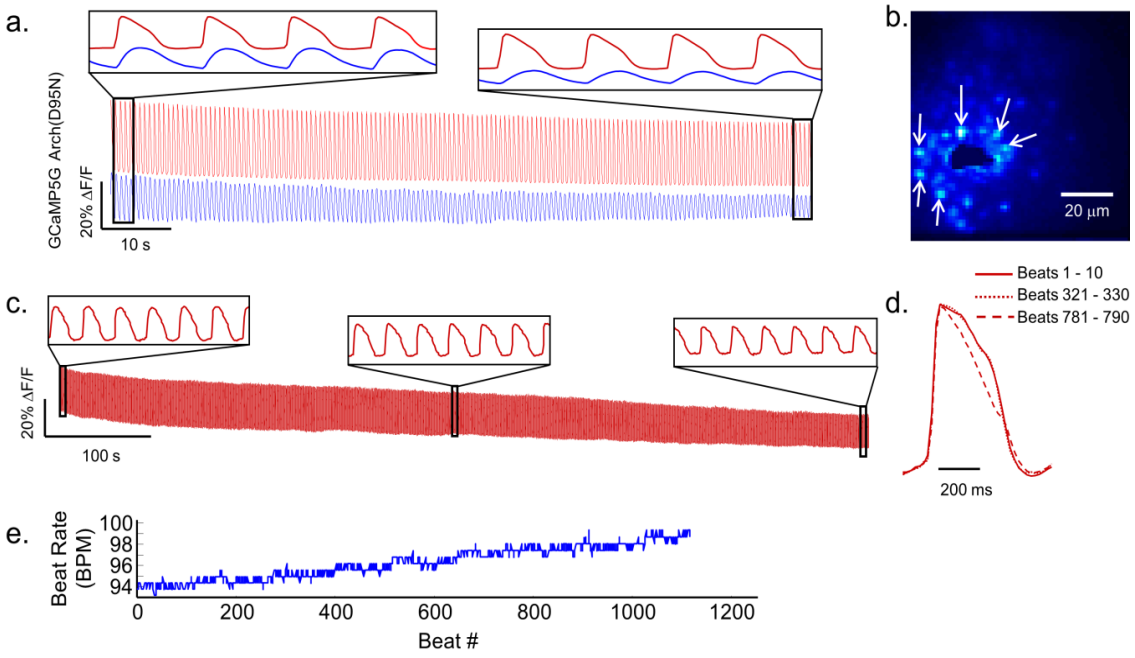

Figure 1-3: Dual indicator CaViar reports V_m and Ca^{2+} in hiPSC-derived cardiomyocytes
(*a*) Simultaneous recording of voltage and Ca^{2+} transients in a single cardiomyocyte expressing CaViar. (*b*) Image showing Ca^{2+} sparks, indicated by arrows, in a single cardiomyocyte. (*c*) Continuous 800 s optical recording from a single cardiomyocyte, showing spontaneous beating throughout the observation time. (*d*) Overlay of optically reported AP waveforms at the beginning and end of the recording in (*c*). (*e*) Beat rate during 800 s recording in (*c*).

Cells expressing CaViar showed flashes of green fluorescence (indicating cytoplasmic $[Ca^{2+}]$) and near infrared fluorescence (indicating V_m) accompanying each beat (Figure 1-3*d*). The transients in GCaMP5G fluorescence had a mean amplitude of $\Delta F/F$ = 16 ± 9% (n = 352 independent single-cell measurements). Calcium "sparks" were clearly visible in some cells (Figure 1-3*b*) [25]. Cells expressing CaViar continued to beat for several weeks, highlighting the low toxicity of genetically encoded reporters.

We sought to determine the phototoxicity limits on optical recordings with Arch(D95N). Figure 1-3*c* shows an 800-second continuous recording from a single hiPSC cardiomyocyte

expressing Arch(D95N)-eGFP. Over this interval, the total fluorescence photobleached by 18%. The AP waveform remained stable for the first 400 s and decreased in width by 25% over the next 400 s (Figure 1-3*d*), while the spontaneous beat rate increased by 4.8% over this interval from 94 to 98.5 beats/min (Figure 1-3*e*). These results demonstrate the feasibility of multiple-minute continuous recordings. Single cells were imaged for 40 s intervals on up to three consecutive days, with no indication of long-term phototoxicity.

1.4 Outlook

Genetically encoded voltage indicators enable optical imaging of cardiac action potentials *in vitro* with high throughput, high signal-to-noise ratio, over long times, and with low levels of photoxicity. In contrast to conventional patch-clamp methods, sterility of the dish is maintained and cells can be probed on multiple successive days. Long-term imaging allows observation of gradual changes in electrophysiology associated with maturation, as well as changes associated with natural or drug-induced variations in gene expression. CaViar reports voltage and Ca^{2+} simultaneously, permitting correlation of these two modalities on a cell-by-cell basis.

The ability to perform optical recordings from many single cells, and then to return to the same cells after administration of a drug, opens the possibility to segment drug responses by cardiomyocyte cell type (e.g. looking for differential effects in atrial and ventricular cells). Drug studies which only probe the population-average response may miss significant variation in the response among cellular subtypes. This challenge is particularly significant for experiments with human iPS-derived cardiomyocytes, where at present pure populations of atrial or ventricular cells cannot be produced. Optical screening of AP waveforms provides a means to monitor the

differentiation process in efforts to generate pure populations of particular cardiomyocyte subtypes.

1.5 Methods

1.5.1 Cloning

For expression in hiPSC cardiomyocytes, Arch(D95N)-eGFP was cloned from the lenti-viral backbone pJMK004 (Addgene 34616), and ligated into the CMV expression backbone pLenti-CMV-Puro (Addgene 17448) cut with *Bam*HI and *Sal*I restriction enzymes.

Arch(D95N)-GCaMP5G was constructed by isothermal cloning [26]. The pLenti-CMV-Puro backbone was cut with *Bam*HI and *Sal*I restriction enzymes. Arch(D95N) (Addgene 34616) and GCaMP5G (Addgene 31788) were amplified and isothermally ligated to the backbone for one hour at 50 °C.

1.5.2 iPSC cardiomyocyte cell culture and transfection

Human induced pluripotent stem cell (iPSC) derived cardiomyocytes (iCell® Cardiomyocytes) were purchased from Cellular Dynamics Inc. (CDI, Madison Wisconsin). Cells were plated in 35 mm diameter MatTek dishes following manufacturer's instructions. The coverslip was coated in 0.02% gelatin and 5 μg/mL fibronectin for 1 hour before plating. Cells were thawed according to manufacturer's directions and plated at densities of 20, 50, or 75×10^3 cells/cm^2 in 500 μL of plating medium (CDI). Cells were incubated at 37 ˚C in 6% CO_2. After 48 hours, cells were switched to maintenance medium (CDI) and fed every 48 hours for up to 1 month. At a plating density of 2×10^4 cells/cm^2, cells did not beat spontaneously. At densities of 5 and

7.5×10^4 cells/cm^2, cells formed a confluent monolayer that began irregular beating after 48 – 96 hours, and regular beating after ~10 days.

iPSC cardiomyocytes were transfected 4 – 20 days after plating, using TransIT-LT1 transfection reagent (Mirus) according to the manufacturer directions. A mixture of 40 μL Opti-MEM (Invitrogen), 200 ng plasmid DNA and 1.2 μL TransIT-LT1 transfection reagent was incubated at room temperature for 20 minutes. Fresh maintenance medium was added to the iPSC cells during the incubation and the transfection mixture was added dropwise over the plate and left for 48 hours. Transfection efficiencies were 3 - 5%. Cells were imaged 2 - 12 days after transfection.

To generate lenti-virus with Arch(D95N)-GCaMP5G, HEK cells were transfected with a second generation lenti-viral packaging construct PSPax2, and the envelope protein VSVg. Transfection was carried out by combining 250 μL optimem, 2 μg plasmid DNA, 4 μg PSPax2 DNA, and 3 μg VSVG DNA. This mixture was combined with 36 mL polyethyleneimine (PEI) at a concentration of 1 mg/mL and left to sit for 10 minutes. The DNA/PEI solution was added dropwise over a 10 cm plate of HEK cells with a medium change after 6 hours. Virus was harvested 48 hours later by spinning down cell medium at 500 g for 5 min to collect cellular debris. The supernatant was filtered through a 0.45 μm filter.

The virus was concentrated by ultra-centrifugation in a 20% sucrose solution. The filtered medium was added to 2 mL of 20% sucrose in an ultracentrifuge tube and spun for 2 hours at 22,500 RPM in a Beckman Coulter Optima centrifuge. The supernatant was discarded and the pellets were resuspended in PBS. This solution was added directly to the cells.

1.5.3 Microscopy of hiPSC-derived cardiomyocytes

Cardiomyocytes were imaged in a homebuilt inverted microscope, similar to that described in the Online Supplement to Ref. [20]. Prior to imaging, cells were incubated with 5 μM all-*trans* retinal for 1 hour and washed with fresh maintenance medium (500 μL). Imaging was performed in fresh maintenance medium without all-*trans* retinal. Cells were maintained at 32 - 34 $^{\circ}$C using a heated stage (Warner QE-1), and an objective heater (Bioptechs 150819-13). In some experiments, imaging was performed in a carbogen (95% O_2, 5% CO_2) atmosphere.

Wide-field illumination was provided by solid state lasers at 640 nm (CrystaLaser DL-638-100-O, 100 mW) and at 488 nm (Omicron PhoxX, 60 mW) or 473 nm (Dragon laser, 50 mW). A dual-band dichroic mirror (Semrock FF483/639-Di01-25x36) reflected excitation to a 60x numerical aperture 1.45 oil immersion objective (Olympus 1-U2B616). Custom excitation and emission pathways allowed for continuously variable magnification between 10x and 66x. Imaging and illumination fields were typically 300 μm dia. Illumination was aligned to exit the objective at an angle just less than that required to enter total internal reflection, at an intensity of 0.25 W/cm^2 (488 nm) or 220 W/cm^2 (640 nm).

A home-made dual-view imaging system projected emission from eGFP or GCaMP5G (525 – 575 nm) and from Arch(D95N) (660 – 760 nm) onto adjacent halves of an EMCCD camera (Andor iXon$^+$ DU-860, 128 x 128 pixels). Exposure times were 1 – 20 ms. Custom scripts were written in LabView (National Instruments) to control the illumination, camera, and electrophysiological stimuli to the cell.

1.5.4 Electrophysiology

Filamented glass micropipettes (WPI) were pulled to a tip resistance of 3-10 MΩ, fire polished, and filled with internal solution (containing, in mM: 125 potassium gluconate, 8 NaCl, 0.6 $MgCl_2$, 0.1 $CaCl_2$, 1 EGTA, 10 HEPES, 4 Mg-ATP, 0.4 Na-GTP; pH 7.3; adjusted to 295 mOsm with sucrose). The micropipettes were positioned with a Burleigh PCS 5000 micromanipulator. Whole-cell voltage clamp recordings were acquired using an AxoPatch 200B amplifier (Molecular Devices), filtered at 2 kHz with the internal Bessel filter, and digitized with a National Instruments PCIE-6323 acquisition board at 10 kHz. Ambient 60 Hz noise was removed by digital filtering during post processing. All patch clamp data was recorded from spontaneously beating cells.

Chapter 2 CaViar in caviar: simultaneous calcium and voltage imaging in embryonic zebrafish hearts

2.1 Introduction

Chapter 1 demonstrated that expression of CaViar in cardiomyocytes enabled investigation of the cardiac AP over wider spatial and temporal scales than was previously achievable. Yet, certain aspects of cardiac electrophysiology cannot be probed by such *in vitro* studies. Fundamentally, the heart is a three-dimensional object; a hollow mass of muscle that contracts upon electrical and chemical signaling. The interplay between electrochemical inputs and mechanical responses cannot be replicated by two-dimensional cardiomyocyte cultures in a petri dish.

Early cardiac electrophysiology studies via electrodes were performed on the human heart during open heart surgery in the 1950s [27], and VSDs have been used to study AP waveforms from excised hearts since the 1970's [7, 10, 11]. More recently, simultaneous measurements with a VSD and a Ca^{2+} sensitive dye were performed in excised guinea pig hearts [16]. But thus far, no technique has allowed monitoring of both calcium and voltage transients in a live functional heart.

For measurements *in vivo*, genetically encoded reporters are preferred due to reduced toxicity and the ability to target specific cell-types. Here we apply our dual-function Ca^{2+} and voltage reporter CaViar to map simultaneous AP propagation and Ca^{2+} dynamics in the embryonic zebrafish heart. We identified a chamber-specific transition during development away from a Ca^{2+}-dominated AP upstroke. This transition occurred first in the ventricle, and later in the atrium. Distinct effects of drugs in the atrium and ventricle of the zebrafish heart highlight the importance

of measurements in well-defined cellular subtypes—a feature missing from studies on iPSC-derived cells.

2.2 Zebrafish as a model organism for cardiac development

Embryonic development is a complex, but coordinated dance: proliferation, migration, and differentiation are orchestrated by mechanical, chemical, and electrical cues to transform a single-celled zygote into a multicellular functional organism. In vertebrate embryogenesis, the heart is the first organ to develop [28], arising from the mesodermal layer. Critical to proper function, highly specialized cells within the cardiac tissue enable the heart to undergo concerted contractions, driving blood flow through the entire embryo.

We were interested in studying voltage and calcium dynamics in zebrafish as a system for investigating cardiac development. In Chapter 1, we observed the propagation of voltage and calcium transients in single cardiomyocytes, but how do these transients relate to neighboring cells? Over time in development, do the transients change? When does the heart become electrically active?

We sought to answer these questions using CaViar in the zebrafish heart. The zebrafish heart undergoes similar stages of development to that of the human heart: tube formation, looping, septation, and heart valve formation. These events first assemble the layer of non-contracting myocardial precursors into a peristaltic pump, then remodel the pump into a synchronously contracting multichambered pump with valves.

Zebrafish are an experimentally convenient organism for studying cardiac development. While morphogenesis to valve formation requires roughly 35 days in the human fetus or 12 days in the embryonic mouse, these events take only 48 hours in the zebrafish [28]. The zebrafish heart

is believed to start peristaltic contractions around 24 hpf [29] and the human heart starts beating at 21 days.

The zebrafish can survive without a circulatory system for the first few days of its life; it is small enough that its cells can rely on diffusion alone to receive sufficient oxygen [30]. Independence from a functional heart has led to the generation of many short-lived, but viable cardiac mutations that would otherwise be fatal in other species. These include but are not limited to mutations that affect morphological processes during organogenesis, vascular integrity, cardiac contractility, rhythm, and rate [31–33].

Finally, *in vivo* imaging of zebrafish is possible because embryos less than 24 hours post fertilization (hpf) are transparent. Pigmentation thereafter can be chemically inhibited with 1-phenyl-2-thiourea [34].

2.3 Previous work on voltage and Ca^{2+} measurements in zebrafish hearts

Microelectrodes have been used to study electrical activity in cultured adult zebrafish cardiomyocytes (Baker 1997), and hearts *ex vivo* [35] and *in vivo* [36], but are laborious and spatially limited to a few point measurements. Optical mapping of electrical excitation in explanted adult zebrafish hearts with the voltage sensitive dye di-4-ANEEPS indicated the presence of a ventricular conduction system, similar to that of humans [37] and the technique has subsequently been used to reveal electrical gradients patterned by *Wnt11* signaling in the developing heart [7].

Voltage imaging with a genetically encoded voltage indicator in zebrafish hearts was first performed in 2010 [38]. The authors found an interesting altered mode of excitation propagation stemming from the atrioventricular node upon astemizole treatment. However, the voltage sensor,

mermaid [39] used in this study, is a FRET-based measurement that requires simultaneous acquisition in two emission bands. Such a technique is subject to artifacts due to poor image alignment or differential photobleaching rates of the donor and acceptor. A FRET-based voltage measurement also occupies precious spectral real estate, which could otherwise be used to probe additional physiological parameters. Furthermore, the voltage sensitivity of mermaid is low; the maximal voltage change during a cardiac action potential only yielded a 5% change in fluorescence of the voltage sensor.

As voltage transients are tightly coupled to the resulting calcium fluxes, calcium imaging is often used as a substitute to elucidate the underlying voltage dynamics. To this end, the calcium dye, calcium green, has been used to observe cardiac conduction in larval zebrafish [40, 41] and a genetically based calcium indicator GCaMP2 was first demonstrated *in vivo* in 2008 [42]. However, spectral overlap of GCaMP2 with previously used voltage reporters has prevented simultaneous optical measurement of voltage and calcium. Furthermore, previously used voltage indicators lacked the temporal resolution to differentiate chamber-specific action potential waveforms. Simultaneous optical recording of V_m and $[Ca^{2+}]$ waveforms can provide insights into cardiac development not attainable from either modality alone.

2.4 Electrophysiological comparisons between human and zebrafish hearts

Action potentials from adult zebrafish have been compared directly to that of human cardiac tissue [35]. Zebrafish action potentials exhibited a rapid upstroke followed by a prolonged plateau phase that lasted longer in the ventricle than in the atrium. The zebrafish ventricular AP showed a similar waveform to that of the human ventricular cells, though it lacked the fast Phase 1 slight repolarization. With the use of selective ion channel blockers, the authors found

similarities to the human cardiac AP: the zebrafish AP upstroke was dominated by a Na^+ current, L-type Ca^{2+} channels contributed to the plateau phase, and inward rectifying K^+ channels are responsible for the repolarization. However, Nemtsas *et al*. found that both atrial and ventricular cardiomyocytes from the adult zebrafish appear to express T-type Ca^{2+} channels. This is in contrast to human cardiomyocytes, where T-type Ca^{2+} channels are expressed predominantly in embryonic hearts. T-type Ca^{2+} channels are nearly undetectable in the mature human ventricle, but are re-expressed in both cell types under pathological conditions [43].

The similarities of the major cardiac conductances, action potential shapes, and beat rates between zebrafish and humans indicate that zebrafish might be a useful model for cardiac studies. Ion channel analogs, such as the hERG analog *zerg*, have been found in zebrafish, and known QT-prolonging drugs induced similar responses such as bradycardia or arrhythmias in zebrafish embryos [44].

Differences, such as the presence of T-type Ca^{2+} channels and the ability to regenerate, raise interesting questions regarding whether the molecular and signaling mechanisms by which the zebrafish gains these abilities can be recapitulated in human hearts.

2.5 Simultaneous Ca^{2+} and voltage imaging in zebrafish hearts

We used CaViar to map simultaneous Ca^{2+} and voltage propagation in the embryonic zebrafish heart as a function of developmental stage. We generated a transgenic zebrafish line expressing CaViar under control of the *cmlc*2 promoter (Figure 2-1*a*). Fish developed normally and showed strong cardiac-localized fluorescence, beginning at 24 hours post fertilization (hpf). At 36 hpf, contractions were readily visualized in the developing heart tube and voltage and Ca^{2+} waveforms could be recorded from the atrium and ventricle using a modified spinning disk

confocal microscope. For fish younger than 48 hpf, supplemental retinal was added to increase fluorescence of Arch(D95N) (Section 2.8.3). Fish treated with supplemental retinal developed normally. After 48 hpf, endogenously produced retinal was sufficient to saturate the Arch(D95N) binding sites and no supplemental retinal was added.

We recorded dual-channel fluorescence movies of optical sections of the heart in a fish at 102 hpf. Flashes of fluorescence occurred in synchrony with the heartbeat, with red fluorescence indicating V_m and green fluorescence indicating $[Ca^{2+}]$. Action potentials in single cells in the ventricle were clearly resolved. For quantitative measurements, fish were soaked in blebbistatin (10 μM) prior to imaging to eliminate contraction and associated motion artifacts. It was then possible to map the propagation of voltage and Ca^{2+} waves across a single plane of the heart (Figure 2-1*b*). We generated a three-dimensional reconstruction of voltage propagation (Figure 2-1*c*) which clearly showed the AP originating in the atrium, spreading slowly across the atrioventricular (AV) canal, and rapidly spanning the ventricle.

Fish were imaged for up to several hours without apparent photodamage. After imaging sessions, fish were released from the agarose mount and allowed to recover in E3 medium. Voltage and calcium imaging the next day showed normal mechanical, electrical, and calcium heart function, indicating that treatments with blebbistatin and retinal were fully reversible, and that mounting and imaging had no apparent damage on fish health.

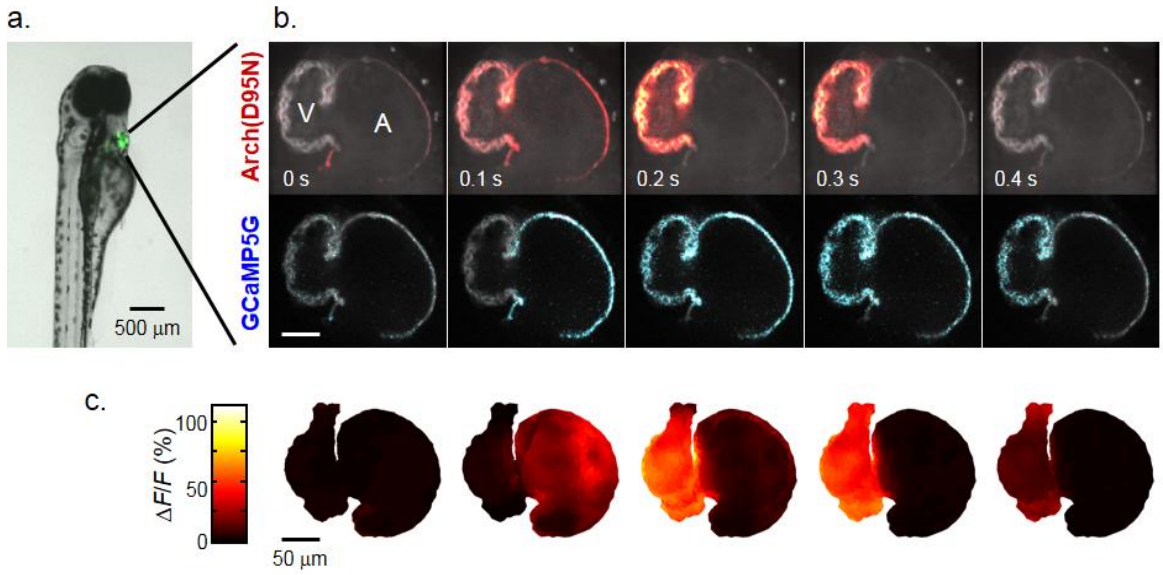

Figure 2-1: Mapping simultaneous V_m and Ca^{2+} in the zebrafish heart *in vivo*
(*a*) Fluorescence of eGFP in a fish expressing Arch(D95N)-eGFP under the *cmlc*2 promoter. (*b*) Single optical section of a zebrafish heart expressing CaViar at 4 dpf. Cell membranes lit up in both the voltage channel (*top*) and the Ca^{2+} channel (*bottom*) as the AP propagated from the atrium to the ventricle. (*c*) Three-dimensional reconstruction of the AP as reported by Arch(D95N).

2.6 Probing zebrafish cardiac maturation via pharmacology

We charted the spatial and temporal development of the voltage and Ca^{2+} patterns at 36, 54, and 102 hpf, using a new fish at each time-point (Figure 2-2; Figure 2-5). The heart showed distinct atrial and ventricular AP waveforms as early as 36 hpf, although the chambers were morphologically indistinct at this point [45]. The electrical APs recorded optically *in vivo* (Figure 2-5) were similar to previous reports of patch clamp measurements on explanted hearts [35, 42]. The Ca^{2+} dynamics also varied markedly along the heart tube, with a faster rise and slower decay in the atrium than in the ventricle (Figure 2-5), consistent with earlier reports [42]. By 54 hpf, the delay in electrical propagation at the AV canal was clearly visible, and by 102 hpf the APs in the atrium and ventricle occurred as two clearly resolved beats.

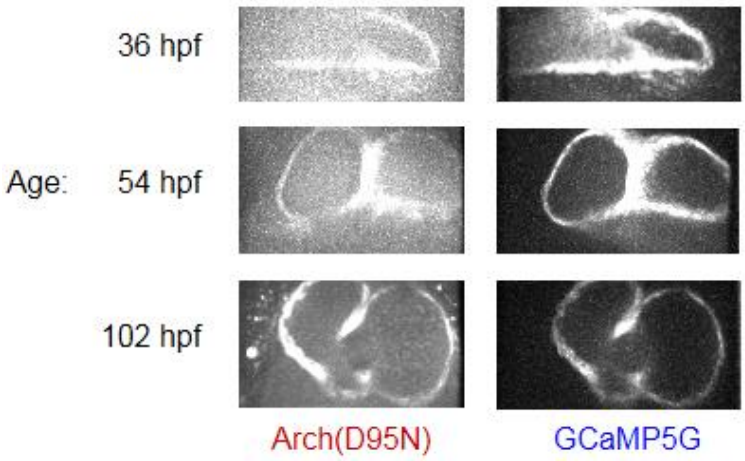

Figure 2-2: Embryonic zebrafish hearts at different stages in development
Fluorescence images of Arch(D95N) (*left)* and GCaMP5G (*right*) at 36 (*top*), 54 (*middle*), and 102 (*bottom*) hpf. These images were acquired from the ventral side of the sample. The atrium is on the right, and ventricle, left, of each image.

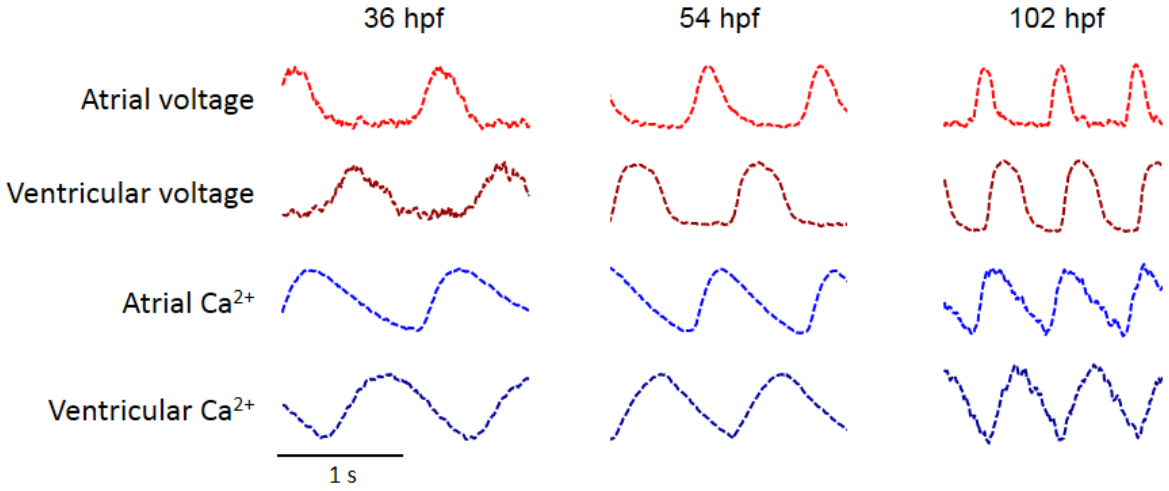

Figure 2-3: Voltage and calcium transients of the atrium and ventricle in an embryonic zebrafish heart during development
Voltage (*red*) and calcium (*blue*) transients as reported by CaViar in the two chambers of the zebrafish heart (atrium: *lighter shade*; ventricle: *darker shade*) at three times in development.

It was previously shown that in the adult zebrafish heart, the AP is dominated by a Na^+ current in both chambers and that nifedipine does not block the AP [35]. We wondered if this was true in embryonic zebrafish as well. Thus, we examined the effects of an L-type calcium channel

blocker, nifedipine (10 μM) and a sodium channel blocker, quinidine (10 μM) on voltage and Ca^{2+} dynamics. New fish were used at each time-point. Figure 2-4*a* contains representative traces showing the effect of the drug on the voltage and Ca^{2+} dynamics, in the atrium and the ventricle, at 90-102 hpf.

Remarkably, the ventricle and atrium showed strongly divergent responses to nifedipine. The ventricle continued to show electrical APs in the presence of nifedipine, despite the strong suppression of Ca^{2+} activity in both chambers. Electrical activity in the atrium was suppressed. In contrast, quinidine had the opposite effect on the electrical activity in the two chambers: only the atrium experienced APs; in the ventricle, APs were suppressed by the drug.

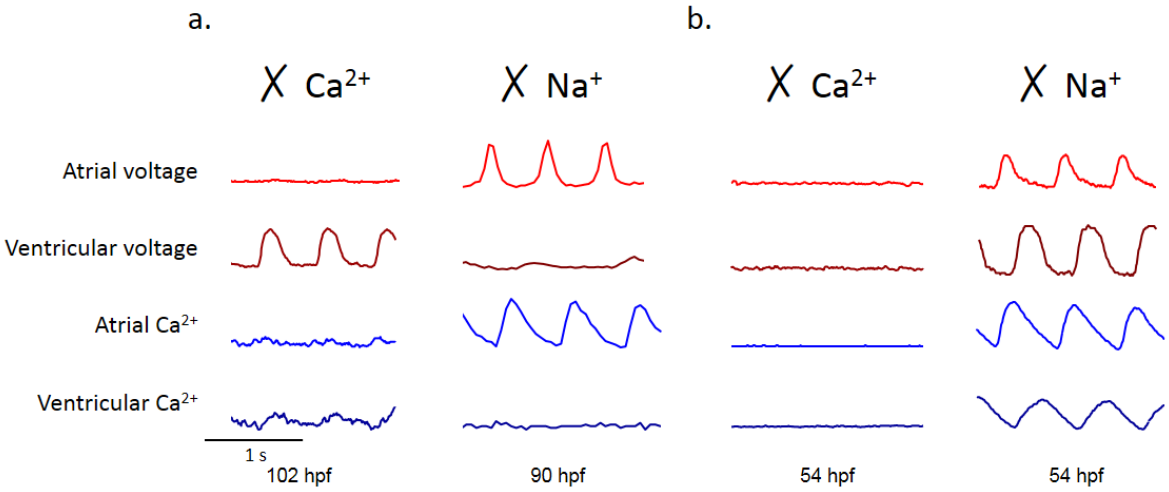

Figure 2-4: Effects of nifedipine and quinidine on atrial and ventricular chambers at different times in development
(*a*) At 90-102 hpf, L-type calcium channel blocker nifedipine suppressed all voltage and calcium transients, except for the ventricular voltage transient (*left*). Contrastingly, the sodium channel blocker quinidine suppressed atrial voltage and calcium transients, but did not affect either transient in the ventricle (*right*). (*b*) At 54 hpf, nifedipine caused complete blockage of both transients in both chambers (*left*), while quinidine did not have a measurable effect (*right*).

At slightly earlier times in development (54hpf), nifedipine largely suppressed the electrical APs in *both* chambers (Figure 2-4*b*). However, quinidine had no observable effect.

These observations indicate a Ca^{2+}-dependent pacemaker and the absence of Ca^{2+}-independent spontaneous electrical activity in either chamber.

Figure 2-5 shows summary statistics for nifedipine effects at three times in development. At all developmental stages, nifedipine largely suppressed Ca^{2+} transients in both chambers. At 36 hpf, effects of nifedipine were similar to that of at 54 hpf.

After nifedipine addition, the ventricular AP retained 75% of its initial amplitude (range 50% to 112%; n = 17 fish) similar to the results in hiPSC-derived cardiomyocytes. In contrast, nifedipine eliminated the atrial AP in 4 of 17 fish (< 20% of initial amplitude), and partially suppressed the atrial AP (35 – 80 % of initial amplitude) in the remainder fish. The differential effect of nifedipine on AP amplitude in the two chambers was pronounced ($p = 8.9 \times 10^{-5}$).

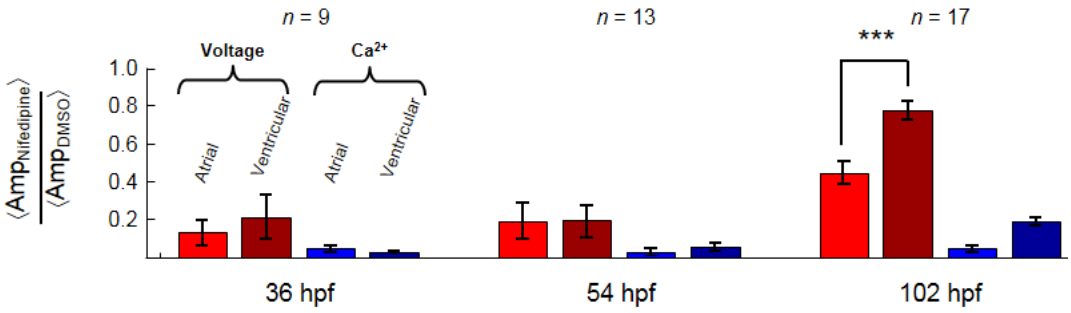

Figure 2-5: Differential effects of nifedipine on atrial and ventricular chambers during zebrafish development
Mean amplitude of the beats in the indicated modality (voltage or Ca^{2+}) in the presence of nifedipine, normalized by mean amplitude of the vehicle control. At 36 and 54 hpf, voltage and Ca^{2+} dynamics were suppressed by nifedipine in both atrium and ventricle. By 102 hpf, calcium activity was still largely suppressed by nifedipine, while voltage dynamics were only partially suppressed, more so in the atrium than in the ventricle.

Prior to drug addition, none of the ventricular waveforms showed a depolarizing "funny current" during diastole, consistent with a non-ventricular pacemaker. In fish where the atrial AP was suppressed entirely, the ventricular cells showed a significantly slowed beat rate (mean 104

bpm before drug vs. mean 70 bpm after drug) and a diastolic depolarization (Figure 2-6). Thus by 4 dpf, the zebrafish ventricle is capable of autonomous pacing, while at earlier times it is not.

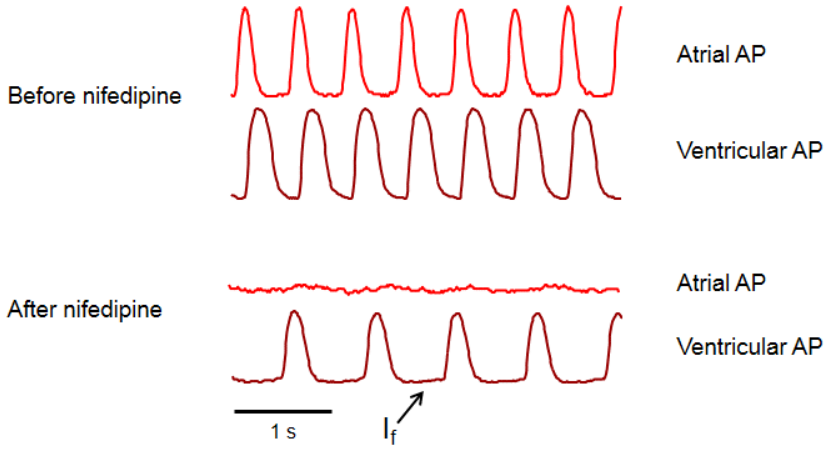

Figure 2-6: Appearance of a slow depolarizing funny current I_f after nifedipine treatment

Our results establish a transition from an immature Ca^{2+}-dependent AP to a mature Na^+-dependent AP that occurs first in the ventricle (around 3 dpf) and later in the atrium (around 4 dpf) (Figure 2-7).

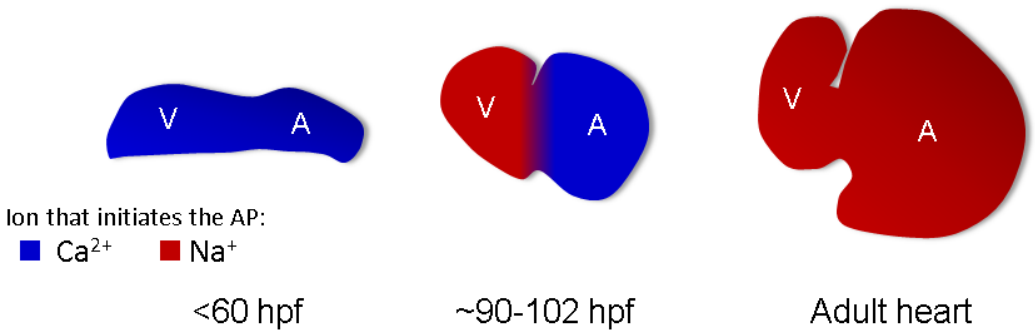

Figure 2-7: Maturation of cardiac AP is chamber-specific
At early times in development, Ca^{2+} initiates the action potential in both chambers. At an intermediate time in development (90-102 hpf), the atrial AP is driven by Ca^{2+} while the ventricular AP is driven by Na^+.

We note that this transition would not have been readily observed with Ca^{2+} or voltage imaging alone. Our results further highlight the importance of working with cardiomyocytes of well-defined subtype and developmental stage for cardiac drug testing—these parameters can have significant effects on drug responses.

2.7 Applications of CaViar *in vivo*

2.7.1 Cardiac CaViar for drug screening

Human iPSC-derived cardiomyocytes and zebrafish hearts have both been proposed as models for cardiac drug testing. In the case of nifedipine, the responses were dramatically different. Figure 2-8 illustrates typical single iPSC-derived cardiomyocyte response to nifedipine, an L-type calcium channel blocker. Nifedipine suppressed the L-type Ca^{2+} current responsible for maintaining the plateau of the AP. The Ca^{2+} trace at 100 nM showed blockage of the Ca^{2+} oscillations and a corresponding increase in beat rate, with further increases in rate occurring at higher concentrations.

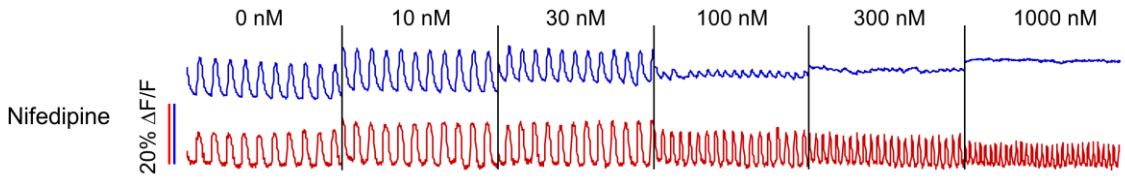

Figure 2-8: Effect of nifedipine in cardiomyocytes expressing CaViar
Calcium transients (*blue*) and voltage transients (*red*) at increasing concentrations of nifedipine.

1 μM nifedipine induced severe tachycardia (from a mean of 70 bpm to 228 bpm, n = 28 cells), while in the zebrafish heart at 102 hpf, 10 μM nifedipine induced bradycardia (from a mean 107 bpm to 93 bpm, n = 17 fish). While the effect of nifedipine on beat rate in the hiPSC culture

is consistent with its clinical effects, the underlying mechanism is likely to be different: cultured hiPSC-derived cardiomyocytes show spontaneous pacemaker activity which is sped up by drug-induced shortening of the action potential. In humans, nifedipine-induced tachycardia is a reflex secondary to arterial vasodilation.

Recently developed mutants of Arch respond in less than 1 ms and have improved sensitivity and membrane trafficking [46]. Ca^{2+} indicators with improved sensitivity and kinetics (GCaMP6f) have also recently been reported [47]. These improved indicators open the possibility to make transgenic mouse and iPSC lines stably expressing multi-function reporters. Human patient-derived cell lines with genetic defects such as long-QT syndrome as well as other channelopathies will be particularly useful for drug screening. Future work will also focus on development of hardware for improved three-dimensional [48] and high throughput [49] imaging. Higher speed voltage indicators will be particularly useful in studies on mouse cardiomyocytes, where the AP is shorter than in human or zebrafish. Co-expression of Arch(D95N) or CaViar with channelrhodopsin will enable optical pacing with simultaneous optical monitoring of physiological responses. Simultaneous application of multiple optogenetic modalities will enable relation of an ever-growing number of physiological quantities in the heart.

2.7.2 Cardiac CaViar to investigate unique zebrafish cardiology

The ability to measure voltage and Ca^{2+} simultaneously *in vivo* in the developing zebrafish heart opens the possibility to study the effects of genetic and pharmacological perturbations on development, on excitation-contraction coupling, and on Ca^{2+} handling. Comparisons of V_m and Ca^{2+} dynamics with and without contraction (modulated via blebbistatin or *silent heart* mutation) enables studies on mechanisms of mechano-electrical feedback *in vivo* [50].

Human cardiomyocytes are incapable of proliferating, and cardiac injury due to ischemic reperfusion, myocardial infarction, and chronic high blood pressure lead to permanent cardiac tissue death and scarring. In contrast, zebrafish are able to regenerate, even after 20% ventricular amputation [51, 52]. Recently, Zhang *et al*. found that cardiac reprogramming via Notch signaling enabled atrial cardiomyocytes to transdifferentiate into ventricular cardiomyocytes following ventricular ablation [53]. But what are the voltage dynamics during the migration of the transdifferentiating atrial to ventricular cells? Do these cells electronically decouple from the excitation-contraction of the syncytium? How does the waveform evolve during the process? CaViar might be able to answer some of these questions.

Finally, we are interested in observing the voltage dynamics during the earliest heart beats. Low expression levels of our current CaViar construct, *cmlc2*:CaViar at the onset of heartbeat results in low Arch signals. Expression of CaViar under an early heart promoter, such as *nkx2.5* [54], could solve this issue.

2.7.3 CaViar expressed in other cell types

One should not limit application of CaViar to studies of the heart. Action potentials are easily attributed to voltage, because its effect results in easily measured or observed quantities – an electrical current or a mechanical contraction. However, less obvious effects of voltage and calcium dynamics potentially drive many biological processes, as voltage across a membrane inevitably influences the local fields felt by all membrane associated proteins and molecules.

Ideally, one would like to observe voltage and calcium dynamics in any cell, at any time in development. A recent paper reported the use of the *Olactb* promoter from the medaka fish to drive ubiquitous transgene expression in zebrafish [55]. The authors showed that the one-cell

embryo maternally inherited the protein driven under the *Olactb* promoter, and thus, all developmental stages could be observed

We recently created a transgenic fish expressing CaViar under this promoter. Preliminary data has indicated functional expression of GCaMP5. The turn on of blue fluorescent light for imaging elicited a contractile response from the body of the zebrafish (Figure 2-9). The Vagus nerve near the heart also lit up in conjunction with the contraction (t = 20, 40, and 60 ms). While further experiments will be necessary to troubleshoot the Arch expression, we hope that this study will allow us to simultaneously monitor voltage and calcium dynamics in all stages of development over the entire fish.

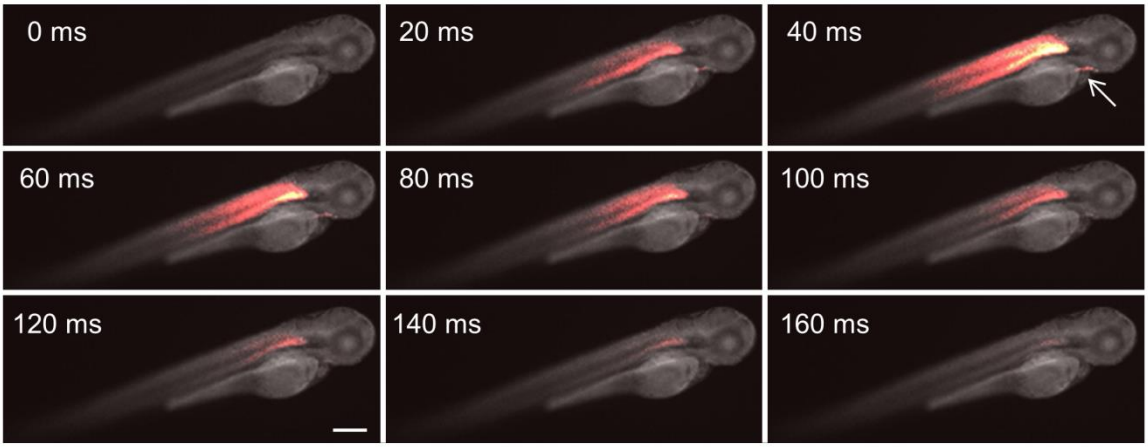

Figure 2-9: Zebrafish expressing CaViar under a ubiquitous promoter
GCaMP5 expressed in the body of the zebrafish lit up during a muscular contraction under 488 nm illumination. The Vegas nerve (*arrow*) also showed a calcium response. Scale bar is 250 μm.

There are also ongoing efforts to simultaneously image calcium and voltage dynamics in endothelial cells of zebrafish. Using the *cloche* mutant, which inhibits endothelium development, Milan *et al.* found that endocardial signaling is required for the development of AV conduction tissue [41]. In addition to studying endothelial cells near the heart, driving expression of CaViar

under an endothelial promoter such as *flk1* would allow study of potential electrical signals in the entire vascular system, which is only possible with a genetically encoded optical voltage indicator.

2.8 Materials and Methods

2.8.1 Molecular cloning

For expression in zebrafish, Arch(D95N)-eGFP and Arch(D95N)-GCaMP5G were amplified by PCR from pJMK019 and cloned into the *Spe*1 site of a Gateway (Life Technology) destination vector, which contained Tol2 transposase recognition sequences. The *cmlc*2 enhancer sequence was amplified and BP-cloned into a compatible entry vector. The resulting entry and destination clones were then LR-reacted to make *cmlc*2:Arch(D95N)-eGFP and *cmlc*2:Arch(D95N)-GCaMP5G expression vectors.

2.8.2 Zebrafish breeding

Adult zebrafish (strain AB) were raised and bred at 28.5 ºC according to standard methods. All experiments were conducted in accordance with Harvard IACUC protocols. Single-cell embryos were injected with a mixture of either *cmlc*2:Arch(D95N)-eGFP or *cmlc*2:Arch(D95N)-GCaMP5G and Tol2 mRNA, each at a concentration of 30 ng/µL, and raised to adulthood. A transgenic line was identified by screening progeny for cardiac GFP or GCaMP5G fluorescence, and was subsequently used for all imaging experiments.

2.8.3 Imaging zebrafish hearts

For imaging transgenic zebrafish, embryos were reared in E3 (5 mM NaCl, 0.17 mM KCl, 0.33 mM $CaCl_2$, 0.33 mM $MgSO_4$) containing 0.003 % 1-phenyl-2-thiourea to prevent

melanization. Embryos were manually dechorionated and mounted in 2% low melting point agar dorsal-side down (40 hpf or before) or ventral-side down (after 40 hpf) on #1 glass coverslips. Heart contraction was arrested by incubating the mounted embryos in 50 μM blebbistatin for two hours prior to imaging.

A 4 mM stock of all-*trans* retinal was made in 33% propylene glycol and 45% (2-hydroxypropyl)-B-cyclodextrin solution. For imaging fish before 48 hpf, larvae were soaked in a 1:1000 dilution of this stock in E3 for 9-12 hours prior to imaging. After 48 hpf, fish did not require exogenous retinal supplementation for Arch imaging.

Confocal images were acquired on a modified Yokogawa CSU-X1 spinning disk unit attached to an Olympus IX71 inverted base. Samples were illuminated by solid state lasers at 488 nm (Coherent Obis, 50 mW) with intensity 0.45 W/cm^2 and at 635 nm (Dragon laser, 300 mW) with intensity 40 W/cm^2, via a custom dichroic (Chroma Technology) optimized for 488/640 illumination. Imaging was performed with a 20x water-immersion objective with coverslip correction (Zeiss Plan-Apochromat NA 1.0). Emission fluorescence passed through a quad-band filter (Chroma NC264505-ZET405/488/532/642m) before being split by a home-built dual-view system that projected emission of wavelengths < 540 nm and > 640 nm onto adjacent halves of an EMCCD camera (Andor iXon X3, 512 x 512 pixels). Exposure times varied between 8 – 50 ms. A piezoelectric objective scanner (PIFOC PD72Z4CA0) was used to control the *z*-position of the sample. A custom LabView (National Instruments) script controlled illumination shutters, objective scanner and camera for automated data acquisition.

For the three-dimensional reconstruction of the zebrafish heart (Figure 2-1*c*), pairs of consecutive *z*-focal planes, separated by 5 μm, were recorded within a single movie, with typically ~10 beats recorded in each *z*-plane. Timing differences between successive focal planes were calculated

from the phase shift between the first and second halves of each movie (Figure 2-10). Maps of action potential propagation within each *z*-plane were constructed via temporal registration and averaging of recordings of ~10 beats. Data from all *z*-planes was combined to create a 4-D (*x*, *y*, *z*, *t*) movie of AP propagation. The boundary of each *z*-plane was segmented and used in the Matlab software package iso2mesh [56] for volumetric rendering of the zebrafish heart. A modified version of this software enabled color to reflect the voltage intensities derived from the mean AP data.

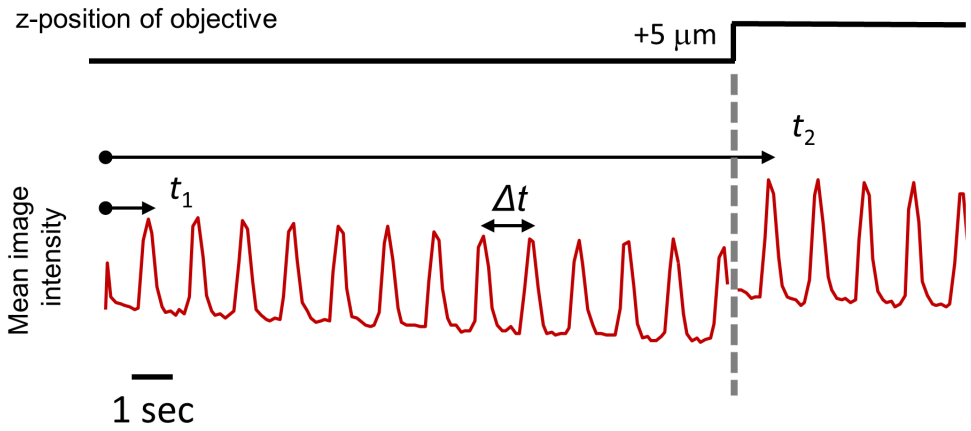

Figure 2-10: Continuous image acquisition during a change in focal plane allowed 3-D reconstruction
t_1 and t_2 represent the clock time of the first peak for each *z*-position, and Δt is the mean period between peaks. Then (t_1-t_2) mod Δt gives the phase shift between consecutive planes.

Chapter 3 Temporal dynamics of microbial rhodopsin fluorescence reports absolute membrane voltage

3.1 Introduction

Section 2.7.3 suggested that membrane voltage dynamics play a ubiquitous role in membrane-associated processes. Indeed, any lipid membrane can, in principle, support a membrane voltage. This voltage modulates the free energy landscape of all charged proteins and small molecules associated with the membrane [57]. While membrane voltage is well known to regulate the activity of ion channels, voltage also regulates activity of phosphatases [58], G-protein coupled receptors [59], and redox proteins [60]. Bacteria, fungi, plants, and animal cells dynamically regulate voltage in the plasma membrane and in intracellular organelles. Resting potentials range from as low as -300 mV in *Neurospora crassa* [61], -180 mV in mitochondria [62], -140 to -80 mV in *E. coli* [63], -90 mV to -65 mV in cardiomyocytes and neurons, to near 0 mV in undifferentiated stem cells [64–66].

Genetically encoded fluorescent reporters of membrane voltage enable non-invasive optical monitoring of electrical dynamics in live cells. With recent advances in speed and sensitivity, one can now visualize single action potentials in neurons and cardiomyocytes, *in vitro [20, 67, 68]* and *in vivo* [38, 69, 70]. These intensity-based measurements report relative changes in membrane voltage, not its precise numerical value. This approach is appropriate for detecting fast action potentials and sub-threshold events, but not for measuring slower shifts in resting voltage, such as occur during embryonic development [71], stem cell differentiation [72], wound healing [73], programmed cell death [74], and plant responses to herbivory [75, 76].

One would like a means to map the numerical value of the membrane voltage in a sample over space and time. A reporter of absolute voltage should meet several criteria. The measurement should be insensitive to variations in reporter concentration, photobleaching, and background autofluorescence. The measurement should also be insensitive to the precise intensity of the illumination or the efficiency of the optical collection, as these parameters often differ between experiments. The reporter should be genetically targeted to facilitate measurements in defined sub-classes of cells within a heterogeneous population.

Dual-wavelength ratiometric imaging is sometimes used in attempts at accurate measurements. This strategy has been employed in fluorescent measurements of pH [77], Ca^{2+} [78, 79], kinase activity [80, 81], and voltage [82, 83]. The dye di-8-ANEPPS undergoes a voltage-dependent shift in emission spectrum which can be detected by simultaneous imaging in two emission bands. FRET-based voltage indicators in principle enable ratiometric measurements of absolute voltage [84, 85], but differential rates of photobleaching between the donor and acceptor make this difficult in practice. Dual-wavelength ratiometric measurements require careful spectral calibration of the apparatus and can be confounded by spectrally or spatially inhomogeneous background fluorescence. Due to the technical challenges of accurately quantifying fluorescence across multiple wavelengths, ratiometric indicators are not widely used for absolute voltage measurements.

In contrast to measurements of intensity, measurements of time can be both precise and accurate. A common strategy for detecting a small signal on a large and inhomogeneous background is to encode the information in the time domain. Fluorescence lifetime imaging microscopy uses changes in the electronic excited state lifetime to report on subtle environmental changes that are not apparent from the raw fluorescence intensity. This technique has been used

effectively to measure calcium concentrations and enzymatic activity in dendritic spines [86, 87]. We sought to encode voltage information into a time-domain optical signal.

Retinal-binding proteins are emerging as a new class of genetically encoded optical reporters [88]. We recently reported that microbial rhodopsins can serve as fast and sensitive, but dim, fluorescent voltage indicators [20, 89]. Electronic excited state lifetimes of rhodopsins are < 100 ps [90], too short to use as a contrast mechanism in imaging. However, these proteins also undergo slower dynamics: they have a complex conformational landscape, with states connected by voltage- and light-dependent transitions [24, 91, 92]. In wild-type Archaerhodopsin 3 (Arch), continuous illumination produces a voltage- and wavelength-dependent photostationary distribution among the states. A change in voltage alters the photostationary distribution and leads to a change in fluorescence. We reasoned that a change in illumination wavelength, with constant voltage, would also change the photostationary distribution. The trajectory of the relaxation to the new distribution might report absolute membrane voltage.

In the mutant Arch(D95H), voltage affected both the amplitude and timecourse of the fluorescence response to a step change in illumination wavelength. These quantities provided a measure of absolute voltage that was insensitive to expression level, precise illumination intensity, or precise collection efficiency. We demonstrated this technique in Human Embryonic Kidney (HEK) cells.

3.2 Search for a promising Arch-based absolute voltage reporter

Voltage-sensitive fluorescence in microbial rhodopsins is believed to arise from changes in protonation of the retinal Schiff base. The protonated state is fluorescent, the deprotonated state is not, and voltage controls the local electrochemical potential of protons and hence this acid-base

equilibrium [24]. Aspartic acid 95 in Arch (homologous to Asp85 in bacteriorhodopsin) is the counterion to the Schiff base, and thus plays a key role in modulating protonation of the Schiff base. In a search for improved fluorescent voltage indicators, we generated a library of twenty Arch mutants by saturation mutagenesis at Asp95. We screened the twenty mutants for voltage-sensitive fluorescence by expressing and imaging them in "spiking" HEK cells that had been genetically engineered to generate spontaneous electrical action potentials [93]. Seven showed voltage-sensitive fluorescence. Of these, Arch(D95H) was the most sensitive.

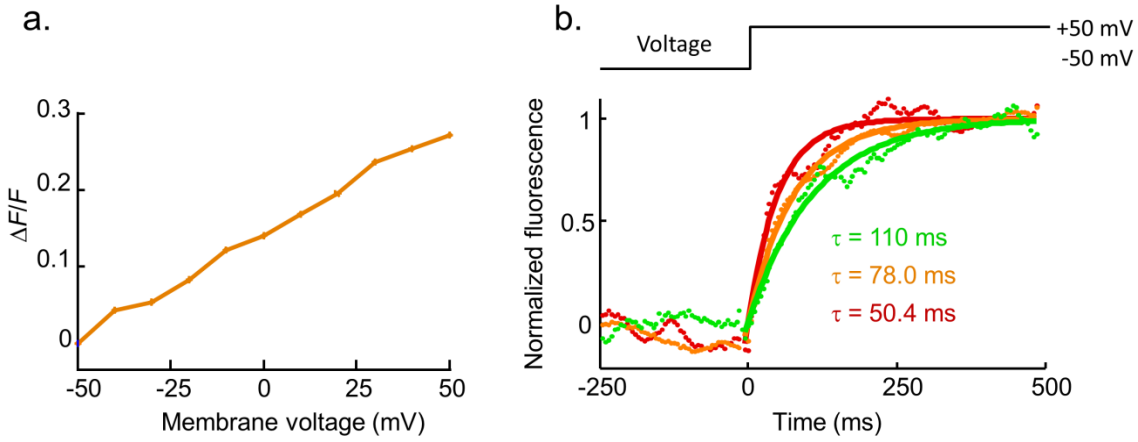

Figure 3-1: Arch(D95H) is a fluorescent voltage indicator
(*a*) Steady-state fluorescence response of Arch(D95H) to a ramp in membrane voltage under 594 nm illumination. (*b*) Fluorescence response of Arch(D95H) to an instantaneous step in membrane voltage from V_m = -50 mV to V_m = 50 mV under 532 (*green*), 594 (*orange*), and 638 (*red*) nm illumination. The time constant τ for the response was dependent on illumination wavelength.

We expressed the fusion Arch(D95H)-eGFP in standard (non-spiking) HEK293 cells and tested the response of Arch fluorescence (λ_{ex} = 594 nm, λ_{em} > 664 nm) to a ramp in membrane voltage applied via a patch pipette. Fluorescence increased 30% from V_m = -50 mV to V_m = 50 mV (

Figure **3-1***a*). The fluorescence response to a 100 mV step in voltage was illumination wavelength dependent with time constants τ of 110, 78.0, and 50.4 ms, for 532, 594, 638 nm illumination, respectively (

Figure **3-1***b*). The protein generated an outward photocurrent of 5 pA, which perturbed membrane voltage by < 1 mV. In contrast, wild-type Arch excited at its absorption peak has been reported to pass a proton current of nearly 1 nA [94]. This large proton current perturbed intracellular pH by 0.15 pH units; thus we infer that the pH perturbation from the 200-fold smaller Arch(D95H) photocurrent was negligible.

3.3 Ratiometric voltage indicators are confounded by differential photobleaching

We explored several strategies for using Arch(D95H) as an absolute voltage indicator. We first tested the eGFP fusion as a prospective dual-wavelength ratiometric indicator. We simultaneously imaged the fluorescence of Arch(D95H) (λ_{ex} = 638 nm, λ_{em} = 660 - 875 nm) and of eGFP (λ_{ex} = 488 nm, λ_{em} = 510 - 530 nm) using a dual-view spinning disk confocal imaging system. We adjusted laser intensities to achieve similar photon count rates in both channels. Figure 3-2*c* shows fluorescence of Arch(D95H) and of eGFP as a function of time under constant membrane voltage. eGFP photobleached faster than Arch(D95H), so this ratio could not be used as a robust measure of absolute voltage.

We further tested whether voltage-dependent shifts in the emission spectrum of Arch(D95H) could provide a measure of absolute voltage. We used an imaging spectrometer to record fluorescence emission spectra of Arch(D95H) at -100, 0, and +100 mV (λ_{ex} = 594 nm, λ_{em} > 664 nm). The emission spectrum did not exhibit detectable voltage-dependent shifts, and thus

was unsuitable as a measure of absolute voltage (Figure 3-2*d*). This finding was consistent with a model of microbial rhodopsin fluorescence in which emission is dominated by a single state whose population is regulated by voltage [24].

We next tested the seven fluorescent and voltage-sensitive D95X mutants for dynamic changes in fluorescence in response to changes in illumination wavelength. We hypothesized that such changes indicated a photocycle topology in which the photostationary distribution depended on illumination as well as voltage, a possible route to a time-domain encoder of absolute membrane voltage. Arch(D95H) showed the biggest fluorescence transients and so we characterized its dynamics in more detail.

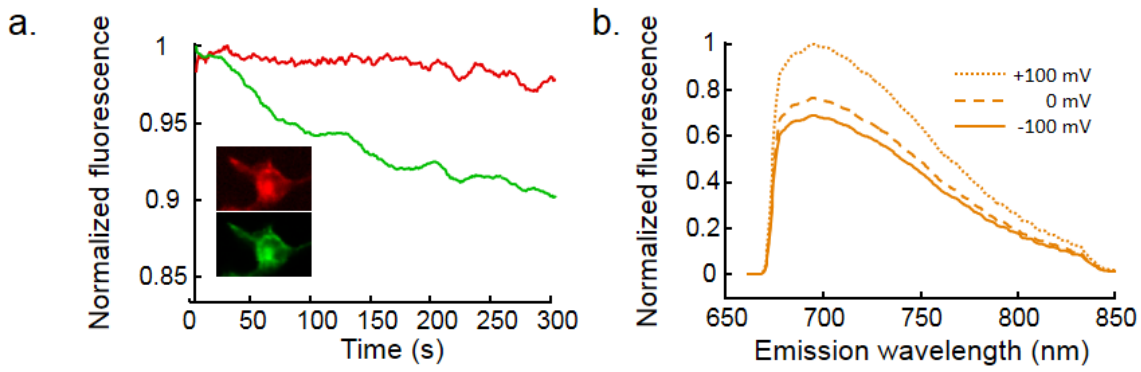

Figure 3-2: Ratiometric imaging does not give a measure of absolute voltage
(*a*) Dual-indicator ratiometry was not robust to differential photobleaching. Under simultaneous illumination at 488 and 638 nm, eGFP (*green*) photobleached faster than Arch(D95H) (*red*). Laser intensities were adjusted to achieve similar initial photon count rates from the two chromophores. (*Inset*) Dual-view spinning disk confocal images of HEK293 expressing Arch(D95H) (*top*) and eGFP (*bottom*). (*b*) Emission spectra of Arch(D95H) changed only in amplitude, and not shape, when membrane voltage was varied from -100 (*solid*), 0 (*dashed*), and +100 (*dotted*) mV.

3.4 Optimization of a robust absolute voltage measurement

We tested whether the relaxation between different photostationary distributions in Arch(D95H) contained information on the membrane voltage. Our goal was to discover some measure, *M*, that could be computed from the time-dependent fluorescence and that would have a robust one-to-one mapping to absolute membrane voltage.

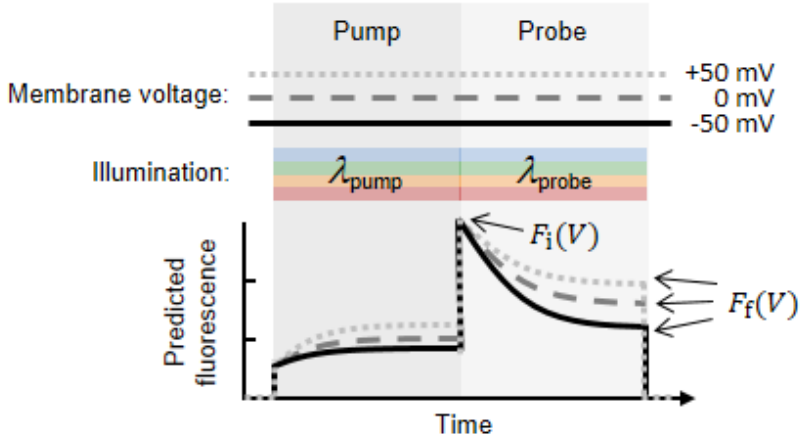

Figure 3-3: Schematic of pump-probe experiment
Sample was held at constant membrane voltage V_m and illuminated sequentially by light of wavelengths (λ_{pump}, λ_{probe}). Fluorescence relaxation during the probe interval depended on V_m, λ_{pump}, and λ_{probe}.

We used whole-cell patch-clamp to set the membrane voltage of an isolated HEK cell to one of three constant values (V_m = -50, 0, or +50 mV). The cell was illuminated at wavelength λ_{pump} for time t_{pump}, immediately followed by wavelength λ_{probe} for time t_{probe} (Figure 3-3*a*). Fluorescence of Arch(D95H) was recorded throughout the pump and probe intervals. We searched for wavelength pairs (λ_{pump}, λ_{probe}) where the relaxation of the fluorescence during the probe interval showed voltage dependence.

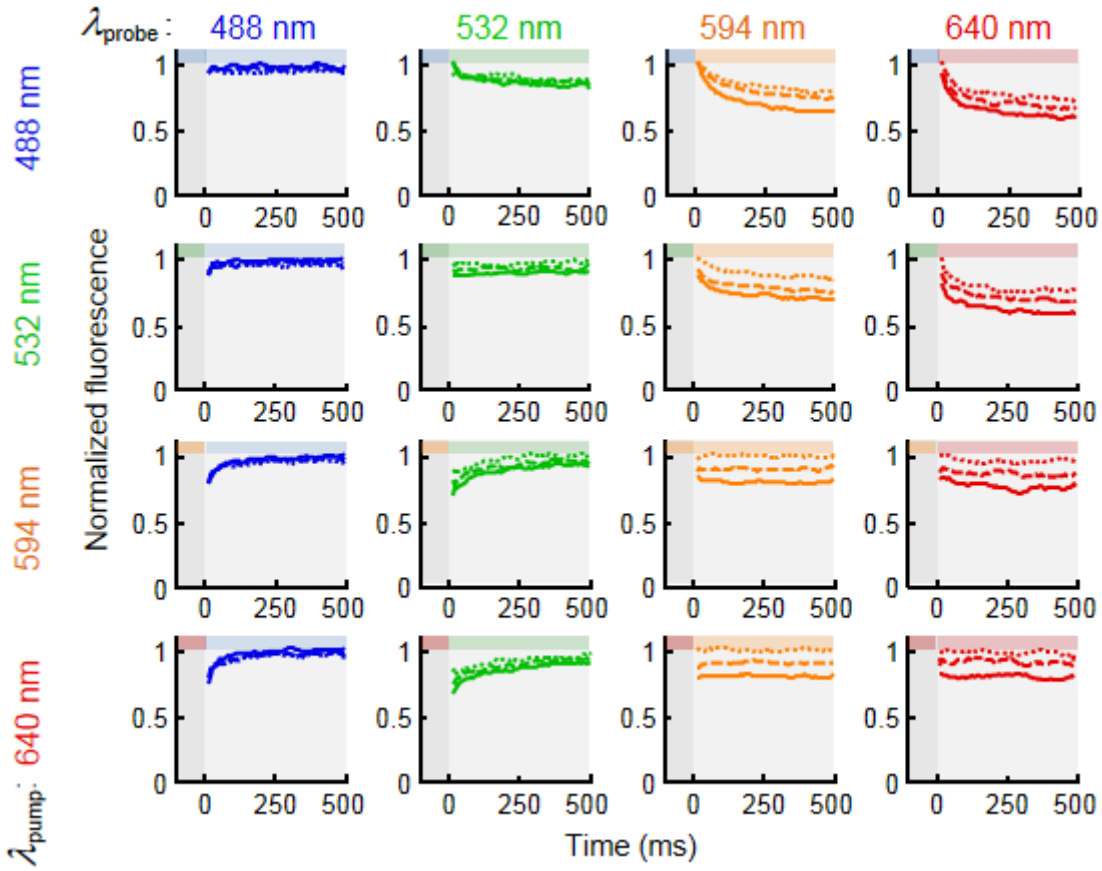

Figure 3-4: Probe intensity traces of HEK293 expressing Arch(D95H)-eGFP, voltage-clamped at three voltages
16 (λ_{pump}, λ_{probe}) pairs using 488, 532, 594, and 638 nm at V_m = 50 (*solid*), 0 (*dashed*), +50 (*dotted*) mV were tested to find the largest differential response between high and low V_m. Data presented are representative traces from n = 5 cells.

We measured relaxation of the fluorescence for sixteen pairs of pump and probe wavelengths, each at three voltages (Figure 3-4). We quantified the fluorescence transient during the probe by the dimensionless metric

$$M(V_m) \equiv \frac{F_i(V_m) - F_f(V_m)}{F_f(V_m)} \tag{3-1}$$

where $F_i(V_m)$ and $F_f(V_m)$ represent the initial and final fluorescence intensities during the probe interval, respectively (*arrows* in Figure 3-3). This metric was designed to be independent of illumination intensity and expression level, *i.e.* multiplying F_i and F_f by the same constant does

not change M. However, variations in voltage-insensitive background could confound measurements of $M(V_m)$, *i.e.* adding a constant to F_i and F_f changes M. For the present measurements on HEK cells via confocal microscopy, background was negligible. An alternative metric based on a voltage-dependent rate constant is insensitive to background and is explored below.

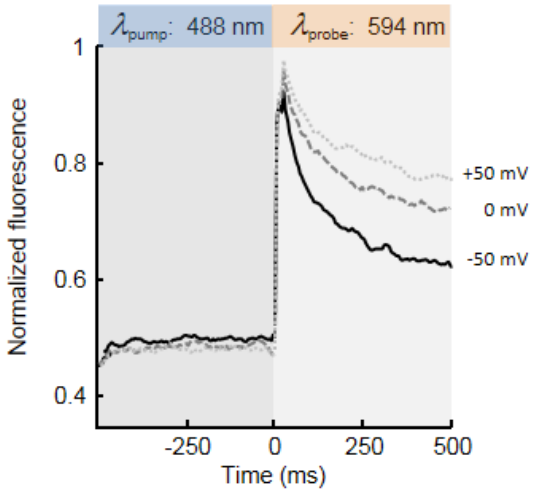

Figure 3-5: Probe intensity trace of favorite wavelength pair
The wavelength pair (λ_{pump}, λ_{probe}) = (488 nm, 594 nm) resulted in intensity traces with the largest sensitivity to absolute membrane voltage. Data presented are representative traces from n = 5 cells.

Sensitivity to membrane potential was characterized by $\Delta M = M(V_m = -50\text{ mV}) - M(V_m = +50\text{ mV})$. The wavelength pair ($\lambda_{pump}$, λ_{probe}) = (488 nm, 594 nm) gave the largest value of ΔM (Figure 3-5). Under blue illumination, the fluorescence showed almost no sensitivity to voltage. This insensitivity to voltage did not change immediately upon switching to orange illumination. Instead, the fluorescence became sensitive to voltage with a time constant of ~100 ms. This observation suggests that the blue photostationary distribution was not influenced by voltage while the orange one was.

We noticed that the initial fluorescence upon illumination at 594 nm depended on the previous illumination, even when the two illumination periods were separated by a dark interval (Figure 3-6*a*). This observation implied that the conformational landscape divided into two regions that only interconverted slowly, if at all, in the dark, but that reached a voltage- and illumination-dependent equilibrium in the light. Thus we adapted the illumination scheme to include a dark interval between pump and probe pulses (Figure 3-6*b*). We reasoned that a dark interval would facilitate relaxation within each sub-manifold, and could allow voltage-dependent processes to occur in the dark. A dark interval could potentially increase the influence of voltage on the temporal dynamics of fluorescence during the probe.

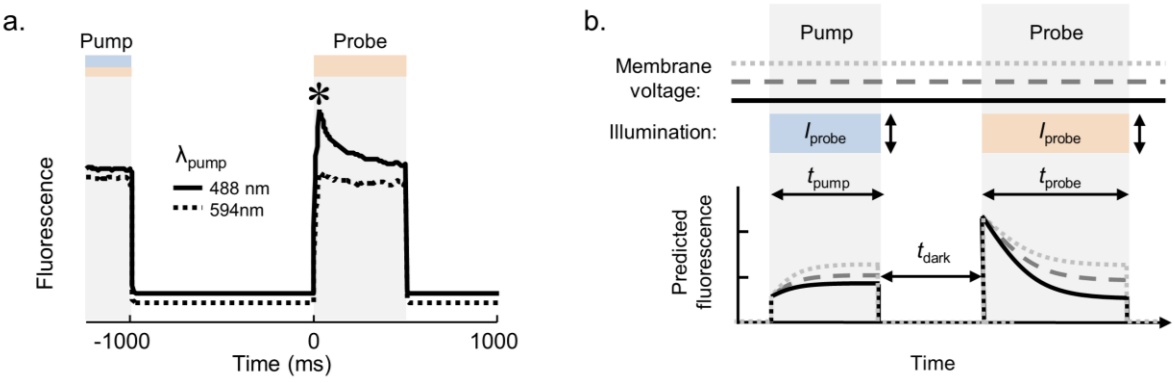

Figure 3-6: Bistability of Arch(D95H) prompts addition of a dark interval in illumination scheme
(*a*) Optical bistability in Arch(D95H). Initial fluorescence upon illumination at 594 nm (*) depended on the wavelength of the preceding illumination, even when separated by a dark interval. Traces are vertically offset for clarity. (*b*) Schematic of pump-probe experiment with the inclusion of a dark interval. Parameters t_{pump}, t_{dark}, t_{probe}, I_{pump}, and I_{probe} were explored.

We measured fluorescence transients as a function of t_{pump}, t_{dark}, t_{probe}, intensities I_{pump} and I_{probe}, and membrane voltage V_m (Figure 3-6*b*). Over the range of t_{pump} explored (1 - 500 ms), fluorescence during the probe interval depended only on I_{pump} and t_{pump} through their contribution to the total fluence, $f_{pump} = I_{pump} \times t_{pump}$. ΔM increased with f_{pump} but showed saturation behavior with a half-maximal fluence of 1 J/cm^2. By choosing a pump fluence well into the saturation

regime (I_{pump} = 40 W/cm^2, t_{pump} = 100 ms), measurements of M became robust to variations in I_{pump}. We varied t_{dark} from 0 to 2 s and found that ΔM was maximal for t_{dark} = 1 s, but varied by only 10% over this range.

a.

Optimal illumination parameters

	Pump	*(dark)*	Probe
λ (nm)	488	N/A	594
Time (ms)	100	1000	750
Intensity (W/cm^2)	40	N/A	80

b.

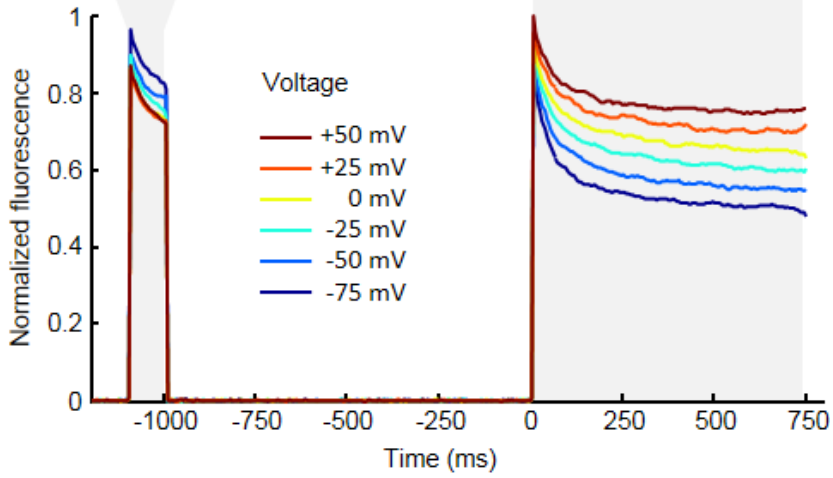

Figure 3-7: Pump-probe experiment with optimal illumination scheme
(*a*) Optimal parameters of time, wavelength, and intensity for sensitivity to voltage. (*b*) Normalized fluorescence traces of Arch(D95H) during the optimized pump-probe experiment showed desired voltage sensitivity. Each trace represents an average over 12 trials with the sample voltage-clamped at the indicated membrane voltage. The single-trial standard deviation in M was $\delta M/M$ = 13%.

To achieve adequate fluorescence intensity during the probe interval, we operated at $I_{probe} \geq 80$ W/cm^2. In this regime, fluorescence was directly proportional to I_{probe}, so M was independent of probe intensity. The probe interval was selected to be long enough for fluorescence to reach steady state; we used $t_{probe} \geq 750$ ms.

With these optimal pump-probe parameters (Figure 3-7*a*), we measured the fluorescence relaxation during the probe at six voltages, between V_m = -75 mV and 50 mV (Figure 3-7*b*). We observed a two-fold change in $M(V_m)$ over this range.

To test the robustness of our absolute voltage measurement, we measured $M(V_m)$ in six cells from three dishes, using the illumination and timing parameters shown in Figure 3-7*a*. For each cell, we used patch-clamp to vary V_m between -75 mV and 50 mV. Expression levels of the indicator varied widely between cells; and hence, the plots of steady-state fluorescence vs. membrane voltage also varied widely between cells (Figure 3-8*a*).

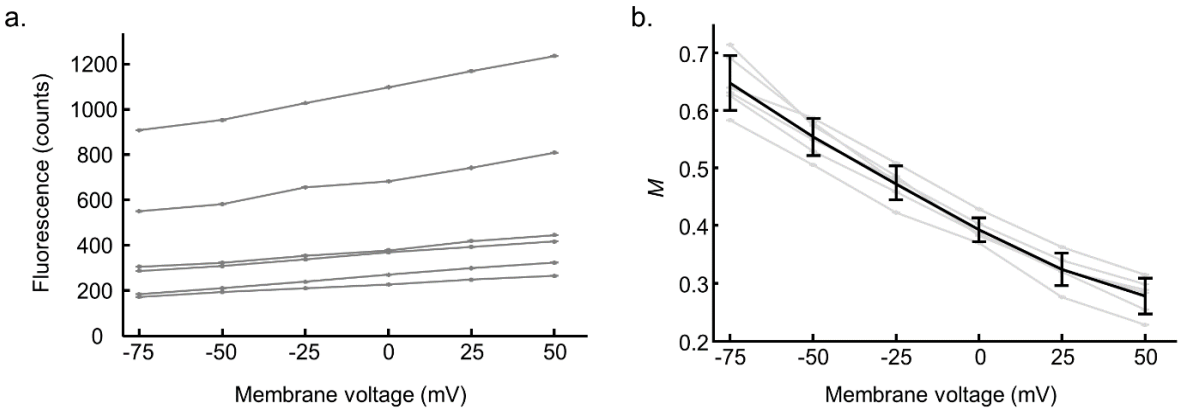

Figure 3-8: Time-domain response of Arch(D95H) gives a robust measure of absolute voltage
(*a*) Steady-state fluorescence of Arch(D95H) in six cells as a function of membrane voltage. Due to wide variations in protein expression levels, absolute fluorescence was not a robust measure of absolute voltage. (*b*) Time-domain response of Arch(D95H) under the illumination parameters of Figure 3-7. The fractional amplitude of the fluorescence relaxation, *M*, reported voltage with an absolute accuracy of σ_V = 9.8 mV. Gray lines show $M(V_m)$ for the same six cells plotted in (*a*).

The dimensionless measure $M(V_m)$ showed significantly less cell-to-cell variation than did the raw fluorescence (Figure 3-8*b*). We asked how accurately one could estimate V_m from *M* in a

cell given no prior information. The error in the voltage estimate, σ_V, depends on the error in the measurement of M, σ_M, by

$$\sigma_V = \left\langle \frac{\sigma_M}{\left| dM / dV_m \right|} \right\rangle_{V_m} \tag{3-2}$$

The plot of $M(V_m)$ was approximately a straight line between -75 and +50 mV, so it was acceptable to take the average over all cells and all voltages. The accuracy of voltage measurements was σ_V = 9.8 mV.

The resistance of the plasma membrane is much greater than that of the cytoplasm, so HEK cells are expected to be electrotonically compact, i.e. the membrane voltage should be uniform throughout the plasma membrane. We used a spinning disk confocal microscope to acquire fluorescence images of the midplane of a HEK cell expressing Arch(D95H) and under patch clamp voltage control. Due to variations in the density of protein, raw fluorescence was not able to test for electrical homogeneity.

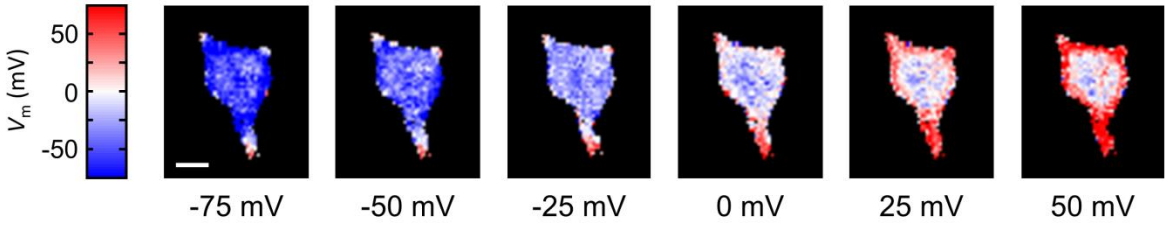

Figure 3-9: Pixel-by-pixel map of V_m using M vs. V_m calibration
Map of voltage in a spinning disk confocal image of a single cell. Colormap indicates distribution of V_m at six values of the applied voltage, as calculated from calibration in Figure 3-8*b*. The voltage-dependent pixels are predominantly localized to the periphery of the cell, as one would anticipate for a voltage sensor. Values in the interior of the cell are determined by a combination of fluorescence from internalized Arch(D95H) (not sensitive to membrane voltage) and out-of-focus Arch(D95H) localized to the dorsal and ventral plasma membranes. Scale bar represents 10 μm.

We applied the illumination scheme of Figure 3-7*b* and calculated a pixel-by-pixel map of *M*. From the map of *M* we made a map of V_m via the calibration in Figure 3-8*b*. Figure 3-9 shows a homogeneous membrane voltage throughout the plasma membrane. Inside the cell the membrane voltage was not a well-defined quantity. The calculated values were not sensitive to plasma membrane voltage, and were dominated by fluorescence from protein that had not trafficked to the plasma membrane.

3.5 Alternative parameterizations of fluorescence transients

The timecourse of the fluorescence transient also encoded information on the underlying membrane voltage. In principle, this timecourse might show complex multi-exponential voltage-dependent kinetics. For simplicity, we initially fit the transients to a single exponential decay, with voltage-dependent time constant τ. Figure 3-10 shows $\tau(V_m)$. The dependence on V_m is weak. Thus, for Arch(D95H), relaxation rate was not a useful measure of absolute voltage.

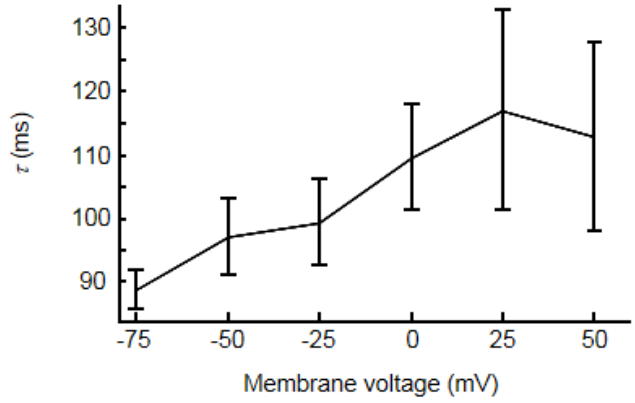

Figure 3-10: Voltage-dependent time constant of fluorescence relaxation in Arch(D95H)

M as defined by Equation (3-1) was chosen to capture the observed voltage-dependent shifts in the fluorescence dynamics. However, one might imagine that in Arch(D95H) or in other

candidate indicators, the fluorescence dynamics could vary with voltage in a complex way. In the absence of a detailed kinetic model (which can be laborious to infer for each mutant), it is not *a priori* obvious how to parameterize voltage-dependent changes in the transient waveforms. We sought a means to achieve this parameterization in a model-independent way.

We used Principal Component Analysis (PCA) to find a basis of reduced dimensionality that accounted for the voltage-dependent variation in the fluorescence transients. This approach does not assume a particular response function. We generated the principal components from a "training set" of fluorescence transients $F(V_m, t)$ in $n = 6$ cells, measured at membrane voltages V_m = -50, -25, 0, 25, 50 mV. We calculated the covariance

$$E(t,t') = \sum_{V_m} \left(F(V_m,t) - \overline{F}(t)\right)\left(F(V_m,t') - \overline{F}(t')\right) \tag{3-3}$$

where $\overline{F}(t)$ is the mean of $F(V_m, t)$ averaged over all tested values of V_m. The eigenvectors of the covariance matrix $E(t, t')$ yielded the set of principal components $P_i(t)$ that represent the variations between the individual fluorescence transients and the mean. For Arch(D95H), > 98% of the variation was accounted for by the first principal component $P_1(t)$. Using $\overline{F}(t)$ and $P_1(t)$ as basis functions (Figure 3-11*a*), we described the time-domain fluorescence $F(V_m, t)$ of Arch(D95H) by two parameters *a* and *b*:

$$F(V_m,t) = a\overline{F}(t) + b(V_m)P_1(t)\,. \tag{3-4}$$

For each data trace, we used a least-squares linear regression to determine the values of *a* and *b* that minimized the residual

$$\sum_t \left(F(V_m,t) - \left(a\overline{F}(t) + b(V_m)P_1(t)\right)\right)^2\,. \tag{3-5}$$

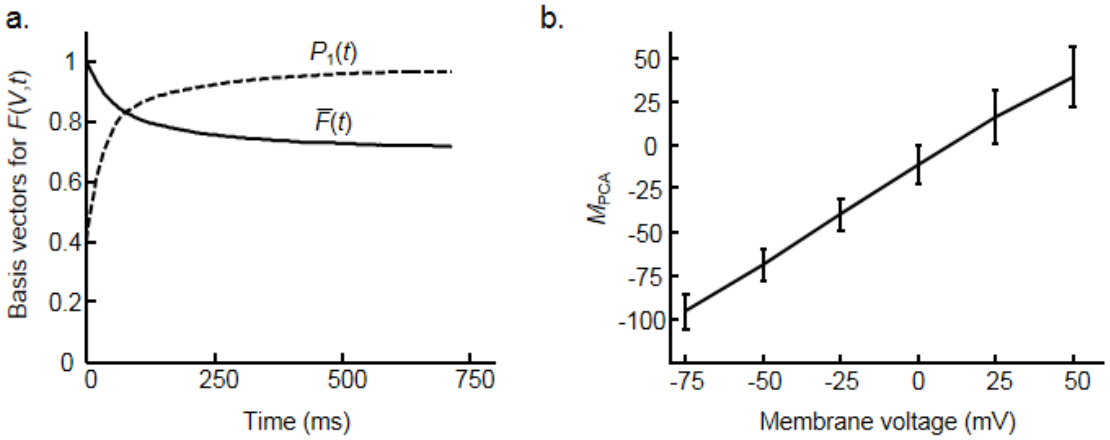

Figure 3-11: Parameterization of time-domain response using Principal Component Analysis

(*a*) Mean $\bar{F}(t)$ (*solid*) and first principal component $P_1(t)$ (*dashed*) time-domain responses of Arch(D95H) during the probe interval. >98% of the variation due to differences in membrane voltage was accounted for by the first principal component. (*b*) Time-domain response of Arch(D95H) parameterized by M_{PCA} was a robust measure of absolute voltage. PCA provided a general approach for extracting absolute voltage measurements from a fluorescence time-trace.

Both a and $b(V_m)$ depend on the illumination intensity and collection efficiency with the same prefactor. Therefore, the quantity $M_{PCA}(V) = b(V_m)/a$, is expected to be a robust measure of absolute voltage, independent of probe intensity or expression level. We found that M_{PCA} reported absolute voltage with accuracy $\sigma_V = 10.5$ mV, similar to the quantity M with the phenomenological definition of Equation (3-1) (Figure 3-11*b*).

In the present study, we accounted for variations in background by a combination of confocal imaging to reject out of focus fluorescence and background subtraction. However, in cases where these techniques are not possible, one could add a constant offset c to the fit in Equation (3-4) to account for background. This approach requires that the background not show fluorescence transients too similar to those of membrane-bound protein—ideally the background should be static. In the case of Arch(D95H), the fluorescence background was dominated by

improperly trafficked protein, which still showed fluorescence transients. Under wide-field epifluorescence imaging, improperly trafficked protein could confound the signal. Ultimately, the solution should be to improve the trafficking of the protein.

The PCA-based analysis of fluorescence transients is applicable to any time-resolved measurement where the complexity of the underlying kinetics may prevent simple parameterization. This analytical approach will be useful in characterizing other reporters that encode absolute voltage in time-domain signals.

3.6 Conclusions and future directions

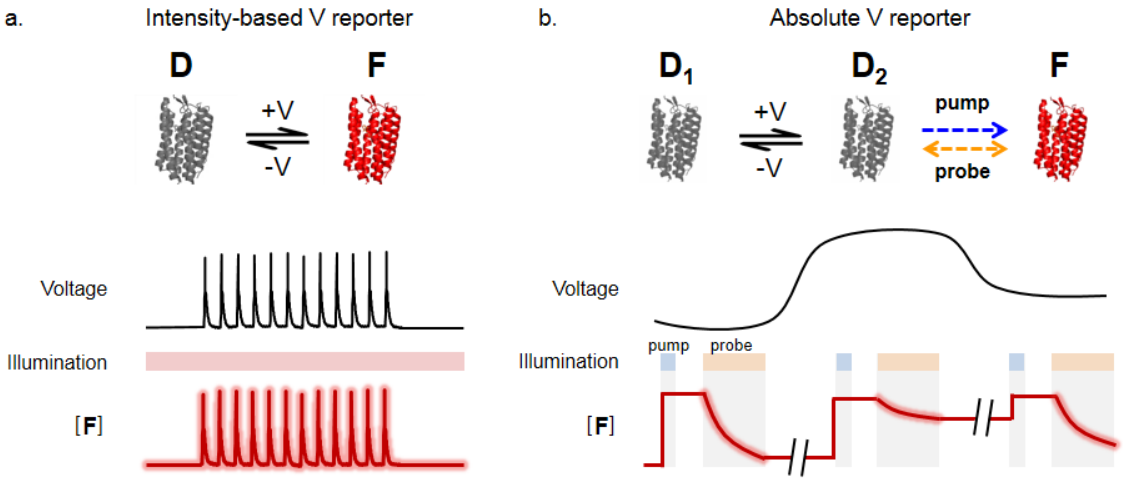

Figure 3-12: Comparison of intensity-based and absolute voltage reporters
(*a*) In an intensity-based voltage reporter, the membrane voltage determines the population of the fluorescent state *F*. Constant illumination excites fluorescence, but does not otherwise shift the equilibrium between *F* and dark state *D*. Fluorescence intensity serves as a reporter of voltage changes, but depends on illumination intensity, probe concentration, collection efficiency, and membrane voltage. (*b*) In an absolute voltage reporter, membrane voltage influences the equilibrium between two dark states D_1 and D_2. Illumination drives transitions between D_2 and fluorescent state *F*, toward a wavelength-dependent photostationary ratio of [*F*] to [*D*]. Time-varying illumination produces non-stationary distributions whose relaxation kinetics report a slowly varying absolute voltage.

Figure 3-12 contrasts the voltage sensing mechanisms of traditional intensity-based voltage reporters and our absolute voltage reporter. In these schematics, we highlight the key transitions relevant to voltage-sensitive fluorescence; each cartoon structure could correspond to a sub-manifold of conformational states. In an intensity-based reporter (Figure 3-12*a*), membrane voltage affects the equilibrium between a dark state *D* and a fluorescent state *F*, but the populations are independent of illumination. Continuous monochromatic illumination probes the population of *F*.

Figure 3-12*b* proposes a simple photocycle topology for an absolute voltage sensor. A voltage-dependent equilibrium exists between two non-fluorescent states, D_1 and D_2. The state D_2 can be optically interconverted into a fluorescent state, *F*. Blue light drives only the transition into *F*, while orange light drives transitions in both directions. In a measurement of absolute voltage, the blue pump pulse drives the whole population into *F*. This population persists in the dark and thus the initial fluorescence during the probe pulse is insensitive to voltage. The orange probe pulse gradually establishes a photostationary distribution between D_2 and *F*, while voltage establishes an equilibrium between D_1 and D_2. By the end of the probe pulse, the steady state fluorescence of *F* thus depends on voltage. Figure 3-12*b* illustrates three voltage measurements in a slowly changing sample: the first at a low voltage, the second at a high voltage, and the third at an intermediate voltage. The fractional change in fluorescence during the probe pulse, *M*, is a function of voltage but not of illumination intensity or protein concentration.

The simple photocycle topology of Figure 3-12*b* occurs as a motif within the voltage-dependent photocycle of wild-type Arch described in Ref. [24]. In the wild-type photocycle, the voltage-dependent equilibrium happens between non-fluorescent photocycle intermediates, while

the optically generated fluorescent state (termed *Q*) thermally relaxes back to the main photocycle. We propose that the mutation D95H preserved the overall photocycle topology but changed the rates. Many microbial rhodopsins show optical bistability [95], so the bidirectional optical switching in our model is biophysically plausible.

Measurements of membrane voltage using membrane-embedded reporters are subtly different from electrode-based measurements. Molecular reporters probe local electric fields; electrodes probe the total potential difference between the aqueous reservoirs on opposite sides of the membrane. These two quantities are not the same for two reasons. First, ionization of lipid headgroups induces a potential difference between the lipid surface and the adjacent bulk aqueous phase. This "surface potential" can differ between membrane faces as a result of differences in the density of ionizable lipid headgroups, or differences in ionic composition of the bulk phases. Second, oriented polar species at the lipid-solution interface induce a "dipole potential" between the aqueous phase and the inside of the membrane. Asymmetry in the dipole potential can also induce an internal electric field. Thus when the lipid composition or ionic environment differs between the two faces of the membrane, a strong unidirectional electric field can permeate the membrane even in the absence of a macroscopically measurable membrane potential [96].

Which parameter is "correct"—the local field or global potential? The answer depends on the process being studied. Equilibrium distribution of ions between the bulk phases depends only on the global potential difference. But conformational changes in transmembrane proteins depend on the local electric field. Interactions of soluble ions with transmembrane proteins are also sensitive to the potential profile in the double layer and in the membrane. Thus one should not anticipate perfect correspondence between optical and electrode-based voltage measurements. Indeed, differences between local field and global potential have been observed with organic

voltage-sensitive dyes and are proposed to be a means by which neurons generate spatially varying thresholds for ion channel activation [97, 98]. Internally generated membrane fields vary slowly compared to the timescale of an action potential, and thus are difficult to detect with reporters of relative voltage. Reporters of absolute voltage promise to elucidate mechanisms by which cells regulate intramembrane electric fields.

What phenomena might one study with the present accuracy of 10 mV? Bacterial resting membrane potential ranges from -80 to -140 mV depending on growth state and many environmental factors. Bacterial membrane voltage also undergoes "spikes" which may last up to tens of seconds and likely have voltage swings > 100 mV [89]. Direct electrode-based calibration of voltage reporters in bacteria has not been feasible, so an absolute reporter could quantify these phenomena. In the context of embryonic development, stem cells with membrane voltages near zero differentiate into electrically diverse tissues: fibroblasts with voltage near -65 mV, neurons with voltage near -70 mV, and cardiomyocytes with voltage near -90 mV. The dynamics and modifiers of these transitions in embryonic development are largely unexplored.

For absolute voltage measurements to become more broadly applicable, several aspects of the reporter need to be improved. Primarily, improved membrane trafficking will prevent conflation of intracellular membrane voltages with plasma membrane voltage, thereby simplifying data analysis and improving accuracy. Overall brightness and voltage-sensitivity are also important parameters to improve. Finally, the protein should have voltage- and illumination-dependent rates in its photocycle, and at least one fluorescent state. While we searched exhaustively at position 95 in Arch, a near-infinite variety of other Arch mutants await exploration; and Arch is but one of more than 5,000 known microbial rhodopsins [99]. It is likely that mutants with better performance can be found.

Photogenerated states of microbial rhodopsins have absorption spectra that are typically broad and overlapping. Thus, continuous illumination at a single wavelength likely induces a mixed population of states, not all of which might be desirable for our purposes. In principle, one could apply an arbitrarily complex sequence of pump wavelengths and intensities to steer the population toward a particular distribution of states or even a single state [100]. The dynamics of fluorescence under such an optical control scheme could provide improved measures of absolute membrane voltage.

Our PCA-based parameterization of the relaxation can account for an arbitrary temporal response without need for an underlying model of the protein's spectroscopic dynamics. Time-domain approaches to absolute voltage measurement hold promise to map subtle shifts in membrane voltage and local electric fields in many biologically important phenomena.

3.7 Future applications

3.7.1 Neuronal maturation

We hope to use this absolute voltage technique to track the maturation of a neuron from its pluripotent state. The pluoripotent cells have resting potentials near 0 mV, and mature neurons have resting potentials around -70 mV. What is the path by which this neuron polarizes? Is it affected by its neighbors, or by chemical signals? Our optical measurement of absolute voltage provides a non-invasive, non-fatal method of quantifying the membrane voltage. This allows us to repeat measurements over many spatial fields and over the course of weeks, from a single dish.

3.7.2 Development in zebrafish

Section 2.7.3 described the development of a zebrafish transgenic line expressing CaViar driven by the ubiquitous promoter *Olactb*. The absolute voltage reporter driven by *Olactb* would also be a powerful tool for studying voltage-dependent processes during development. Instead of tracking fast dynamical changes with CaViar, an *Olactb*: Arch(D95H)-eGFP construct would allow us to study the slow evolution of resting potential as the embryonic grows and matures. How do spatial gradients of resting voltage across an embryo affect development of organs, vasculature, and tissues? At what point do the various internal systems start to polarize to their mature resting potentials? Knowing the absolute voltage in a large number of cells *in vivo* was previously unattainable, and we believe our technique has overcome the barrier to begin investigating such questions.

3.8 Materials and methods

3.8.1 Molecular cloning

Arch(D95H)-eGFP was created during the generation of an Arch(D95X) mutant library in pET-28b via saturation point mutagenesis. Arch(D95H) was moved (Gibson Assembly, New England Biolabs) into a lentiviral mammalian expression vector (Addgene plasmid 22051 cut with the restriction enzymes *Bam*HI and *Age*I). The final construct consisted of Arch(D95H) fused to C-terminal eGFP, driven under a ubiquitin promoter. The construct is available on Addgene.

3.8.2 HEK293 cell culture

HEK293T cells were cultured and transfected as previously described in [24]. Briefly, HEK293T cells were grown in DMEM supplemented with 10% FBS and penicillin/streptomycin in a

37 °C incubator under 5% CO_2. Cells were grown to 50-70% confluency before transfection (Mirus Transit 293) with Arch(D95H)-eGFP. 24 hours later, cells were trypsinized and re-plated at a density of ~5,000-10,000 cells/cm^2 on Matrigel-coated coverglass bottom dishes (P35G-1.5-14-C, MatTek). Cell were allowed to recover for 24 hours before imaging. Although there was some retinal present in FBS, dishes were supplemented with all-*trans* retinal (5 μM) 1 - 2 hours prior to imaging.

3.8.3 Electrophysiology

Patch-clamp experiments were performed under conditions similar to those described in [24]. Briefly, pipettes were pulled from borosilicate glass capillary tubes (World Precision Instruments, 1.5 mm OD, 0.84 mm ID) via a Flaming/Brown style micropipette puller (Sutter Instruments, P-1000) and filled with intracellular buffer (125 mM potassium gluconate, 8 mM NaCl, 0.6 mM $MgCl_2$, 0.1 mM $CaCl_2$, 1 mM EGTA, 10 mM HEPES, 4 mM Mg-ATP, and 0.4 mM Na-GTP at pH 7.3; adjusted to 295 mOsm with sucrose). Pipette resistances were 5-10 MΩ. The silver pipette electrode and ground were rechlorided daily before experimentation. HEK293 cells were bathed in Tyrode's buffer (125 mM NaCl, 2 mM KCl, 3 mM $CaCl_2$, 1 mM $MgCl_2$, 10 mM HEPES, and 30 mM glucose at pH 7.3; adjusted to 305 mOsm with sucrose) for patch-clamp recordings. The liquid junction potential was compensated with the pipette immersed in the extracellular solution at zero pressure, prior to making a gigaseal with the cell membrane. Patch-clamp electrical parameters (pipette capacitance, access resistance, and membrane resistance) were recorded to ensure accurate control of the membrane voltage. All patch-clamp data were acquired in voltage-clamp mode under whole cell conditions, with a patch-clamp amplifier (Molecular Devices, Axopatch 200B).

3.8.4 Microscopy and image analysis

Figure 3-13 shows the experimental apparatus. This system comprised a spinning disk confocal microscope with up to four independently modulated laser lines. A patch-clamp apparatus controlled the membrane voltage in HEK cells expressing candidate indicators. Beams from solid state lasers at 488 nm (Coherent Obis, 50 mW), 532 nm (Coherent Compass 315M, 100mW), 594 nm (Cobalt Mambo, 100 mW), and 638 nm (CrystaLaser, 100 mW) were combined using dichroic mirrors (Semrock) and passed through an acousto-optic tunable filter (AOTF; Gooch & Housego 48058) that allowed for spectral and temporal control of sample illumination. Illumination was directed into a modified Yokogawa spinning disk confocal imaging system (CSU-X1) attached to an Olympus IX71 inverted base. Imaging was performed with a custom dichroic optimized for 405, 488, 594 nm excitation (Chroma). Maximum intensities after the objective (Zeiss 20x Plan-Apochromat NA 1.0) were 43 and 82 W/cm^2 for 488 and 594 nm, respectively. Emission fluorescence passed through a dual-band filter (Chroma) optimized for 488 and 594 excitation and collected on an EMCCD camera (Andor iXon X3, 512 x 512 pixels).

Alternatively, illumination was directed onto the sample via widefield epifluorescence with a 650 nm dichroic mirror (Semrock). Intensities at the sample were 175, 80, 184, 193 W/cm^2 for 488, 532, 594, 638 nm light, respectively. Emission fluorescence was filtered through a 664 nm long pass filter (Semrock) before collection by the same Andor camera.

A custom LabView (National Instruments) script along with a National Instruments DAQ (PCIe-6323) controlled the AOTF, patch-clamp amplifier, and camera for data acquisition. Data from images and current recordings were analyzed in MATLAB. Membrane-localized protein was separated from intracellular protein by selecting voltage-sensitive pixels corresponding to the plasma membrane via the method described in [20].

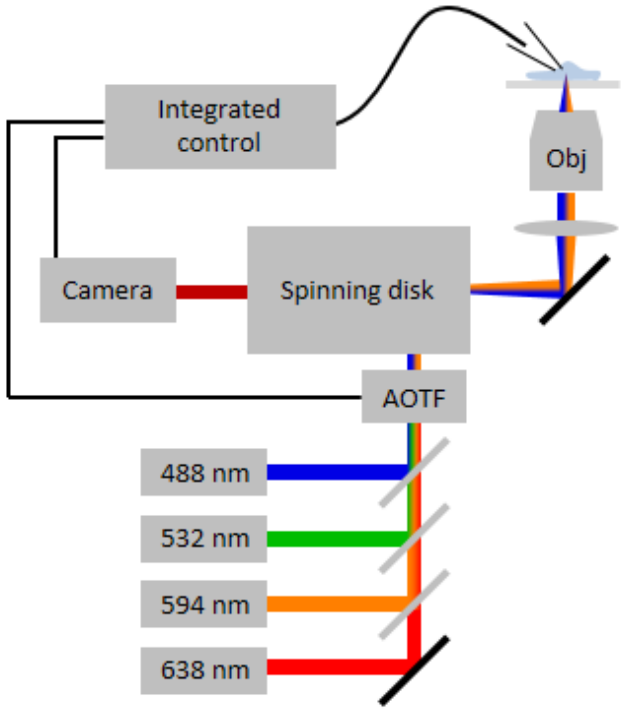

Figure 3-13: Imaging scheme with temporal control of illumination, patch-clamp amplifier, and camera for automated data acquisition

3.8.5 Voltage-dependent emission spectra

Emission spectra of Arch(D95H) were measured by placing an imaging spectrograph (Horiba iHR320) at the image plane of the microscope. Samples under voltage-clamp control were illuminated by 594 nm light (184 W/cm^2) via epifluorescence. Fluorescence was dispersed on a grating (100 grooves/mm) and then re-imaged on an EMCCD camera.

Chapter 4 Improvements on the Yokogawa spinning disk confocal imaging system

4.1 **Introduction**

Spinning disk confocal microscopy is a technique for imaging fluorescence from a single plane in a three-dimensional sample. Here, we describe the Yokogawa spinning disk microscope system, the standard brand used for spinning disk confocal microscopy (Figure 4-1). The essence of the technique is to scan a large number of tightly focused illumination spots across a sample. These focal spots are imaged onto an array of pinholes which passes fluorescence from the focal spots while rejecting out-of-focus fluorescence. A disk comprised of an array of confocal pinholes is mounted on an axle. A second disk on the same axle is comprised of an array of microlenses, arranged so each microlens is focused on one corresponding pinhole. A dichroic mirror is placed at an angle, typically 45°, between the microlens array and the pinhole array. The disks are arranged relative to an optical microscope such that the pinhole array is in an image plane of the microscope.

The axle containing the microlens and pinhole arrays is set to rotate at a high speed, typically 1,800 – 10,000 rpm. Collimated illumination impinges on the microlens array, passes through the dichroic mirror, and passes through the pinholes. The microscope then projects a demagnified image of the pinhole array onto the focal plane inside the sample. The focal spots excite fluorescence from the sample. The objective lens captures the fluorescence and the microscope re-images the fluorescence onto the pinhole array. Fluorescence emanating from the focal plane is brought to sharp focus on the pinholes and passes with high efficiency. Out of focus fluorescence is largely blocked by the pinholes.

The fluorescence then reflects off the dichroic mirror. A lens or set of lenses re-images the pinhole array onto a camera, often a CCD or EMCCD camera. The rotation rate of the pinhole array is sufficiently fast compared to the frame rate of the camera such that the camera registers a seemingly continuous image of the focal plane.

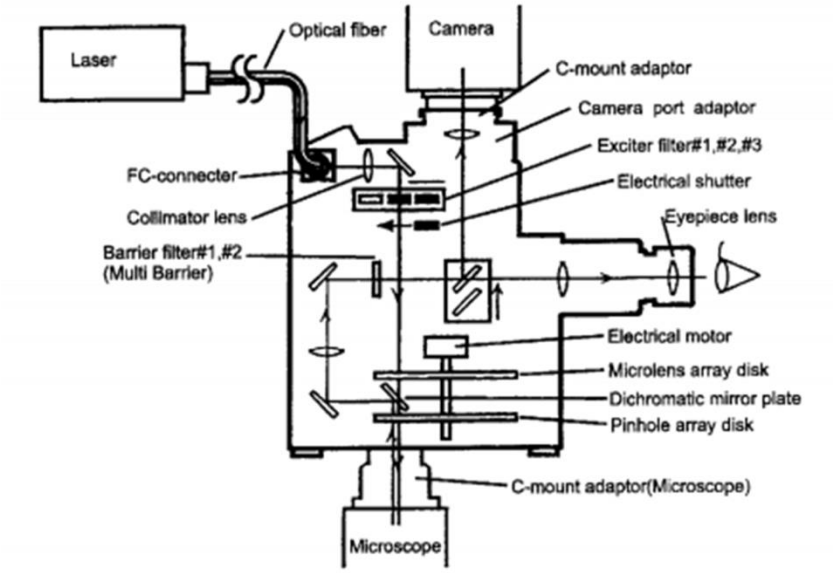

Figure 4-1: Optical path in Yokogawa spinning disk unit
Reproduced from [101].

This chapter discusses improvements made to a commercial spinning disk confocal microscope that enabled imaging of Arch *in vivo* as described in Chapter 2.

4.2 Modification of the input illumination

Traditionally, illumination light is coupled into the Yokogawa spinning disk unit via a single mode fiber (*top left*, Figure 4-1). The output of a single mode fiber is a beam with a Gaussian

intensity profile, which leads to uneven illumination of the sample. Not shown in Figure 4-1 is a series of internal optics that shape and expand the Gaussian beam after its entrance into the unit via the FC connector. A window aperture selects the center of this expanded beam, where illumination is the most intense and uniform, and rejects the rest of the incoming light.

For imaging dim samples, maximizing illumination power is essential for a high signal-to-noise ratio. Coupling into a single mode fiber is often inefficient, and rejecting excitation light to achieve a flat field is wasteful. About 1-2% of the light from our laser head made it onto the sample via this traditional input path.

Thus, we chose to remove the last turning mirror before the microlens array (*not shown*), and to externally shape our input beam before steering it directly onto the microlens array in the Yokogawa imaging system. This modification avoided the use of a lossy single mode fiber, and allowed complete control over the size and profile of our input illumination. We found that with these modifications, 10-20% of our input power could reach the sample, a 10-fold increase in comparison to the traditional coupling method.

4.3 Discovery of anomalous background fluorescence

In principle, spinning disk confocal microscopy enables highly sensitive and depth-resolved fluorescence imaging. However, we discovered that existing systems suffer from a background signal due to weak autofluorescence of the dichroic. This background interferes with imaging of very dim samples, such as single fluorescent molecules or very dim fluorophores.

We discovered this autofluorescence by noticing that even with the Yokogawa unit closed to the sample, illumination by 594 nm light into the unit resulted in faint fluorescence at the camera (Figure 4-2*a*) after an emission filter (655 nm, long-pass). The fluorescence was more pronounced

when the electron-multiplying gain of an Andor iXon camera was maximized (Figure 4-2*b*). Initially, we hypothesized that the fluorescence was spectral leakage of the illumination light through the emission filter. However, the addition of a second filter, 692/40 nm band-pass, only reduced the fluorescence by 30%, not the expected orders of magnitude (Figure 4-2*c*). This indicated that the wavelength of the aberrant fluorescence was indeed in the spectral band intended for our sample of interest.

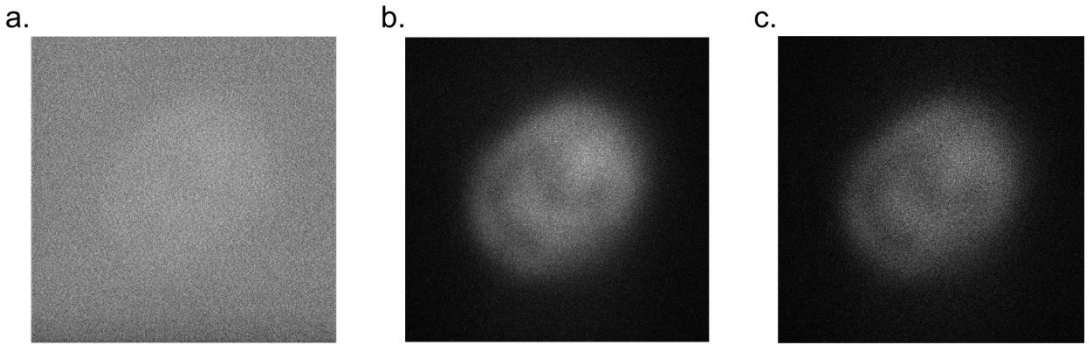

Figure 4-2: Autofluorescence from Yokogawa CSU-X1
(*a*) Fluorescence image at the sample with no electron-multiplying gain applied by the camera. Illumination at the sample was ~300 mW/cm^2 at 594 nm. The fluorescence passed through a 655 nm long-pass emission filter. (*b*) Fluorescence image at the sample with maximized electron-multiplying gain (300) applied by the camera. (*c*) A second emission filter (692/40 nm, band-pass) was placed in parallel with the 655 nm long-pass filter. Fluorescence only decreased ~30%.

Lastly, with the spinning disk not rotating (Figure 4-3*a*), we found that the fluorescence image looked like a partially in-focus image of the pinhole array (Figure 4-3*b*). In other words, the left side of the image was in focus and the right side of the image was not. We concluded that what we were seeing was autofluorescence coming from the dichroic itself. Beams of light from the microlens array come to a focus at the pinhole array. Because the dichroic sits at a 45^o angle between the microlens array and the pinhole array, on one side, the dichroic is very close to the pinhole array. Here, beams from the microlens array are nearly in focus and only illuminate

focused spots on the dichroic. At the other extreme, where the dichroic is close to the microlens array, the light from the microlens is still diffuse, and thus fluoresces large areas of the dichroic.

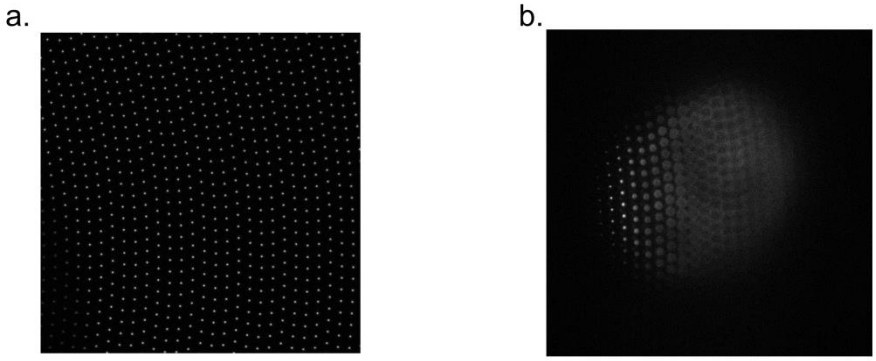

Figure 4-3: Images of autofluorescence from a stopped disk of the Yokogawa unit
(*a*) Trans-illuminated image of the stopped pinhole array inside of a Yokogawa spinning disk unit. (*b*) Image of dichroic autofluorescence with a stopped pinhole array.

The autofluorescence of the dichroic is a more severe problem in spinning disk confocal microscopy than in conventional epifluorescence microscopy for two reasons. First, in epifluorescence systems, the intense excitation light reflects off the front surface of the dichroic (*blue arrow*, Figure 4-4*a*), while in spinning disk systems, the excitation light passes through the dichroic (*blue arrow*, Figure 4-4*b*). Thus the excitation light in spinning disk systems interacts with a far larger volume of the dichroic (the entire thickness) than in epifluorescence (just the front surface). The excitation light therefore excites more fluorescence from the substrate of the dichroic in spinning disk systems.

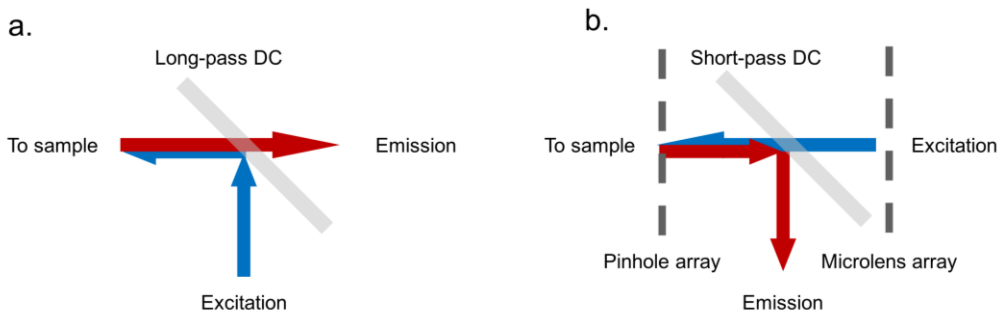

Figure 4-4: Comparison of optical setup between conventional epifluorescence microscopy and spinning disk confocal microscopy
(*a*) Excitation light (*blue*) reflects off a long-pass dichroic (DC), and red-shifted emission light (*red*) is transmitted through the DC to the detector. (*b*) In contrast, in spinning disk confocal microscopy, excitation light (*blue*) is transmitted through a short-pass DC, and red-shifted emission light (*red*) reflects off the DC to the detector.

Secondly, in epifluorescence systems, the dichroic mirror is far from an image plane. Only a small fraction of light emitted from the dichroic is collected by the microscope optics and re-imaged onto the detector. In spinning disk systems, the dichroic is positioned close to an image plane. The optics that re-image the pinholes onto the camera also collect a large fraction of the autofluorescence from the dichroic.

4.4 Modifications for improved an signal-to-noise ratio

To overcome this autofluorescence issue, we invented a simple optical element which improved the signal-to-background ratio 37-fold. Figure 4-5 illustrates the invention. Traditionally the camera would reside at P1, the first image plane just outside the spinning disk unit. The numerical aperture of the desired signal at P1 is given by NA/M, where NA is the numerical aperture of the objective and M is the magnification. In contrast, the numerical aperture of the autofluorescence at P1 is D0/(2*f0), where D0 is the diameter and f0 is the focal length of the last lens inside the spinning disk unit (*not shown*.)

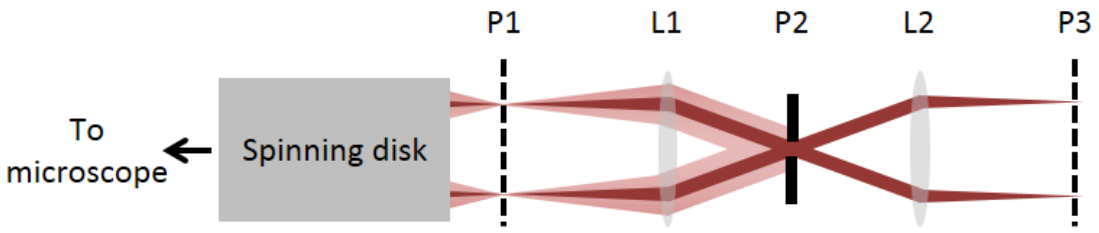

Figure 4-5: Yokogawa unit with spatial filter on emission port
A series of two lenses L1 and L2 at the output of the Yokogawa unit reimages the sample onto the camera. An iris in the Fourier plane of the image rejects most of the background autofluorescence (*pink*) while transmitting the fluorescence signal (*dark red*) from the focal plane of interest in the sample.

A lens L1 with focal length f1 is focused on P1, collimating the rays emerging from each pinhole into a bundle of diameter D1 = 2 f1*NA/M. At plane P2, a distance f1 away from L1, these bundles of rays cross. A pinhole of diameter D1 passes the light from the pinholes. In contrast, the autofluorescence of the dichroic is not confined at plane P2 and is mostly blocked by the pinhole.

A lens L2 is focused on P3 and forms an image at P3, where a camera is placed. To obtain maximum rejection of background, lenses L1 and L2 should have focal lengths as short as practical.

The spatial filter described here can be applied to reject background autofluorescence from sources other than the dichroic. For instance, in fluorescence microscopy with ultraviolet excitation, there is often significant autofluorescence from the objective itself. The present invention may be used to reject this background, either in the context of spinning disk confocal microscopy, or in the context of conventional epifluorescence microscopy.

4.5 Applications to biological samples

Figure 4-6 compares a confocal image of HEK cells expressing Arch, with and without the spatial filter. The autofluorescence of the dichroic is obvious in Figure 4-6*a*, where there is no spatial filter. In contrast, in Figure 4-6*b*, the image exhibits minimal background fluorescence with the addition of the spatial filter.

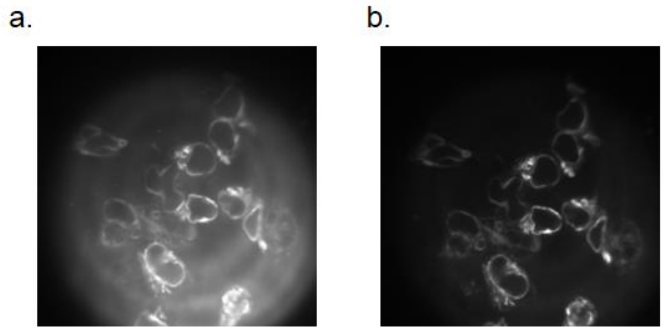

Figure 4-6: Comparison of spinning disk confocal images with and without the spatial filter
Fluorescent images (λ_{ex} = 594 nm, λ_{em} > 655 nm) of HEK cells expressing Arch with the modified spinning disk confocal microscopy (*a*) without the spatial filter and (*b*) with the spatial filter. Background is significantly reduced upon addition of a spatial filter.

We tested if we could detect single molecules in the spinning disk, which in past, has not been possible. We made a dilute solution of hyaluronidase labeled with Alexa Fluor 488, and confined it to a thin flow cell. We were able to image the individual enzyme molecules as they diffused into the focal plane of the spinning disk. The change in intensity counts (~900) when a bright spot came into view was relatively constant (Figure 4-7). Occasionally, intensity changes were twice as large (teal trace in Figure 4-7), indicating a doubly-labeled hyaluronidase molecule. The quantization of the fluorescence changes led us to infer that we were seeing single molecules of hyaluronidase.

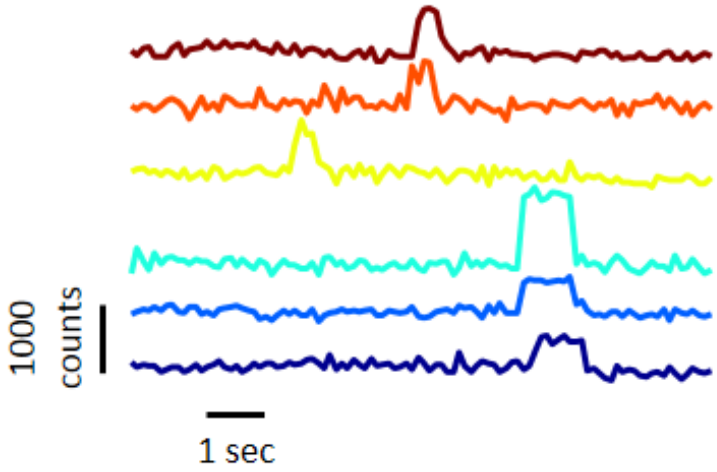

Figure 4-7: Fluorescent traces of hyaluronidase-AF488 entering and exiting the image plane of the modified spinning disk microscope

We showed that the Yokogawa spinning disk has an inherent design flaw that has prohibited its broad use in laboratories working with dim samples. The changes we made to the Yokogawa spinning disk, while simple, drastically reduced the background autofluorescence caused by the dichroic. Such a modification increases the possibility of imaging dim samples in a three-dimensional volume.

Chapter 5 Motion induced by asymmetric enzymatic degradation of hydrogels

5.1 Introduction

Polymer-based hydrogels are ubiquitous in life – from mucus that lines most internal epithelia of the human body [102], to the extracellular matrix (ECM) that fills the space between cells [103], to the extracellular polymeric substance (EPS) secreted by biofilm-forming bacteria [104]. In each case, transport through the hydrogel is critical to the survival of the organism(s). Mucus, in addition to serving as a lubricant, blocks pathogens while passing nutrients, oxygen, or sperm, depending on the organ [102, 105, 106]. The ECM provides structural support to tissues and organs [107, 108], but also regulates cell-to-cell communication by mechanical and chemical signals [109, 110]. Additionally, the ECM serves as a highway for cellular movement, such as keratinocyte migration during wound healing [111] and tumor cell invasion during metastasis [112, 113]. EPS anchors bacteria to a favorable surface [103, 104], but also modulates nutrient flow within the bacterial biofilm [114].

Transport of molecules and cells is sensitive to the physical and chemical properties of the hydrogel environment, which, in turn, are often sensitive to external parameters such as humidity, temperature, pH, and ionic strength. Some cells regulate transport by varying these physical parameters. For example, *Helicobacter pylori*, a bacterium known for its unique ability to colonize the stomach lining and create ulcers, secretes the enzyme urease which raises the pH and thereby lowers the viscosity of gastric mucus [115]. The decrease in viscosity is believed to facilitate colonization by the bacterium.

Many cells, especially pathogens, secrete or decorate their surface with gel-degrading enzymes: pathogenic *E. coli* [116] and *Vibrio cholera* [117, 118] secrete proteases; influenza decorates its coat with neuraminidase, a glycosidase [119, 120]; and metastatic tumors secrete matrix metalloproteases [112, 113]. Enzymatic degradation can lead to steep spatial gradients in gel properties, as the enzyme irreversibly cleaves strands of the gel. In turn, spatially heterogeneous changes of the gel parameters can lead to nonequilibrium motion of particles embedded the gel, i.e. the appearance of active transport. Thus, it is important to study how gradients in gel degradation affect the motion of small particles through the gel to begin to understand relevant biological phenomena.

We studied motion of beads embedded in gelatin, in a gradient of trypsin concentration. Trypsin is a serine protease that readily degrades gelatin and is found in the digestive tracts of many vertebrates. We discovered that as the enzyme digested the gel, the beads moved up the enzyme concentration gradient, in the direction of greater gel degradation. We sought a physical model that would explain the existence and direction of this motion, the time of initial bead motion, and the velocity with which the beads first moved. To constrain the model, we simultaneously tracked the motion of the enzyme, the gel, and the beads. We found that enzymatic degradation caused the gel to swell in the direction of maximal degradation. The swelling gel carried the beads with it. This finding suggests that degradation-induced swelling is a possible transport mechanism in nonequilibrium biogels.

5.2 Directed motion of beads in a gradient of enzymatic degradation

We developed a split channel flow cell assay to generate a gradient in trypsin concentration inside a sample of bead-laden gelatin (Figure 5-1*a*). The gelatin was labeled with a blue

fluorophore, Alexa 488 (AF488), and the enzyme was labeled with a red fluorophore, Alexa 647 (AF647), while the beads were visible via bright-field microscopy. We used multi-wavelength time-lapse imaging to follow the motion of all three components simultaneously.

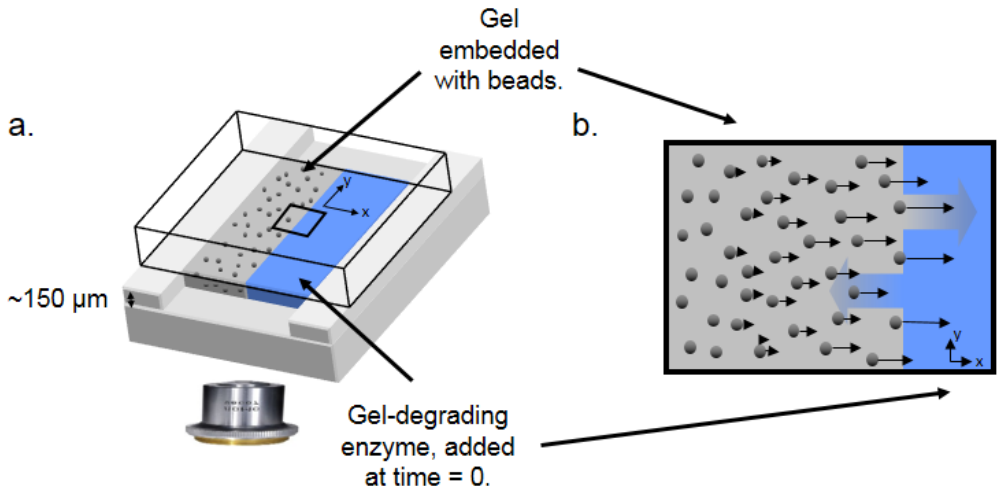

Figure 5-1: Experimental setup with split channel flow cell
(*a*) Flow cell made with glass. Half of the flow cell was filled with bead-laden gel. At time = 0, the other half was filled with a gel-degrading enzyme. (*b*) Microscopic depiction of boxed area in (*a*).

At the start of each experiment, a solution of trypsin in pre-digested gelatin was introduced along one edge of the gelatin. The trypsin diffused into the gelatin, and established an enzyme concentration gradient. This enzyme gradient led to a degradation gradient in the gelatin. The microscopic beads embedded in the gelatin spontaneously moved up the enzyme gradient. Digested gelatin also drifted up the enzyme gradient. Control solutions of buffer with no enzyme, or with heat-inactivated enzyme, did not induce bead motion.

Figure 5-2 shows typical data in which beads, gel, and enzyme were tracked simultaneously. The motion of all three components was predominantly along the *x*-coordinate (perpendicular to the gel-enzyme interface), and independent of *y*-coordinate (parallel to the gel-

enzyme interface). Thus bead motion, enzyme concentration, and gel concentration were averaged over *y* and analyzed as functions of *x* and *t*.

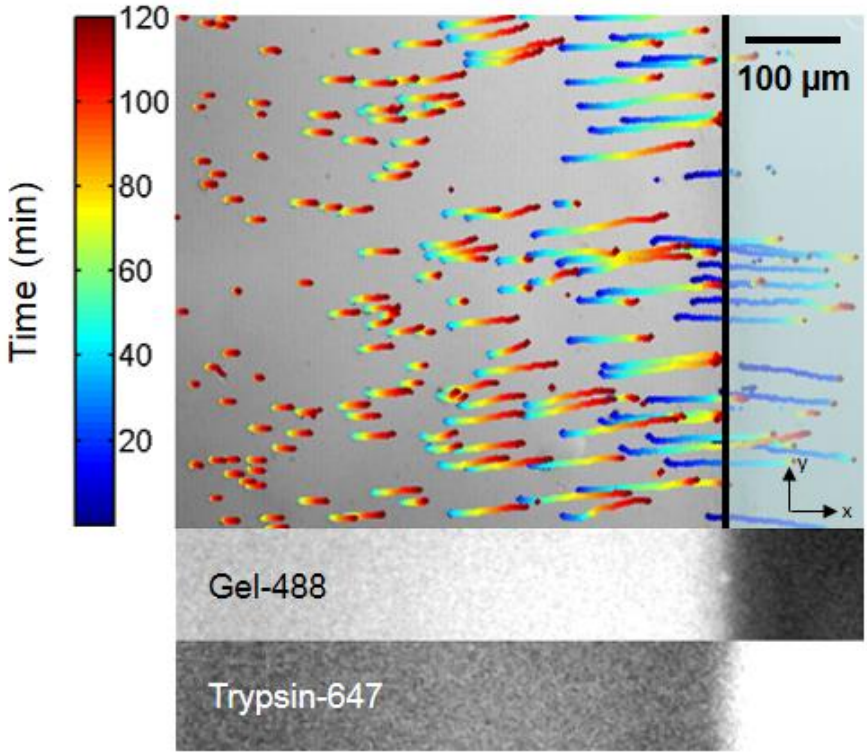

Figure 5-2: Particle motion driven by gel swelling under a gradient of enzyme degradation
Time-colored trajectories of beads in a gel degradation gradient overlaid on a brightfield image (*top*), with simultaneous fluorescence imaging of gelatin-488 (*middle*) and trypsin-647 (*bottom*). The black vertical line marks the gel-enzyme interface. The sample is 6 µm polystyrene beads embedded in 5% (*w*/*w*) gelatin (*left of the interface*) with 1 mg/mL trypsin in 5% digested gelatin (*right of the interface*). The images were acquired at 12 frames per minute. The enzyme diffused into the gel matrix and degraded the gel. The enzymatic degradation of the gel induced directional motion of both the gel molecules as well as the embedded beads. Beads closer to the interface moved earlier than beads farther from the interface.

The beads underwent three phases of behavior. Initially, the beads were at rest in the gel. As the enzyme permeated and digested the gel, the beads moved toward the interface. Trajectories of beads, averaged over initial position away from the interface, are plotted as a function of time

and space (Figure 5-3*a*). Beads closest to the interface moved earliest and fastest, while beads further from the interface moved later and slower. At 5% gelatin, and 1 mg/mL trypsin, early-moving beads had initial velocities of ~0.2 μm/s while late-moving beads had initial velocities asymptotically approaching 0.03 μm/s at x = -1 mm from the initial interface (Figure 5-3*b*). Finally, the beads slowed and drifted up the enzyme gradient at ~0.02 μm/s and began to show detectable Brownian motion, indicating a transition of the gelatin from a gel to a liquid. We call the (x, t)-coordinate at initial bead motion the 'invasion front,' indicated by the grey dotted line in Figure 5-3*a*. The initial bead velocity at the time of motion is plotted vs. starting x-position in Figure 5-3*b*.

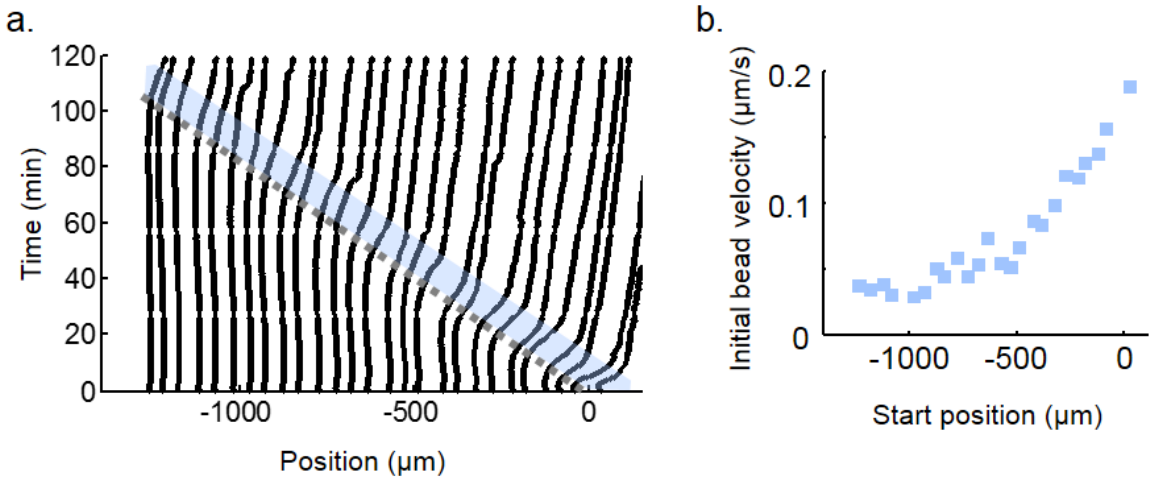

Figure 5-3: Bead trajectories an enzymatic degradation gradient
(*a*) Trajectories of beads as a function of position from interface and time for 5% gelatin and 1 mg/mL trypsin. Trajectories were acquired from time-lapse images of beads at 12 frames per minute. Net bead motion was toward the gel-enzyme interface, located at x = 0. The grey dotted line indicates the 'invasion front', the (x,t)-coordinate at which beads started to move. (*b*) Initial bead velocities (blue region on (*a*)) as a function of starting position for the same data set (5% gelatin and 1 mg/mL trypsin). Brownian motion of the beads became detectable ~10 minutes after initial bead movement, coincident with a decrease in bead velocity.

5.3 Motion of beads in homogeneous enzymatic degradation

The experiments in Section 5.2 generated gradients in enzyme concentration due to enzyme diffusion, gradients in gel structure due to heterogeneous degradation, and gradients in hydrostatic pressure due to osmotic swelling of the degraded gel. To determine which gradients were responsible for bead motion, we studied motion of beads in gelatin with spatially homogeneous enzyme concentration, and hence homogeneous gel degradation.

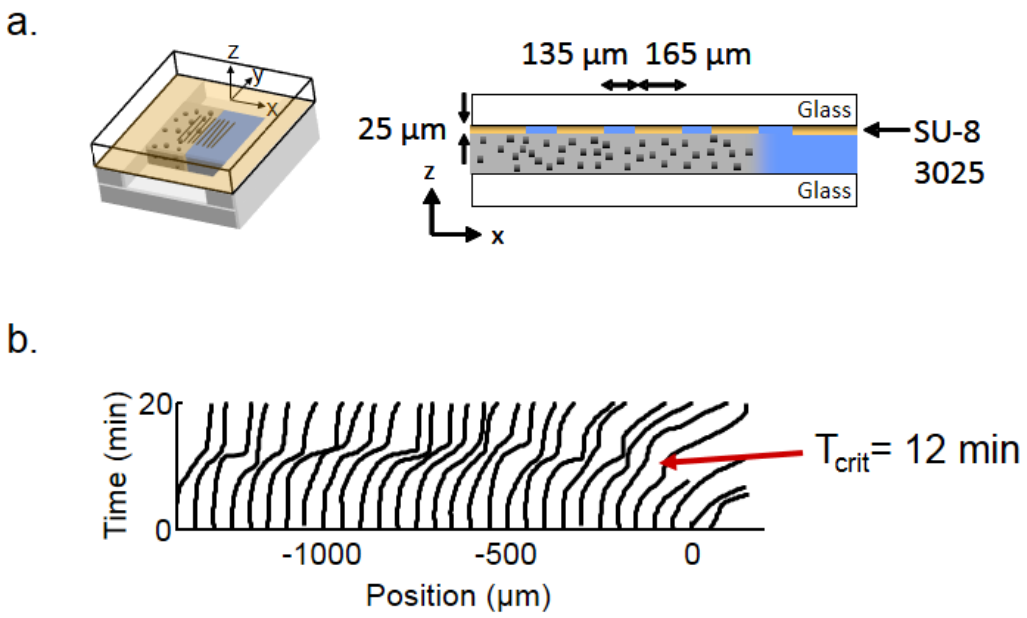

Figure 5-4: Particle motion driven by gel swelling under homogeneous enzyme degradation
(*a*) Experimental setup with split channel flow cell. A micropatterned lid provided vertical confinement while allowing enzyme to permeate the gel homogeneously from the top. The enzyme (*blue*) quickly diffused vertically into the gelatin, leading to spatially homogeneous degradation. (*b*) Trajectories of beads as a function of position and time for 5% gelatin and 0.1 mg/mL trypsin, acquired at 12 frames per minute. At T_{crit} = 12 minutes, the beads synchronously moved toward the free interface.

We designed a microfluidic chamber to deliver enzyme rapidly throughout the gel at the start of the experiment. The lid of the split channel flow cell used in Section 5.2 was replaced with a slide containing microfabricated grooves (

Figure **5-4***a*). These grooves enabled rapid introduction of enzyme over the entire top surface of the gel. Diffusion of enzyme from the grooves into the gel took ~2 min, shorter than any other timescales in the experiment.

Initially most beads remained stationary. At t = 12 minutes beads throughout the sample moved in the $+x$-direction at a velocity of ~0.3 μm/s. This motion lasted for ~5 min, and then slowed. Thereafter we observed Brownian motion of the beads, indicating a transition from a gel to a liquid.

These observations of bead motion in the absence of gradients in enzyme concentration or gel degradation establish that diffusiophoresis is not necessary for degradation-induced motion. Furthermore, the absence of detectable Brownian motion during the directed motion indicates that the beads remained strongly coupled to the viscoelastic gel network. Thus we infer that the motion of the beads was due to degradation-induced swelling of the gel toward the free solution-gel interface.

Under physiological conditions, one rarely has a homogeneous distribution of enzyme that is suddenly activated; typically enzyme is produced from a source and diffuses into the gel. Additionally, in the homogeneous degradation experiments, the asymmetric boundary conditions (free on one side, fixed on the other) set the direction of motion. In an enzymatic gradient however, it is the gradient that establishes the asymmetry leading to directed motion. Thus we next sought to determine how enzymatic diffusion and reaction kinetics interacted with gel swelling to produce the motions observed in Section 5.2.

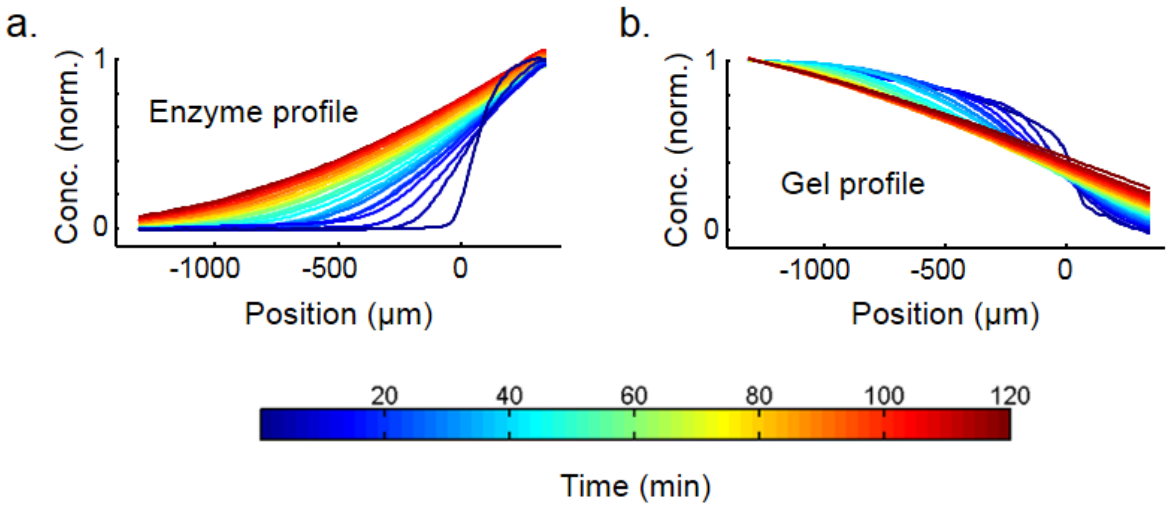

Figure 5-5: Fluorescent profiles as a function of time and position along enzyme gradient
(*a*) Enzyme and (*b*) gel profiles as a function of position from the interface (*x*) and time (*color*).

We divided the observed process into three stages: 1) enzyme transport through the gel; 2) enzymatic cleavage of the gel strands; and 3) swelling of the gel to a new hydrostatic quasi-equilibrium and corresponding motion of the beads. To disentangle the roles of each process on the observed bead motion, we simultaneously tracked the diffusion of the enzyme and the motion of the gel in gradient experiments under different conditions, and also conducted additional experiments to explore the kinetics of the gel-enzyme reaction in a homogeneous solution.

5.4 Diffusive transport of enzyme through gel

We first analyzed the transport of the enzyme through the gel. The theory of diffusion in gels has been treated previously [121]. If the transport of the enzyme is purely diffusive and our sample is translationally invariant in *y*, then the concentration profile of enzyme, $c(x, t)$ is governed by the 1D diffusion equation:

$$\frac{\partial c(x,t)}{\partial t} = D\frac{\partial^2 c(x,t)}{\partial x^2} \tag{5-1}$$

where D is the diffusion coefficient of enzyme through the gel. If the gel resides in a semi-infinite plane $x \geq 0$, the solution to Equation (5-1) with the initial condition $c(x,0) = c_0\theta(-x)$ yields the following functional form for the dimensionless mean position of the enzyme, $\langle \tilde{x}_{\text{enz}}(t) \rangle$, over a region $x \in [0, x_{\text{f}}]$:

$$\langle \tilde{x}_{\text{enz}}(t) \rangle = \frac{Dt * \text{erf}\left(\frac{x_{\text{f}}}{2\sqrt{Dt}}\right) + \frac{1}{2}x_{\text{f}}\left(-2\sqrt{\frac{Dt}{\pi}}\exp\left(-\frac{{x_{\text{f}}}^2}{4Dt}\right) + x_{\text{f}}\ \text{erfc}\left(\frac{x_{\text{f}}}{2\sqrt{Dt}}\right)\right)}{2x_{\text{f}}\sqrt{\frac{Dt}{\pi}}\left(1-\exp\left(-\frac{{x_{\text{f}}}^2}{4Dt}\right)\right) + x_{\text{f}}\ \text{erfc}\left(\frac{x_{\text{f}}}{2\sqrt{Dt}}\right)} \tag{5-2}$$

where $\text{erf}(x) = \frac{2}{\sqrt{\pi}}\int_0^x e^{-t^2}dt$ and $\text{erfc}(x) = 1 - \text{erf}(x)$.

A typical profile of enzyme concentration as a function of time is shown in Figure 5-5*a*. To further reduce the dimensionality of the data, we converted each time-dependent concentration profile $\varepsilon(x,t)$ into a dimensionless mean enzyme position $\langle \tilde{x}_{\text{enz}}(t) \rangle$, calculated from:

$$\langle \tilde{x}_{\text{enz}}(t) \rangle = \frac{\int_0^{x_{\text{f}}} x\varepsilon(x,t)\text{d}x}{x_{\text{f}}\int_0^{x_{\text{f}}} \varepsilon(x,t)\text{d}x} \tag{5-3}$$

where x_{f} is the edge of the gel opposite the initial gelatin-trypsin interface (x = 0). Figure 5-6*a* shows $\langle \tilde{x}_{\text{enz}}(t) \rangle$ for three gelatin concentrations, all at a trypsin enzyme concentration of 1 mg/mL (points). The data are well fit by a simple Fickian diffusion model (*solid lines*, Equation (5-2), with trypsin diffusion coefficients of D_{tryp} = 42.2, 44.0, and 29.4 μm^2/s in gelatin concentrations 2.5%, 5%, and 10%, respectively. The weak dependence of D_{tryp} on gelatin concentration is

consistent with free diffusion of the enzyme through the interstices of the gel, with the enzyme spending little of its time bound to the gel.

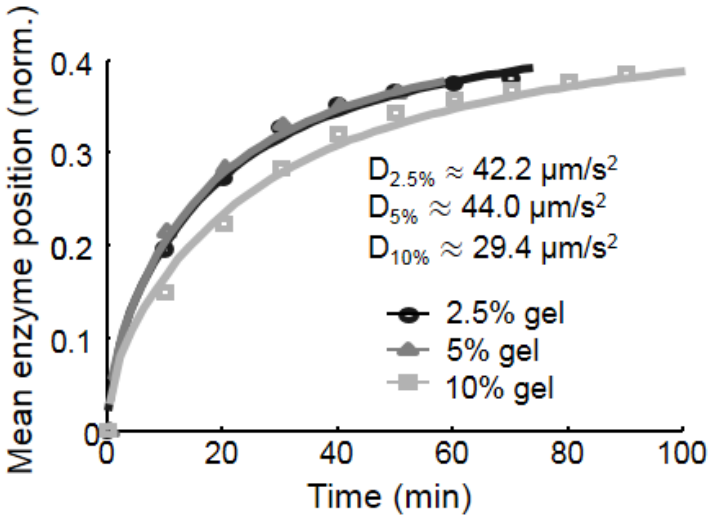

Figure 5-6: Characterization of enzyme transport through the degrading gel
The mean penetration of enzyme into the gel as a function of time for three gelatin concentrations. The solid lines are fits to the analytic solution given by Equation (5-2). Diffusion of the enzyme was only weakly dependent on gelatin concentration.

To confirm our hypothesis that trypsin diffused almost freely, we compared the diffusion of trypsin in gelatin to the diffusion of free Alexa 647 dye in undegraded gelatin. The dye had larger absolute diffusion coefficients than trypsin, as expected from its smaller molecular size, but showed a similar dependence of D_{dye} on gel concentration. The dye had D_{dye} = 198 μm^2/s in 5% gel and D_{dye} = 121 μm^2/s in 10% gel, a 39% decrease, while D_{tryp} decreased by 33% between 5% and 10% gel.

The insensitivity of enzyme diffusion to gel concentration and similarity to free dye diffusion allowed us to rule out significant sticking of the enzyme to the gelatin, significant

degradation-dependent modifications in D_{tryp}, and significant changes to enzyme motion due to convection of the buffer or directional motion of the gel.

5.5 Critical enzyme exposure for bead motion

The onset of bead motion in the homogeneous degradation experiments (Section 5.3) was largely independent of *x*-position. In contrast, in the gradient experiments (Section 5.2), the invasion front propagated through the gel at nearly constant velocity. We defined the invasion velocity as the inverse slope of the grey dotted line in Figure 5-3*a*. This velocity increased with enzyme concentration and decreased with gelatin concentration (*dark grey bars*, Figure 5-7*a* and *b*). However, the initial bead velocities, averaged over *x*, were roughly independent of enzyme concentration, and non-monotonic with gelatin concentration, being higher at 5% gel than at 2.5% or 10% (*light grey bars*, Figure 5-7*a* and *b*).

We sought a model of the gel degradation process to explain the sudden onset of bead motion (Figure 5-3*a* and

Figure **5-4***b*), and the dependence of the invasion velocity on enzyme concentration and gel concentration (Figure 5-7*a* and *b*). Together, these trends suggested that the concentration of gelatin crosslinks, $C(x, t)$, had to pass below a threshold C_{crit} for bead motion to commence.

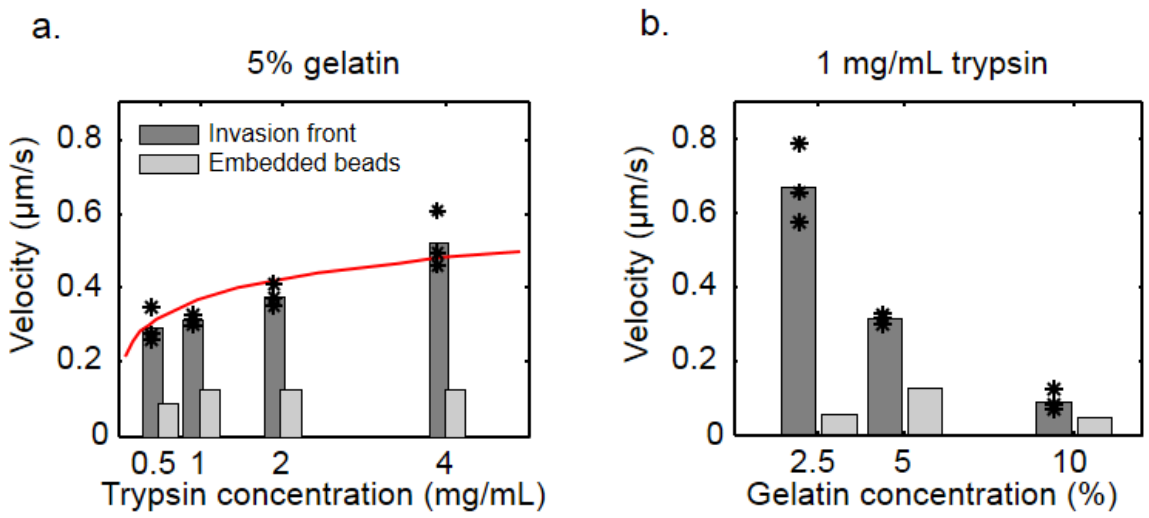

Figure 5-7: Characterization of transport as a function of initial enzyme and gel concentrations
Velocities of invasion front (*dark grey bars*) and beads (*light grey bars*) as a function of (*a*) trypsin concentration at 5% gelatin concentration; and (*a*) gelatin concentration at 1 mg/mL trypsin concentration. Invasion front bars represent the average of three data sets, whose individual values are indicated by the asterisks. Bead velocity bars represent the mean initial velocities across the three data sets. The red line on (*c*) is a scaled fit to our model for invasion velocity as a function of enzyme concentration.

The enzyme acts as a monomer and the number of enzyme binding sites in the gelatin vastly exceeds the number of enzyme molecules; thus one expects the reaction to be first order in enzyme:

$$\frac{\partial C}{\partial t} \propto \varepsilon \qquad (5\text{-}4)$$

where $C(x, t)$ is the concentration of gel crosslinks and $\varepsilon(x,t)$ is the time-dependent enzyme concentration. This model implies that $C(x, t)$ depends on $\varepsilon(x,t)$ only through the cumulative enzyme exposure, $\mathrm{E}(x,t) = \int_o^t \varepsilon(x,t')\,\mathrm{d}t'$, regardless of the order of the reaction in C. Thus for each initial enzyme concentration C_0, the critical crosslink concentration for bead motion C_{crit} should correspond to a critical cumulative enzyme exposure, E_{crit}.

The T_{crit} for bead motion in homogeneous degradation conditions corresponds to E_{crit} = 1.2 (min·mg/mL) (

Figure **5-4***b*). Similarly, we calculated E(x, t) from the measured $\varepsilon(x,t)$ of Figure 5-5*a* in gradient degradation conditions for a 5% gel and 1 mg/mL enzyme source (Figure 5-8). Throughout the gel, bead motion commenced at a characteristic cumulative enzyme exposure E_{crit} = 1.6 (min·mg/mL) (*inset*, Figure 5-8). The similarities in E_{crit} between the two experiments, and throughout a heterogeneously degraded gel, support the model of a critical crosslink concentration for bead motion.

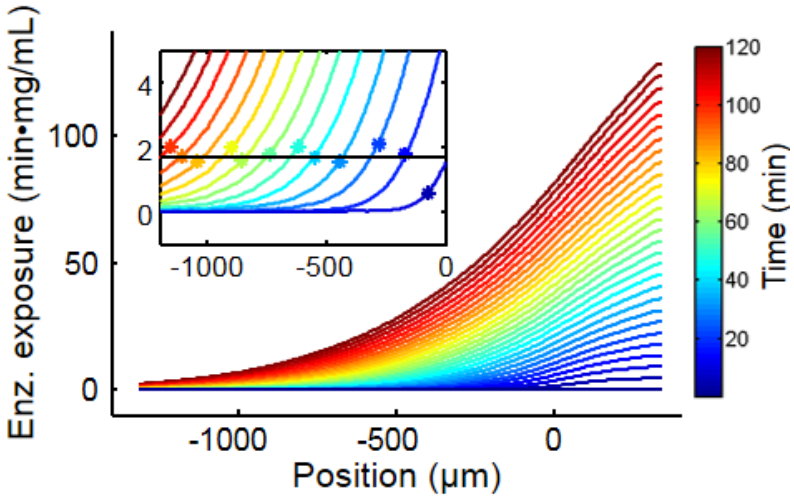

Figure 5-8: Cumulative enzyme exposure as a function of position and time
Gel was 5% (w/w), and enzyme was at 1 mg/mL. (*Inset*) Zoom-in at low cumulative exposure values. Asterisks indicate the (*x*,*t*)-coordinate of the invasion front from Figure 5-3*a*. The enzyme exposure at these position-time points was constant at 1.6 min•mg/mL (*black*).

We combined our finding that enzyme transport was diffusive (Section 5.4) with the observation that bead motion commenced at a critical cumulative enzyme exposure, to predict the

invasion front velocity as a function of initial enzyme concentration. Our simple model captured the dependence of velocity on enzyme concentration observed in our data (*red line*, Figure 5-7*a*).

We further hypothesized that the gel-enzyme reaction was first order in *C*, i.e.

$$\frac{\partial C}{\partial t} = -k\varepsilon C \,. \tag{5-5}$$

Then

$$C(x,t) = C_0 \exp\left(-k\int_0^t \varepsilon(x,t')dt'\right) = C_0 \exp\left(-k\mathrm{E}(x,t)\right). \tag{5-6}$$

We used Equation (5-6) to predict the motion of the invasion front at several initial gel concentrations. The rate constant *k* was varied to fit our predictions to the data of Figure 5-7*b*, yielding $k = 0.47$ (min·mg/mL)$^{-1}$ at 20 ºC.

5.6 Molecular state of gel upon bead motion

We sought to characterize the state of the gel at the onset of bead motion. We quantified the extent of Brownian motion perpendicular to the drift velocity before, during, and after motion. Before and during bead motion, there were no detectable position fluctuations. After directed motion had slowed, we observed Brownian motion with a diffusion coefficient of $D = 0.05$ μm^2/s, consistent with a low viscosity liquid. To estimate the magnitude of thermal fluctuations, we calculated the effective spring constant *k* for displacement of a 6 μm diameter bead in an infinite gel with Young's modulus 40 kPa and Poisson's ratio 0.4, corresponding to the mechanical properties of a 5% gelatin gel. From the relation $\left\langle \delta x^2 \right\rangle = k_B T / k$ we obtained an amplitude < 1 nm, consistent with the absence of detectable thermal fluctuations prior to gel liquefaction.

The bead migration data did not indicate the molecular state of the gelatin at the onset of bead motion. To obtain a more detailed understanding of the process by which trypsin degrades

gelatin, we investigated the reaction in bulk solution, where enzyme and gel concentrations were homogeneous in space. We used sodium dodecyl sulfate polyacrylamide gel electrophoresis (SDS-PAGE) to analyze the distribution of gelatin molecular weights as a function of incubation time with enzyme. The degradation products were stained with Coomassie blue (Figure 5-9).

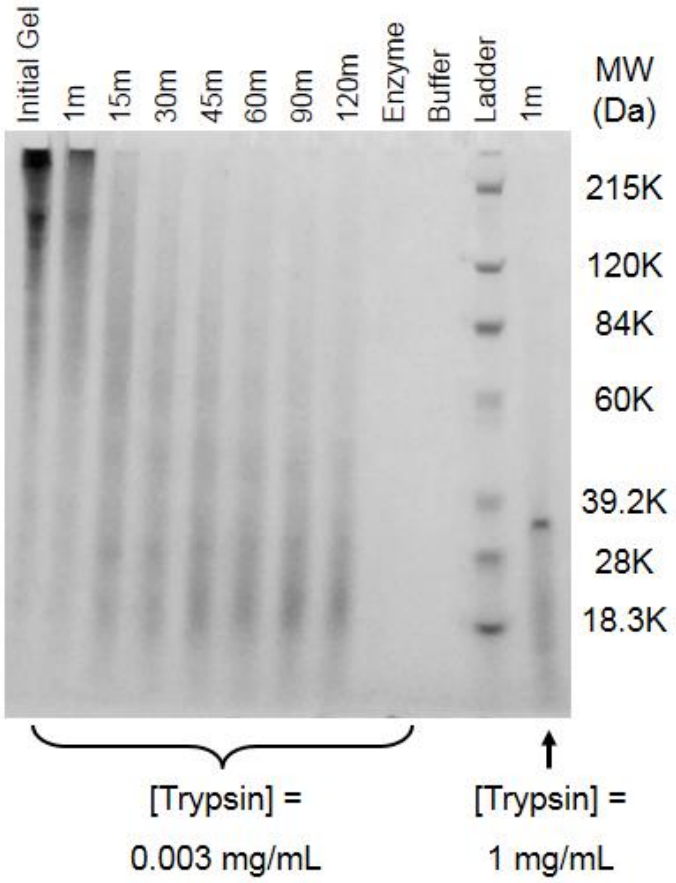

Figure 5-9: SDS-PAGE gel of gelatin after digestion for fixed time
Enzyme concentrations were 0.003 mg/mL (*lanes 2-9*) and 1 mg/mL (*lanes 12-15*). Gel was stained with Coomassie blue.

At a trypsin concentration of 1 mg/mL—corresponding to the loading concentration in the bead experiments—the gelatin was degraded into segments smaller than our lower bound of detection (~15 kDa) within one minute of mixing (lane 12 of gel, Figure 5-9). At 300-fold lower trypsin concentration (0.003 mg/mL), we observed that in a span two hours, there was a gradual disappearance of large molecular weight gelatin and appearance of smaller molecular weight

fragments. The staining pattern within each lane was converted to a distribution $\rho(l,t)$ describing the concentration of molecules with molecular weight l at time t (Figure 5-10*a*).

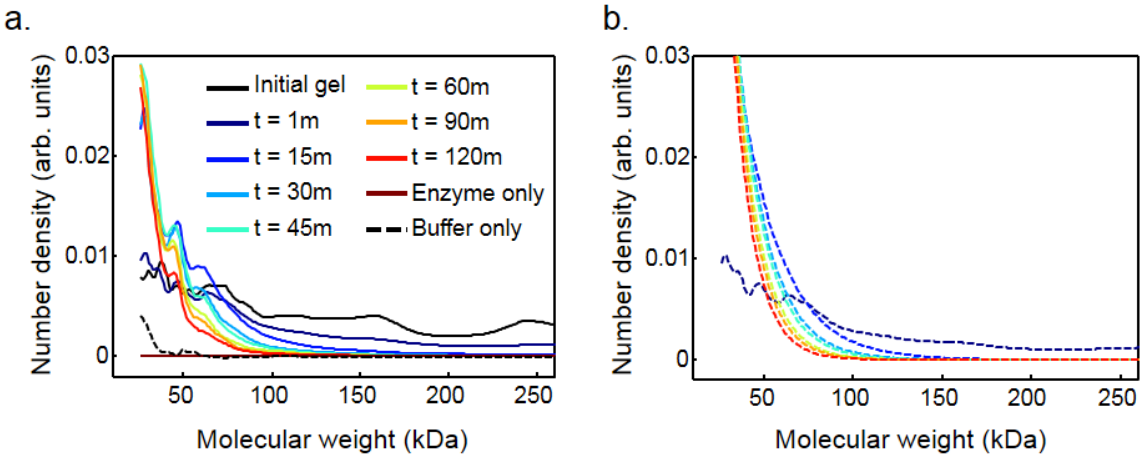

Figure 5-10: Molecular weight distribution of the gelatin during degradation
(*a*) Gelatin distribution by molecular weight, extracted from SDS-PAGE gel (Figure 5-9, lanes 2-9) with trypsin concentration of 0.003 mg/mL. Molecular weight components >100 kDa of the gelatin disappeared within the first minutes of the reaction, and their smaller molecular weight products accumulated over time. (*b*) Evolution of the molecular weight distribution by a random scission binary fragmentation model, with initial conditions determined by the experimental molecular weight distribution of undegraded gelatin. The model could be matched to data shown in (*a*) by assuming a time-dependent rate constant.

We constructed a microscopic model of gel degradation to explain the measured molecular weight distributions. Trypsin cleaves gelatin at arginine and lysine residues, but only if the residue is not followed by proline [122]. From the amino acid composition of gelatin [123], we estimated the density of cleavage sites $\alpha \sim 1$ per kDa of gelatin. As a result of the processing from collagen, the molecular weights of gelatin are heterogeneous, ranging from 100-400 kDa. It was thus reasonable to assume that the number of cleavage sites n was proportional to the molecular weight l, so we worked with the distribution $\rho(n,t)$.

Each cleavage event converted a strand with *n'* cleavage sites into two strands with *n* and *n' – n – 1* sites (one site was lost to cleavage). We assumed that after each cleavage event, the enzyme dissociated from the polymer and that there was no correlation between the locations of successive cleavage events. Finally, we assumed that the enzyme had no molecular weight preference, i.e. that all cleavage sites were equally good targets, regardless of the length of the chain in which they were embedded. Under these admittedly simplifying assumptions, the evolution of $\rho(n,t)$ is governed by a simple master equation, originally developed in the context of thermal degradation of polymers [124, 125]:

$$\frac{\partial \rho(n,t)}{\partial t} = -\gamma n \rho(n,t) + 2\gamma \sum_{n'=n+1}^{n'=n_{\max}} n' \Omega(n,n') \rho(n',t) \tag{5-7}$$

where γ is the rate of scission *per cleavage site* on the polymer backbone. The second term on the right hand side describes the creation of a strand with *n* sites from one with *n*' > *n* sites. The assumption of uniformly distributed random scission implies that

$$\Omega(n,n') = \frac{1}{n'} \text{ for } n < n' . \tag{5-8}$$

Using Equation (5-8) we recast Equation (5-7) in matrix form:

$$\frac{d\vec{\rho}(t)}{dt} = \gamma \mathbf{T} \vec{\rho}(t) , \tag{5-9}$$

where $\vec{\rho}(t) = \rho(n,t)$ and the matrix **T** is

$$\mathrm{T}_{n,n'} = \begin{cases} 2 & \text{for } n < n' \\ -n & \text{for } n = n' \\ 0 & \text{otherwise} \end{cases} . \tag{5-10}$$

We fit Equation (5-9) to the data in Figure 5-10*a* at t = 15, 30, 45, 60, 90, 120 min, using $\vec{\rho}(t = 1\text{min})$ as the initial condition and floating the rate constant γ (Figure 5-10*b*). The good correspondence between the predicted molecular weight distributions (Figure 5-10*b*) and the

measured distributions (Figure 5-10*a*) indicates that the simple binary fragmentation model accurately captures the mechanics of the trypsin-gelatin degradation reaction.

The SDS-PAGE data enabled us to determine the degree of gelatin degradation at which beads started to move in the gradient studies. We extrapolated the data in Figure 5-10*a* to the critical cumulative enzyme exposure calculated for the gradient experiments (Section 5.5). Bead motion commenced when the gelatin had ~0.13 cuts/kDa and only 1% of the remaining gelatin was larger than 45 kDa. This high degree of degradation prior to bead motion is explained by the fact that the gelatin molecules assemble into higher-order fibrils [126, 127]. Cleavage of a single gelatin molecule does not change the crosslink density—only when enzyme has completely cut through a fibril does the crosslink density change.

We compared the cleavage rate γ inferred from bulk degradation with the cleavage rate constant k inferred from the velocity of the invasion front (Section 5.5). These rates are related by

$$k = \frac{\gamma\alpha}{[\text{trypsin}]}, \tag{5-11}$$

where [trypsin] = 0.003 mg/mL is the concentration in the bulk degradation experiments and α ~ 1 cleavage site/kDa gelatin. Using γ ~ 0.002 cuts/(cleavage site·min) at time scales of the bead experiments, Equation (5-11) yields a rate constant k ~ 0.66 (min·mg/mL)$^{-1}$ at 20 ºC. We found in Section 5.5 that k = 0.47 (min·mg/mL)$^{-1}$. The agreement is good, considering the very different types of measurement.

5.7 Mechanism for bead motion

Next we sought to explain how enzymatic degradation led to gel swelling. We propose that enzymatic degradation shifted the equilibrium between osmotic swelling and gel self-attraction. The degree of swelling of a gel is characterized by the volume fraction, $\phi = \frac{V_p}{V_g}$, where V_p is the volume of the dry polymer, and V_g is the volume of the swollen gel. The theory of gel dynamics predicts that in a dilute gel, equilibrium is attained when

$$\phi_{eq} = \chi N_c^{-3/5}, \tag{5-12}$$

where χ is a material parameter and N_c is the mean number of monomeric segments between crosslinks of the polymer gel [128]. Enzymatic scission of crosslinks caused N_c to increase. Equation (5-12) implies that the degradation led to a smaller ϕ_{eq}, and hence to swelling of the gel. Equation (5-12) also predicts continuous expansion of the gel as a function of enzyme exposure, as we observed in Figure 5-5*a*. We hypothesize that the existence of a critical enzyme exposure prior to expansion was a consequence of the fibrillar nature of the crosslinks: many enzymatic cleavage events were needed before any crosslinks were cut (Figure 5-11).

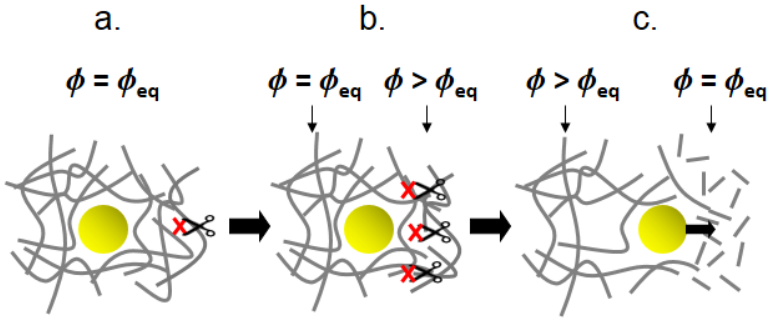

Figure 5-11: Mechanism for bead motion
(*a*) Gelatin starts in equilibrium. Enzyme, represented by scissors, diffuses in the local environment of a bead, but cleavage by enzyme does not change N_c at early times. (*b*) After a critical threshold of cleavage, N_c changes and shifts the equilibrium volume fraction. (*c*) As degradation proceeds, the gelatin swells, and pushes the bead forward into the liquefied gel solution.

Was the rate of gel swelling determined by the rate of the enzyme diffusion-reaction, or by hydrodynamic flow into the swelling gel? The approach to hydrostatic equilibrium in a dilute gel is described by Darcy's law

$$v_s - v_p = -\frac{1}{f}\nabla p, \tag{5-13}$$

where v_s is the velocity of the solvent, v_p is the velocity of the polymer, $f(\phi)$ is the frictional drag per unit gel volume between the polymer and solute, and $p(x, t)$ is the pressure in the gel. Applying incompressibility and mass conservation of the solvent and polymer, Darcy's law leads to a diffusion equation for the pressure:

$$\frac{\partial p(x,t)}{\partial t} = D_s \frac{\partial^2 p(x,t)}{\partial x^2}, \tag{5-14}$$

where D_s = is the ratio of osmotic modulus M to frictional drag f [128–130]. Previous measurements of D_s for gelatin by gel swelling studies via in-situ interferometry [131] and quasi-elastic light scattering studies [132, 133] show that $D_s \sim 20\text{-}40\ \mu m^2/s$, This estimate, which is on the same order as $D_{tryp} \sim 40\ \mu m^2/s$ (Section 5.4), implies that pressure diffused into the gel on the same time scale as trypsin.

However, we note that our estimate of D_s is only relevant for a solid, undegraded gel. In the gradient experiments, D_s decreased with time due to a degradation-induced decrease in the modulus M. At the end-point of the reaction, the gel was liquid and $M \rightarrow 0$, implying that $D_s \rightarrow 0$. We propose that due to the high degree of degradation at the onset of gel swelling, D_s was less than D_{tryp} throughout the time of bead motion. Thus the bead velocity was determined by hydrodynamic swelling, independent of bulk enzyme concentration, in agreement with our observations (*light grey bars*, Figure 5-7*c*).

5.8 Extension to other gel-enzyme systems

To test the generality of degradation-induced motion in gels, we studied the motion of beads in hyaluronan subject to asymmetric degradation by hyaluronidase. Hyaluronan is a large polymer of disaccharides, ranging from 5 kDa – 2×10^4 kDa [134]. As with collagen, hyaluronan is a major component of the ECM and serves as a lubricant and structural barrier [134]. This biogel interacts with cell surface receptors, and is thought to play an important role in the proliferation and migration of cancer cells [135, 136]. We prepared split channel flow cells as we had for gelatin: an aqueous gel of hyaluronan, doped with beads, was placed in one half of the channel, and a solution of hyaluronidase was flowed in the other half. As the enzyme degraded the gel, the beads moved toward the degradation front. Initial motion of the beads followed an invasion front, similar to the behavior in gelatin/trypsin (Figure 5-12).

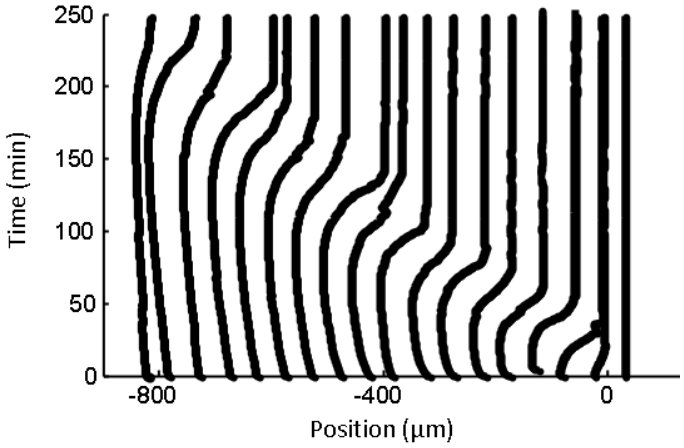

Figure 5-12: Degradation-induced motion of beads in a hyaluronan gel with hyaluronidase
Trajectories were acquired from time-lapse images of beads at 12 frames per minute. Similar motion to that of gelatin/trypsin was observed for this carbohydrate-based gel. Gen and enzyme concentrations were 1% w/w and 1 mg/mL, respectively.

The degraded hyaluronan had sufficiently low viscosity that the beads settled and stopped moving ~30 min after the initial motion. These observations establish that motion induced by asymmetric gel degradation occurs in both protein and carbohydrate-based biogels.

5.9 Conclusions and future directions

We have shown that asymmetric enzymatic degradation induces motion in a biogel via asymmetric swelling of the gel. Understanding the conditions under which this motion occurs can lead to new insights on how pathogenic bacteria invade host organisms, how cancer cells move through the extracellular matrix, and how biofilm-forming bacteria move and communicate with each other.

This mechanism of motion is distinct from the well-known diffusiophoretic effects in which concentration gradients in the liquid state lead to osmotic forces directly on a particle [137–140]. Experimental demonstrations of diffusiophoretic "swimmers" have been restricted to simple liquids [141]. The particle velocities we observe are orders of magnitude larger than would be predicted from diffusiophoresis alone and arise through large-scale reconfigurations of a viscoelastic gel.

Chemically powered phoretic motion in complex fluids offers qualitatively new modes of transport, and is likely to be relevant to biological motility. For instance, the bacterium *Listeria monocytogenes* propels itself within a host eukaryotic cell by an actin-based Brownian ratchet: asymmetric polymerization of the host actin by the bacterium produces a comet tail of stiff actin filaments leading to directed propulsion [142, 143]. We speculate that microorganisms may use asymmetric degradation of host biogels to induce directed propulsion as well. By investigating

possible mechanisms for selective passage of particles through viscoelastic barriers, one may be able to engineer systems to infiltrate these protective systems for targeted drug delivery.

5.10 Materials and methods

Gel-enzyme flow cell experiments

Trypsin from porcine pancreas (Sigma Aldrich T7409) was fluorescently labeled by reaction with Alexa 647 SE (Invitrogen A-20106) in a 1:1 molar ratio in 0.1 M pH 8.3 sodium bicarbonate, following manufacturer instructions. Excess dye was removed by spin centrifugation (GE PD SpinTrap G-25 28-9180-04).

Gelatin from bovine skin (Sigma-Aldrich G9391) was fluorescently labeled by reaction with Alexa 488 TFP (Invitrogen A-30005) in a 1 dye:1 lysine ratio in 0.1 M pH 9.0 sodium bicarbonate, following manufacturer instructions. Excess dye was removed by gravity flow column fractionation (GE PD-10 17-0851-01).

All experiments were performed in phosphate-buffer saline, pH 7.4 (PBS). Carboxylated polystyrene beads (6 μm diameter; Phosphorex 117) were washed by centrifugation (3 x 5 minutes at 15,000 g) to remove residual surfactant, and then re-suspended in PBS. Lyophilized gelatin washydrated in the washed bead suspension at 2.5%, 5%, or 10% (w/v) and heated at 60 ^{o}C until all pellets of gelatin were visibly dissolved. Gelatin-488 was doped into the unmodified bead-gelatin mixture in a 1:60 ratio.

To eliminate possible osmotic imbalances due to gelatin degradation products, the enzyme was pre-mixed with gelatin before the experiment. Trypsin-647 was doped into unmodified trypsin solution in a 1:90 ratio. The trypsin solution was mixed with unlabeled gelatin for a final trypsin concentration of 0.5, 1, 2, or 4 mg/mL and final gelatin concentration to match that of the

bead-gelatin mixture. The trypsin-gelatin solution was incubated at 4 ºC for 3 hours, ensuring complete degradation of the gelatin. The mixture remained liquid, as the trypsin digested the gelatin and prevented gelation.

For the gradient studies (Section 5.2), microfluidic channels were made with glass slides as the bottom and top surfaces, and sealed with melted parafilm (Figure 5-2 *a*). Half the width of the channel was temporarily filled with plastic shim of thickness 150 µm. The pre-heated microfluidic channels were filled with the molten bead-laden gel, and the gelatin was allowed to solidify at 4 ºC for 3 hours at 100% relative humidity. The sample was brought up to room temperature and mounted on the microscope. The plastic spacer was removed, and the empty half of the chamber was filled with the solution of trypsin and degraded gelatin to start the degradation.

For experiments on bead motion in uniformly degrading gelatin (Section 5.3), a microfluidic system was used to deliver enzyme homogeneously throughout the gel. Gel was cast in a flow cell similar to that used in Section 5.2. The top surface was removed, and replaced with a glass slide patterned with microchannels for trypsin delivery.

The microchannels were made by photolithography using SU-8 3025 (MicroChem). Channels were 1 cm (L) x 135 µm (W) x 25 µm (D), spaced by 165 µm, and covered a 1 cm x 1 cm window. The rest of the glass was coated in a 25 µm layer of SU-8. The slide was baked for 2 hours at 150 °C to promote adhesion of the SU-8. The slide was then plasma cleaned for 5 minutes to render the SU-8 hydrophilic. The dimensions of the channels were chosen based on D_{tryp} = 44.0 µm^2/s in 5% gelatin (Section 5.4) to allow trypsin to diffuse homogeneously throughout the sample within ~2 minutes.

As the enzyme digested the gel at room temperature (20 °C), time-lapse images were acquired on one of two setups: (1) a custom-built inverted microscope with 4x magnification

equipped with a QSI 504 camera and wide-field illumination by light emitting diodes (Luxeon V Star LXHL-LB5C) with corresponding filter cube (Olympus U-MWB2); or (2) an inverted Nikon TE-2000e microscope with 4x magnification equipped with a Hamamatsu 1394 ORCA-ERA camera and wide-field illumination by an X-Cite mercury lamp. Enzyme and gel motion were followed by fluorescence, and bead motion by white light trans-illumination.

Preparation of sample chambers with hyaluronan (Sigma-Aldrich 53747) and hyaluronidase (Sigma-Aldrich H3884) followed the same procedure as for the gelatin/trypsin experiments.

5.10.1 Bulk kinetics and SDS-PAGE studies

Solubilized trypsin and molten gelatin were prepared as described in Section 0, but without beads and fluorescent doping. Gelatin-trypsin samples were incubated at 20 ^{o}C on a tube rotator for the prescribed time and then boiled at 100 ^{o}C in 0.1 M Tris, 0.1 M HEPES, 3 mM SDS, 75 mM DTT, pH 8 for 5 minutes. Reaction products were fractionated via SDS-PAGE (Thermo Scientific Precise Protein Gels, 4-20%, 25244) at 135 V for 50 minutes. The gels were visualized with Coomassie Blue R-250 by staining overnight in a solution of 1% Coomassie R-250, 10% acetic acid, and 40% methanol, followed by destaining in 10% acetic acid, 40% methanol for 4-6 hours. The SDS-PAGE gel was evenly trans-illuminated with a light emitting capacitor (CeeLite) for digital photography. Images were processed in Matlab with custom scripts.

5.10.2 Data analysis

Movies of bead motion were analyzed as follows. Each image was bandpass filtered with a lower bound of 2 pixels and an upper bound of 10 pixels to remove point defects and to correct

for uneven illumination. Features were identified in each movie frame by brightness: only pixels less than three standard deviations of the mean pixel intensity were retained. Remaining features were then further culled by area: only features within two standard deviations of the mean area were kept. The Matlab adaptation [144] of the IDL Particle Tracking Code [145] was used find the centroids of the features, with a peak width of 9 pixels, and then to stitch the lists of centroids together into trajectories. The particles were expected to move at most 9 pixels between tracked frames and were allowed to disappear for at most four frames. Only trajectories that started in the first frame and lasted for more than 25% of the movie were kept. Trajectories of stuck particles were removed by hand.

Fluorescent images of gel-488 and trypsin-647 were corrected for dark counts and uneven illumination by a flat-field reference. Images were median-filtered to remove specks of dirt, and then averaged over the *y*-dimension to obtain intensity profiles as a function of (x, t).

SDS-PAGE images were analyzed using the reference ladder to map the spatial distribution of Coomassie blue stain of each lane to a number density profile as a function of molecular weight. The lane profiles were background-corrected by subtracting off the intensity profile of the enzyme-only control lane.

References

[1] ICH (2005) The nonclinical evaluation of the potential for delayed ventricular repolarization (QT interval prolongation) by human pharmaceuticals S7B. *Recommended for adoption at Step* (FDA & EMEA, 4.

[2] Ma J, Guo L, Fiene SJ, *et al*. (2011). High purity human-induced pluripotent stem cell-derived cardiomyocytes: electrophysiological properties of action potentials and ionic currents. *American Journal of Physiology-Heart and Circulatory Physiology* **301:**H2006-H2017.

[3] Hardy M, Lawrence C, Standen N, and Rodrigo G. (2006). Can optical recordings of membrane potential be used to screen for drug-induced action potential prolongation in single cardiac myocytes?. *Journal of Pharmacological and Toxicological Methods* **54:**173-182.

[4] Yazawa M, Hsueh B, Jia X, *et al*. (2011). Using induced pluripotent stem cells to investigate cardiac phenotypes in Timothy syndrome. *Nature* **471:**230-234.

[5] Itzhaki I, Maizels L, Huber I, *et al*. (2011). Modelling the long QT syndrome with induced pluripotent stem cells. *Nature* **471:**225-229.

[6] Segers VFM and Lee RT. (2008). Stem-cell therapy for cardiac disease. *Nature* **451:**937-942.

[7] Panáková D, Werdich AA, and MacRae CA. (2010). Wnt11 patterns a myocardial electrical gradient through regulation of the L-type Ca2+ channel. *Nature* **466:**874-878.

[8] Kaestner L and Lipp P. (2011). Screening action potentials: the power of light. *Frontiers in Pharmacology* **2:**42.

[9] Mandel Y, Weissman A, Schick R, *et al*. (2012). Human embryonic and induced pluripotent stem cell–derived cardiomyocytes exhibit beat rate variability and power-law behavior. *Circulation* **125:**883-893.

[10] Entcheva E and Bien H. (2006). Macroscopic optical mapping of excitation in cardiac cell networks with ultra-high spatiotemporal resolution. *Progress in Biophysics and Molecular Biology* **92:**232-257.

[11] Salama G and Morad M. (1976). Merocyanine 540 as an optical probe of transmembrane electrical activity in the heart. *Science (New York, NY)* **191:**485-487.

[12] Rohr S and Salzberg B. (1992). Discontinuities in action potential propagation along chains of single ventricular myocytes in culture: multiple site optical recording of transmembrane voltage (MSORTV) suggests propagation delays at the junctional sites between cells. *The Biological Bulletin* **183:**342-343.

[13] Fast VG and Kléber AG. (1993). Microscopic conduction in cultured strands of neonatal rat heart cells measured with voltage-sensitive dyes. *Circulation Research* **73:**914-925.

[14] Windisch H, Ahammer H, Schaffer P, Müller W, and Platzer D. (1995). Optical multisite monitoring of cell excitation phenomena in isolated cardiomyocytes. *Pflügers Archiv European Journal of Physiology* **430:**508-518.

[15] Ren Y, Lee MY, Schliffke S, *et al*. (2011). Small molecule Wnt inhibitors enhance the efficiency of BMP-4-directed cardiac differentiation of human pluripotent stem cells. *Journal of Molecular and Cellular Cardiology* **51:**280-287.

[16] Choi BR and Salama G. (2000). Simultaneous maps of optical action potentials and calcium transients in guinea-pig hearts: mechanisms underlying concordant alternans. *The Journal of Physiology* **529:**171-188.

[17] Lee P, Klos M, Bollensdorff C, *et al*. (2012). Simultaneous Voltage and Calcium Mapping of Genetically Purified Human Induced Pluripotent Stem Cell-Derived Cardiac Myocyte Monolayers. *Circ Res* **110:**1556-1563.

[18] Herron TJ, Lee P, and Jalife J. (2012). Optical imaging of voltage and calcium in cardiac cells & tissues. *Circulation Research* **110:**609-623.

[19] Akerboom J, Chen TW, Wardill TJ, *et al*. (2012). Optimization of a GCaMP calcium indicator for neural activity imaging. *J Neurosci* **32:**13819-13840.

[20] Kralj JM, Douglass AD, Hochbaum DR, Maclaurin D, and Cohen AE. (2012). Optical recording of action potentials in mammalian neurons using a microbial rhodopsin. *Nature Methods* **9:**90-95.

[21] Bayraktar H, Fields AP, Kralj JM, *et al*. (2011). Ultrasensitive measurements of microbial rhodopsin photocycles using photochromic FRET. *Photochemistry and Photobiology* **88:**90-97.

[22] Miller EW, Lin JY, Frady EP, *et al*. (2012). Optically monitoring voltage in neurons by photo-induced electron transfer through molecular wires. *Proceedings of the National Academy of Sciences* **109:**2114-2119.

[23] Sjulson L and Miesenbock G. (2007). Optical recording of action potentials and other discrete physiological events: a perspective from signal detection theory. *Physiology* **22:**47.

[24] Maclaurin DM, Venkatachalam VV, Lee H, and Cohen AE. (2013). Mechanism of voltage-sensitive fluorescence in a microbial rhodopsin. *Proc Natl Acad Sci USA* **110:**5939-5944.

[25] Cheng H, Lederer M, Lederer W, and Cannell M. (1996). Calcium sparks and Ca^{2+} waves in cardiac myocytes. *American Journal of Physiology-Cell Physiology* **270:**C148-C159.

[26] Gibson DG, Young L, Chuang RY, *et al*. (2009). Enzymatic assembly of DNA molecules up to several hundred kilobases. *Nature Methods* **6:**343-345.

[27] WOODBURY JW, LEE J, BRADY AJ, and MERENDINO KA. (1957). Transmembranal potentials from the human heart. *Circulation Research* **5:**179-179.

[28] Stainier DY. (2001). Zebrafish genetics and vertebrate heart formation. *Nature Reviews Genetics* **2:**39-48.

[29] Glickman NS, Yelon D (2002) Cardiac development in zebrafish: coordination of form and function

[30] Pelster B and Burggren WW. (1996). Disruption of hemoglobin oxygen transport does not impact oxygen-dependent physiological processes in developing embryos of zebra fish (Danio rerio). *Circulation Research* **79:**358-362.

[31] Stainier D, Fouquet B, Chen J, *et al*. (1996). Mutations affecting the formation and function of the cardiovascular system in the zebrafish embryo. *Development* **123:**285-292.

[32] Warren KS, Wu JC, Pinet F, and Fishman MC. (2000). The genetic basis of cardiac function: dissection by zebrafish (Danio rerio) screens. *Philosophical Transactions of the Royal Society of London.Series B: Biological Sciences* **355:**939-944.

[33] Chen J, Haffter P, Odenthal J, *et al*. (1996). Mutations affecting the cardiovascular system and other internal organs in zebrafish. *Development* **123:**293-302.

[34] Karlsson J, von Hofsten J, and Olsson P. (2001). Generating transparent zebrafish: a refined method to improve detection of gene expression during embryonic development. *Marine Biotechnology* **3:**522-527.

[35] Nemtsas P, Wettwer E, Christ T, Weidinger G, and Ravens U. (2010). Adult zebrafish heart as a model for human heart? An electrophysiological study. *Journal of Molecular and Cellular Cardiology* **48:**161-171.

[36] Milan DJ, Jones IL, Ellinor PT, and MacRae CA. (2006). In vivo recording of adult zebrafish electrocardiogram and assessment of drug-induced QT prolongation. *American Journal of Physiology-Heart and Circulatory Physiology* **291:**H269-H273.

[37] Sedmera D, Reckova M, Rosengarten C, *et al*. (2005). Optical mapping of electrical activation in the developing heart. *Microscopy and Microanalysis* **11:**209-215.

[38] Tsutsui H, Higashijima S, Miyawaki A, and Okamura Y. (2010). Visualizing voltage dynamics in zebrafish heart. *The Journal of Physiology* **588:**2017-2021.

[39] Tsutsui H, Karasawa S, Okamura Y, and Miyawaki A. (2008). Improving membrane voltage measurements using FRET with new fluorescent proteins. *Nature Methods* **5:**683-685.

[40] Sehnert AJ, Huq A, Weinstein BM, *et al*. (2002). Cardiac troponin T is essential in sarcomere assembly and cardiac contractility. *Nature Genetics* **31:**106-110.

[41] Milan DJ, Giokas AC, Serluca FC, Peterson RT, and MacRae CA. (2006). Notch1b and neuregulin are required for specification of central cardiac conduction tissue. *Development* **133:**1125-1132.

[42] Chi NC, Shaw RM, Jungblut B, *et al*. (2008). Genetic and physiologic dissection of the vertebrate cardiac conduction system. *PLoS Biology* **6:**e109.

[43] Ono K and Iijima T. (2010). Cardiac T-type Ca< sup> 2 channels in the heart. *Journal of Molecular and Cellular Cardiology* **48:**65-70.

[44] Langheinrich U, Vacun G, and Wagner T. (2003). Zebrafish embryos express an orthologue of HERG and are sensitive toward a range of QT-prolonging drugs inducing severe arrhythmia☆. *Toxicology and Applied Pharmacology* **193:**370-382.

[45] Tu S and Chi NC. (2012). Zebrafish models in cardiac development and congenital heart birth defects. *Differentiation* **84:**4-16.

[46] Hochbaum DR, Klapoetke N, Maclaurin D, *et al*. (2013). Optopatch: All-optical electrophysiology in mammalian neurons. *Submitted*

[47] Chen T, Wardill TJ, Sun Y, *et al*. (2013). Ultrasensitive fluorescent proteins for imaging neuronal activity. *Nature* **499:**295-300.

[48] Weber M and Huisken J. (2011). Light sheet microscopy for real-time developmental biology. *Current Opinion in Genetics & Development* **21:**566-566–572.

[49] Müller O, Tian Q, Zantl R, *et al*. (2010). A system for optical high resolution screening of electrical excitable cells. *Cell Calcium* **47:**224-233.

[50] Werdich AA, Brzezinski A, Jeyaraj D, *et al*. (2012). The zebrafish as a novel animal model to study the molecular mechanisms of mechano-electrical feedback in the heart. *Progress in Biophysics and Molecular Biology* **110:**154-165.

[51] Poss KD, Wilson LG, and Keating MT. (2002). Heart regeneration in zebrafish. *Science* **298:**2188-2190.

[52] Raya Á, Consiglio A, Kawakami Y, Rodriguez-Esteban C, and Izpisúa-Belmonte JC. (2004). The zebrafish as a model of heart regeneration. *Cloning and Stem Cells* **6:**345-351.

[53] Zhang R, Han P, Yang H, *et al*. (2013). In vivo cardiac reprogramming contributes to zebrafish heart regeneration. *Nature*

[54] Lien C, Wu C, Mercer B, *et al*. (1999). Control of early cardiac-specific transcription of Nkx2-5 by a GATA-dependent enhancer. *Development* **126:**75-84.

[55] Yoshinari N, Ando K, Kudo A, Kinoshita M, and Kawakami A. (2012). Colored medaka and zebrafish: Transgenics with ubiquitous and strong transgene expression driven by the medaka β-actin promoter. *Development, Growth & Differentiation* **54:**818-828.

[56] Fang Q and Boas DA. (2009). Tetrahedral mesh generation from volumetric binary and grayscale images. *IEEE Int Symp Biomed Imaging* 1142-1145.

[57] Bezanilla F. (2008). How membrane proteins sense voltage. *Nature Reviews Molecular Cell Biology* **9:**323-332.

[58] Murata Y, Iwasaki H, Sasaki M, Inaba K, and Okamura Y. (2005). Phosphoinositide phosphatase activity coupled to an intrinsic voltage sensor. *Nature* **435:**1239-1243.

[59] Mahaut-Smith MP, Martinez-Pinna J, and Gurung IS. (2008). A role for membrane potential in regulating GPCRs?. *Trends in Pharmacological Sciences* **29:**421-429.

[60] Principe DD, Avigliano L, Savini I, and Catani MV. (2011). Trans-plasma membrane electron transport in mammals: functional significance in health and disease. *Antioxidants & Redox Signaling* **14:**2289-2318.

[61] Blatt MR, Rodriguez-Navarro A, and Slayman CL. (1987). Potassium-proton symport in Neurospora: Kinetic control by pH and membrane potential. *The Journal of Membrane Biology* **98:**169-189.

[62] Kamo N, Muratsugu M, Hongoh R, and Kobatake Y. (1979). Membrane potential of mitochondria measured with an electrode sensitive to tetraphenyl phosphonium and relationship between proton electrochemical potential and phosphorylation potential in steady state. *The Journal of Membrane Biology* **49:**105-121.

[63] Felle H, Porter JS, Slayman CL, and Kaback HR. (1980). Quantitative measurements of membrane potential in Escherichia coli. *Biochemistry* **19:**3585-3590.

[64] Cone Jr CD. (1971). Unified theory on the basic mechanism of normal mitotic control and oncogenesis. *Journal of Theoretical Biology* **30:**151-181.

[65] Binggeli R and Weinstein RC. (1986). Membrane potentials and sodium channels: hypotheses for growth regulation and cancer formation based on changes in sodium channels and gap junctions. *Journal of Theoretical Biology* **123:**377-401.

[66] Biagiotti T, D'Amico M, Marzi I, *et al*. (2006). Cell renewing in neuroblastoma: electrophysiological and immunocytochemical characterization of stem cells and derivatives. *Stem Cells* **24:**443-453.

[67] Jin L, Han Z, Platisa J, *et al*. (2012). Single action potentials and subthreshold electrical events imaged in neurons with a fluorescent protein voltage probe. *Neuron* **75:**779-785.

[68] Lam AJ, St-Pierre F, Gong Y, *et al*. (2012). Improving FRET dynamic range with bright green and red fluorescent proteins. *Nature Methods* **9:**1005-1012.

[69] Cao G, Platisa J, Pieribone VA, *et al*. (2013). Genetically Targeted Optical Electrophysiology in Intact Neural Circuits. *Cell* **154:**904-913.

[70] Akemann W, Mutoh H, Perron A, Rossier J, and Knöpfel T. (2010). Imaging brain electric signals with genetically targeted voltage-sensitive fluorescent proteins. *Nature Methods* **7:**643-649.

[71] Aw S, Koster J, Pearson W, *et al*. (2010). The ATP-sensitive K -channel (KATP) controls early left-right patterning in Xenopus and chick embryos. *Developmental Biology* **346:**39-39-53.

[72] Sundelacruz S, Levin M, and Kaplan DL. (2009). Role of membrane potential in the regulation of cell proliferation and differentiation. *Stem Cell Reviews and Reports* **5:**231-246.

[73] Beane WS, Morokuma J, Adams DS, and Levin M. (2011). A Chemical Genetics Approach Reveals H, K-ATPase-Mediated Membrane Voltage Is Required for Planarian Head Regeneration. *Chemistry & Biology* **18:**77-89.

[74] Nicholls DG and Ward MW. (2000). Mitochondrial membrane potential and neuronal glutamate excitotoxicity: mortality and millivolts. *Trends in Neurosciences* **23:**166-174.

[75] Mousavi SA, Chauvin A, Pascaud F, Kellenberger S, and Farmer EE. (2013). GLUTAMATE RECEPTOR-LIKE genes mediate leaf-to-leaf wound signalling. *Nature* **500:**422-426.

[76] Volkov AG .(2006) *Plant electrophysiology*, (Springer, Berlin),

[77] Miesenbock G, De Angelis DA, and Rothman JE. (1998). Visualizing secretion and synaptic transmission with pH-sensitive green fluorescent proteins. *Nature* **394:**192-195.

[78] Grynkiewicz G, Poenie M, and Tsien RY. (1985). A new generation of Ca2+ indicators with greatly improved fluorescence properties. *Journal of Biological Chemistry* **260:**3440-3450.

[79] Miyawaki A, Llopis J, Heim R, *et al*. (1997). Fluorescent indicators for Ca2+; based on green fluorescent proteins and calmodulin. *Nature* **388:**882-887.

[80] Ting AY, Kain KH, Klemke RL, and Tsien RY. (2001). Genetically encoded fluorescent reporters of protein tyrosine kinase activities in living cells. *Proceedings of the National Academy of Sciences* **98:**15003-15008.

[81] Zhang J, Ma Y, Taylor SS, and Tsien RY. (2001). Genetically encoded reporters of protein kinase A activity reveal impact of substrate tethering. *Proceedings of the National Academy of Sciences* **98:**14997-15002.

[82] Gross E, Bedlack Jr RS, and Loew LM. (1994). Dual-wavelength ratiometric fluorescence measurement of the membrane dipole potential. *Biophysical Journal* **67:**208-216.

[83] Zhang J, Davidson RM, Wei M, and Loew LM. (1998). Membrane electric properties by combined patch clamp and fluorescence ratio imaging in single neurons. *Biophysical Journal* **74:**48-53.

[84] Sakai R, Repunte-Canonigo V, Raj CD, and Knopfel T. (2001). Design and characterization of a DNA-encoded, voltage-sensitive fluorescent protein. *European Journal of Neuroscience* **13:**2314-2318.

[85] Lundby A, Mutoh H, Dimitrov D, Akemann W, and Knöpfel T. (2008). Engineering of a genetically encodable fluorescent voltage sensor exploiting fast Ci-VSP voltage-sensing movements. *PLoS One* **3:**2514.

[86] Murakoshi H, Lee S, and Yasuda R. (2008). Highly sensitive and quantitative FRET–FLIM imaging in single dendritic spines using improved non-radiative YFP. *Brain Cell Biology* **36:**31-42.

[87] Murakoshi H and Yasuda R. (2012). Postsynaptic signaling during plasticity of dendritic spines. *Trends in Neurosciences* **35:**135-143.

[88] Wang W, Nossoni Z, Berbasova T, *et al*. (2012). Tuning the Electronic Absorption of Protein-Embedded All-trans-Retinal. *Science* **338:**1340-1343.

[89] Kralj JM, Hochbaum DR, Douglass AD, and Cohen AE. (2011). Electrical spiking in Escherichia coli probed with a fluorescent voltage indicating protein. *Science* **333:**345-348.

[90] Ohtani H, Kaneko M, Ishikawa M, Kamiya N, and Yamamoto N. (1999). Picosecond-millisecond dual-time-base spectroscopy of fluorescent photointermediates formed in the purple membrane of Halobacterium halobium. *Chemical Physics Letters* **299:**571-575.

[91] Hagedorn R, Gradmann D, and Hegemann P. (2008). Dynamics of voltage profile in enzymatic ion transporters, demonstrated in electrokinetics of proton pumping rhodopsin. *Biophysical Journal* **95:**5005-5013.

[92] Geibel S, Lörinczi È, Bamberg E, and Friedrich T. (2013). Voltage Dependence of Proton Pumping by Bacteriorhodopsin Mutants with Altered Lifetime of the M Intermediate. *PloS One* **8:**e73338.

[93] Park J, Werley CA, Venkatachalam V, *et al*. (2013). Screening fluorescent voltage indicators in spontaneously spiking HEK cells. *PLoS One. (In press)***.**

[94] Chow BY, Han X, Dobry AS, *et al*. (2010). High-performance genetically targetable optical neural silencing by light-driven proton pumps. *Nature* **463:**98-102.

[95] Tsukamoto H and Terakita A. (2010). Diversity and functional properties of bistable pigments. *Photochemical & Photobiological Sciences* **9:**1435-1443.

[96] Clarke RJ. (2001). The dipole potential of phospholipid membranes and methods for its detection. *Advances in Colloid and Interface Science* **89:**263-281.

[97] Xu C and Loew LM. (2003). The effect of asymmetric surface potentials on the intramembrane electric field measured with voltage-sensitive dyes. *Biophysical Journal* **84:**2768-2780.

[98] Bedlack RS, Wei M, Fox SH, Gross E, and Loew LM. (1994). Distinct electric potentials in soma and neurite membranes. *Neuron* **13:**1187-1193.

[99] Spudich JL. (2006). The multitalented microbial sensory rhodopsins. *Trends in Microbiology* **14:**480-487.

[100] Assion A, Baumert T, Bergt M, *et al*. (1998). Control of chemical reactions by feedback-optimized phase-shaped femtosecond laser pulses. *Science* **282:**919-922.

[101] Inoue S and Inoue T. (2002). Direct-view high-speed confocal scanner: the CSU-10. *Methods in Cell Biology* **70:**87-127.

[102] Thornton DJ and Sheehan JK. (2004). From mucins to mucus: toward a more coherent understanding of this essential barrier. *Proc Am Thoracic Soc* **1:**54.

[103] Hay ED .(1991) *Cell biology of extracellular matrix* (Springer,

[104] Flemming HC and Wingender J. (2010). The biofilm matrix. *Nature Reviews Microbiology* **8:**623-633.

[105] Linden S, Sutton P, Karlsson N, Korolik V, and McGuckin M. (2008). Mucins in the mucosal barrier to infection. *Mucosal Immunology* **1:**183-197.

[106] Cone RA. (2009). Barrier properties of mucus. *Advanced Drug Delivery Reviews* **61:**75-85.

[107] Bosman FT and Stamenkovic I. (2003). Functional structure and composition of the extracellular matrix. *The Journal of Pathology* **200:**423-428.

[108] Fomovsky GM, Thomopoulos S, and Holmes JW. (2010). Contribution of extracellular matrix to the mechanical properties of the heart. *Journal of Molecular and Cellular Cardiology* **48:**490-496.

[109] Rosso F, Giordano A, Barbarisi M, and Barbarisi A. (2004). From cell–ECM interactions to tissue engineering. *Journal of Cellular Physiology* **199:**174-180.

[110] Tsang KY, Cheung MCH, Chan D, and Cheah KSE. (2010). The developmental roles of the extracellular matrix: beyond structure to regulation. *Cell and Tissue Research* **339:**93-110.

[111] Martin P. (1997). Wound healing--aiming for perfect skin regeneration. *Science* **276:**75.

[112] Sabeh F, Shimizu-Hirota R, and Weiss SJ. (2009). Protease-dependent versus-independent cancer cell invasion programs: three-dimensional amoeboid movement revisited. *The Journal of Cell Biology* **185:**11.

[113] Stetler-Stevenson WG and Yu AE. (2001). Proteases in invasion: matrix metalloproteinases. *Seminars in Cancer Biol* **11:**143-153.

[114] Stoodley P, Dodds I, Boyle J, and Lappin-Scott H. (1998). Influence of hydrodynamics and nutrients on biofilm structure. *Journal of Applied Microbiology* **85:**19S-28S.

[115] Celli JP, Turner BS, Afdhal NH, *et al*. (2009). Helicobacter pylori moves through mucus by reducing mucin viscoelasticity. *Proceedings of the National Academy of Sciences* **106:**14321-14326.

[116] Kramer RA, . Zandwijken D, Egmond MR, and Dekker N. (2000). In vitro folding, purification and characterization of Escherichia coli outer membrane protease OmpT. *Eur J Biochem* **267:**885-893.

[117] Scott ME, Dossani ZY, and Sandkvist M. (2001). Directed polar secretion of protease from single cells of Vibrio cholerae via the type II secretion pathway. *Proceedings of the National Academy of Sciences* **98:**13978-13983.

[118] Silva AJ, Pham K, and Benitez JA. (2003). Haemagglutinin/protease expression and mucin gel penetration in El Tor biotype Vibrio cholerae. *Microbiology* **149:**1883-1891.

[119] Matrosovich MN, Matrosovich TY, Gray T, Roberts NA, and Klenk HD. (2004). Neuraminidase is important for the initiation of influenza virus infection in human airway epithelium. *Journal of Virology* **78:**12665.

[120] Kuiken T, Holmes EC, McCauley J, *et al*. (2006). Host species barriers to influenza virus infections. *Science* **312:**394.

[121] Lauffer MA. (1961). Theory of diffusion in gels. *Biophysical Journal* **1:**205-213.

[122] Keil B .(1992) *Specificity of proteolysis* (Springer-Verlag, Berlin; New York).

[123] Harrington WF and Von Hippel PH. (1961). The structure of collagen and gelatin. *Adv Protein Chem* **16:**1-138.

[124] Aris R and Gavalas G. (1966). On the theory of reactions in continuous mixtures. *Philosophical Transactions of the Royal Society of London.Series A, Mathematical and Physical Sciences* **260:**351.

[125] McCoy BJ and Wang M. (1994). Continuous-mixture fragmentation kinetics: Particle size reduction and molecular cracking. *Chemical Engineering Science* **49:**3773-3785.

[126] Robinson C and Bott M. (1951). Optical rotation and chain folding in synthetic polypeptides and gelatin. *Nature* **168:**325-326.

[127] Djabourov M, Leblond J, and Papon P. (1988). Gelation of aqueous gelatin solutions. I. Structural investigation. *Journal De Physique* **49:**319-332.

[128] Masao D. (2009). Gel Dynamics. *Journal of the Physical Society of Japan* **78:**052001.

[129] Tanaka T and Fillmore DJ. (1979). Kinetics of swelling of gels. *The Journal of Chemical Physics* **70:**1214.

[130] Li Y and Tanaka T. (1990). Kinetics of swelling and shrinking of gels. *The Journal of Chemical Physics* **92:**1365.

[131] Wu C and Yan CY. (1994). Studies of the swelling and drying kinetics of thin gelatin gel films by in situ interferometry. *Macromolecules* **27:**4516-4520.

[132] Amis EJ, Janmey PA, Ferry JD, and Yu H. (1983). Quasielastic light scattering of gelatin solutions and gels. *Macromolecules* **16:**441-446.

[133] Herning T, Djabourov M, Leblond J, and Takerkart G. (1991). Conformation of gelatin chains in aqueous solutions: 2. A quasi-elastic light scattering study. *Polymer* **32:**3211-3217.

[134] Laurent TC, Laurent UBG, and Fraser JRE. (1996). The structure and function of hyaluronan: An overview. *Immunology and Cell Biology* **74:**A1-A7.

[135] Sugahara KN, Murai T, Nishinakamura H, *et al*. (2003). Hyaluronan oligosaccharides induce CD44 cleavage and promote cell migration in CD44-expressing tumor cells. *Journal of Biological Chemistry* **278:**32259.

[136] Adamia S, Maxwell CA, and Pilarski LM. (2005). Hyaluronan and hyaluronan synthases: potential therapeutic targets in cancer. *Current Drug Targets-Cardiovascular & Hematological Disorders* **5:**3-14.

[137] Golestanian R, Liverpool TB, and Ajdari A. (2005). Propulsion of a molecular machine by asymmetric distribution of reaction products. *Physical Review Letters* **94:**220801.

[138] Howse JR, Jones RAL, Ryan AJ, *et al*. (2007). Self-motile colloidal particles: from directed propulsion to random walk. *Physical Review Letters* **99:**48102.

[139] Rückner G and Kapral R. (2007). Chemically powered nanodimers. *Physical Review Letters* **98:**150603.

[140] Anderson JL. (1989). Colloid transport by interfacial forces. *Annual Review of Fluid Mechanics* **21:**61-99.

[141] Paxton WF, Kistler KC, Olmeda CC, *et al*. (2004). Catalytic nanomotors: Autonomous movement of striped nanorods. *Journal of the American Chemical Society* **126:**13424-13431.

[142] Theriot JA, Mitchison TJ, Tilney LG, and Portnoy DA. (1992). The rate of actin-based motility of intracellular Listeria monocytogenes equals the rate of actin polymerization. *Nature* **357:**257-260.

[143] Smith GA, Portnoy DA, and Theriot JA. (1995). Asymmetric distribution of the Listeria monocytogenes ActA protein is required and sufficient to direct actin-based motility. *Molecular Microbiology* **17:**945-951.

[144] Blair D and Dufresne E .(2008). The Matlab Particle Tracking Code Repository. http://physics.georgetown.edu/matlab/index.html.

[145] Crocker JC and Grier DG. (1996). Methods of digital video microscopy for colloidal studies. *Journal of Colloid and Interface Science* **179:**298-310.